Fall 12-2014

Investigation of Glassy State Molecular Motions in Thermoset Polymers

Jianwei Tu
University of Southern Mississippi

The University of Southern Mississippi

INVESTIGATION OF GLASSY STATE MOLECULAR MOTIONS IN THERMOSET POLYMERS

by

Jianwei Tu

Abstract of a Dissertation
Submitted to the Graduate School
of The University of Southern Mississippi
in Partial Fulfillment of the Requirements
for the Degree of Doctor of Philosophy

December 2014

ABSTRACT

INVESTIGATION OF GLASSY STATE MOLECULAR MOTIONS

IN THERMOSET POLYMERS

by Jianwei Tu

December 2014

This dissertation presents the investigation of the glassy state molecular motions in isomeric thermoset epoxies by means of solid-state deuterium (^{2}H) NMR spectroscopy technique. The network structure of crosslinked epoxies was altered through monomer isomerism; specifically, diglycidyl ether of bisphenol A (DGEBA) was cured with isomeric amine curatives, *i.e.*, the meta-substituted diaminodiphenylsulfone (33DDS) and para-substituted diaminodiphenylsulfone (44DDS). The use of structural isomerism provided a path way for altering macroscopic material properties while maintaining identical chemical composition within the crosslinked networks.

The effects of structural isomerism on the glassy state molecular motions were studied using solid-state ^{2}H NMR spectroscopy, which offers unrivaled power to monitor site-specific molecular motions. Three distinctive molecular groups on each isomeric network, *i.e.,* the phenylene rings in the bisphenol A structure (BPA), the phenylene rings in the diaminodiphenylsulfone structure (DDS), and the hydroxypropoyl ether group (HPE) have been selectively deuterated for a comprehensive study of the structure-dynamics-property relationships in thermoset epoxies.

Quadrupolar echo experiments and line shape simulations were employed as the main research approach to gain both qualitative and quantitative motional information of

the epoxy networks in the glassy state. Quantitative information on the geometry and rate of the molecular motions allows the elucidation of the relationship between molecular motions and macro physical properties and the role of these motions in the mechanical relaxation. Specifically, it is revealed that both the BPA and HPE moieties in the isomeric networks have almost identical behaviors in the deep glassy state, which indicates that the molecular motions in the glassy state are localized, and the correlation length of the motions does not exceed the length of the DGEBA repeat unit. BPA ring motions contribute to the low temperature (around -80 to -50 °C) region, and HPE chain motions to the even lower temperature range (-110 °C) of the mechanical relaxation as detected by DMA. The differences in the physical properties of the isomeric epoxies are mostly attributed to the DDS moieties. The occurrence of 44DDS ring motions decreases the modulus and the swept-out space from its ring axis fluctuation explains the higher hole-size free volume of the para-substituted networks. 33DDS rings do not exhibit large amplitude motions but only undergo fast small-angle fluctuations, which results in a decrease in the magnitude of the high temperature part of the γ relaxation of 33A, a phenomenon often seen in the anti-plasticization process.

The University of Southern Mississippi

INVESTIGATION OF GLASSY STATE MOLECULAR MOTIONS IN THERMOSET POLYMERS

by

Jianwei Tu

A Dissertation
Submitted to the Graduate School
of The University of Southern Mississippi
in Partial Fulfillment of the Requirements
for the Degree of Doctor of Philosophy

Approved:

Dr. Jeffrey Wiggins
Committee Chair

Dr. William Jarrett

Dr. Sergei Nazarenko

Dr. James Rawlins

Dr. Robson Storey

Dr. Karen S. Coats
Dean of the Graduate School

December 2014

DEDICATION

To my hometown, the City of Rui'an.

To Mother, Father, and my sister Xiuwei.

To the love of my life Tongtong and my sweetheart Yolanda.

ACKNOWLEDGMENTS

Graduate school is not only an intellectual challenge, but also a test of endurance. Without the support and encouragement from the following people I would have not gone this far at Southern Miss.

First and foremost I would like to thank my advisor Dr. Jeffrey Wiggins. He has been a great mentor and a best friend, and provided me with intellectual guidance and financial support to achieve my career goal. I would also like to acknowledge my research committee members, Dr. William Jarrett, Dr. Sergei Nazarenko, Dr. James Rawlins, and Dr. Robson Storey, for challenging me to be a real scientist. I especially would like to thank Dr. William Jarrett for being a great source of NMR and for the countless times of discussion.

I have had the good fortune to work with many smart and diligent people in the Wiggins Research Group. I am greatly indebted to Dr. Samuel Tucker and Dr. Stephen Heinz for their inspiration and pioneering works. They have taught me to be the scientist I am. I also owe sincere gratitude to Dr. Abdelwahed Sayed, for without his amazing synthetic skills all this research would be impossible. I really want to thank Dr. Matthew Jackson for all the help he has provided me with. I also appreciate the friendship with Dr. Katherine Frank; I enjoyed the tasty cookies she made. I want to thank all other Wiggins Group members for their friendship, and Ms. Charlie and Stephenie for all their kindness.

I would like to thank the Chinese community at Southern Miss for their friendship and trust. I am honored to become a friend of Dr. Jinhai Yang, who has always been

leading me to God. I thank Mr. Yan Zong for being a delightful roommate. To others, I cherish the good times we have spent together.

Finally I want to thank all the friends I have made throughout my visit at Southern Miss, including all the faculty, staff, and graduate students in Polymer Science, and friends outside of the department as well, especially Bharath Kumar. You all have made life so much easier and joyful.

TABLE OF CONTENTS

LIST OF TABLES

Table

LIST OF ILLUSTRATIONS

Figure

LIST OF EQUATIONS

Equation

CHAPTER I

INTRODUCTION

Research Incentives

Materials make up every aspect of our world and have been critical throughout history in advancing both technological and cultural development, from the tools of the Bronze Age to the silicon driving the Information Age. An epic challenge of the 21st century is meeting the growing demand worldwide for efficient and sustainable energy consumption. Light-weight, high-strength and high-stiffness composite materials have been identified as a key cross-cutting technology for reinventing energy efficient transportation, enabling efficient power generation, and providing new mechanisms for storing and transporting reduced carbon fuels.[1] Advanced carbon-fiber-reinforced polymer composites are particularly promising materials for application in transportation industries and energy savings for their higher structural strength-to-weight ratio over many structural materials.

Fiber-reinforced polymer (FRP) composites exhibit exceptional structural properties thanks to the excellently engineered combination of a matrix, usually a homogeneous and isotropic polymer resin which protects against abrasion or chemical attack, and anisotropic reinforcing fibers, which mechanically support and transfer loads. The proliferation of applications of FRP composites in aerospace and defense, and more recently in luxury automobiles, wind turbines, and compressed gas storage tanks, has led to vibrant efforts to optimize the properties of polymer matrices and carbon fibers, and research interests aimed to understand the interfacial properties between the constituents.

Thermoset epoxy networks have been widely used as polymer matrices due to their excellent mechanical properties, thermal capacity, solvent resistance, manufacturability, and low cost. To achieve "aerospace quality", crosslinked epoxy networks usually comprise of highly aromatic, low molecular-weight monomers, and thus are inherently brittle. Adding toughening agents such as thermoplastic polymers to epoxies to some extent alleviates the problem, but this is usually achieved at the sacrifice of the high modulus, high glass transition temperature (T_g), and processability.[2,3] Therefore, a major research target of the Wiggins Research Group at the University of Southern Mississippi has been to research for ideal epoxies that have high modulus, high strength and high T_g for use as next generation matrix materials. The philosophy of research is that a better understanding of the structure-dynamics-property relationships of epoxy networks will allow the intelligent design of monomer molecules to build better matrix materials.

Advances in synthetic techniques and in polymer functionality both require and inspire advances in our ability to characterize molecular and material structure in detail. The molecular structure and dynamics, and their characteristics during synthesis, processing, and characterization, all of which determine the material properties in the final state, also must be understood to enable rational advances in polymer design and optimization of performance.[4] A multi-scale and multi-technique research approach is therefore employed by the Wiggins Research Group to achieve such a goal, which starts from a molecular level design and screening of polymers though Computational Molecular Dynamics Modeling to laboratory syntheses of targeted molecules, and from quantum-mechanics level characterization of molecular dynamics using solid-state NMR

spectroscopy to macro-scale determination of complex deformation behaviors through high-accuracy Digital Image Correlation techniques.

Glass Transition

In the study of polymers and their applications, it is important to understand the concept of T_g, the glass transition temperature. T_g is one of the most important properties of amorphous polymers. When the temperature rises above the T_g of an amorphous polymer the material becomes soft and pliable. If the polymer is crosslinked or semi-crystalline, above its T_g or the T_g of its amorphous phase the material becomes rubbery. When the temperature drops below the T_g, the material will become hard and glassy. In general, values of T_g well below room temperature define the domain of soft materials and elastomers, whereas values above room temperature define rigid, structural polymers. Thus, knowledge of T_g is essential in the selection of materials for various applications. For example, elastomers find their applications in automotive tires in transportation industries, sonar attenuation for acoustic tiles on submarines, and arterial walls for medical use, whereas advanced glassy polymers are commonly used in electronics for memory storage and device fabrication, in organic photovoltaic for batteries, in fibers and matrix chemistries for light-weight high performance composites, as well as in energy storage, generation, and power conversion where polymeric glasses are structural entities.

Because of the significance of T_g, one might be interested in asking: What happens at the glass transition? This question has indeed been asked by generations of scientists and has drawn great interest and intensive efforts. However, believe it or not, the exact nature of glass transition remains elusive to date. When one takes a fresh look at the literature on the glass transition, they cannot fail to be struck by the wide diversity

of views and approaches. The well-known quip that "There are more theories of the glass transitions than there are theorists who propose them" is reflective of the diversity and enormity of the problem. The Nobel laureate P. W. Anderson is quoted as saying "The deepest and most interesting unsolved problem in solid state theory is probably the theory of the nature of glass and the glass transition."[5] Indeed, a generally accepted theoretical description of the glass transition was selected by *Science* on its 125th anniversary as one of the 125 important scientific problems to be resolved.[6]

Glass Transition Phenomenon

Before moving on to introduce the general phenomenon of the glass transition, the author states that neither does he pretend to be a glass transition theorist that understands in full depth all aspects of most current theories, nor is he a mathematics savvy who is capable of mastering the sophisticated mathematical models behind the theories. Only the qualitative, intrinsic features of the glass transition phenomenon will be described.

When a liquid is quenched fast enough, it is supercooled to a glass. This is because the molecules do not have time to react to the fast temperature drop and rearrange themselves into a more thermodynamically stable crystalline phase, thus avoiding the thermodynamic first-order phase transition and resulting in a disordered amorphous material. Most matters can form glasses, given the quench rate is fast enough. A prominent example is amorphous water.[7] Liquid water must be cooled to its T_g (about 136 K or -137 °C) in milliseconds to prevent the spontaneous nucleation of crystals.

Although the nature of glass formation process is still mysterious, an established consensus is that the observed glass "transition" is not a *bona fide* thermodynamic phase

transition, but rather a temperature range through which a material transforms from a viscous liquid at equilibrium to a disordered solid matter.[8] The empirical T_g is only defined as the temperature below which the material becomes too viscous to flow and appears solid on a "reasonable" time scale: by a typical convention T_g corresponds to a temperature at which the viscosity of the material reaches 10^{13} Poise or the relaxation time is of the order of 10^2 seconds. Hereafter, we distinguish between a supercooled liquid which refers to the highly viscous, solid-like liquid at temperatures above T_g, and a glass which is the amorphous solid below T_g. In practice, T_g is usually measured using Differential Scanning Calorimetry (DSC) following Standard ASTM E1356, "Standard Test Method for Assignment of the Glass Transition Temperature by Differential Scanning Calorimetry".

So what is there to be explained about the glass transition? Several universal observations during glass transition are found throughout the whole glass family, be them small molecular glasses, metallic glasses, or polymeric glasses. The first and foremost significant feature is the up to 14 orders of magnitude increase in a continuous manner in the main (α) relaxation time τ_α from a few picoseconds at the melting temperature T_m to 100 seconds at the glass transition temperature T_g. This increase is even more remarkable considering the corresponding temperature decrease $\Delta T = T_m - T_g$ is, as a rule of thumb, about $\frac{1}{3}T_m$, not a large value if one considers $k_B T_m$ as the typical energy scale. The drastic increase in τ_α is accompanied by a concomitant, comparable increase of the shear viscosity η, which is understandable considering a simple Maxwell model where η and τ_α are related by $\eta = G_\infty \tau_\alpha$, where G_∞ is the instantaneous elastic modulus.

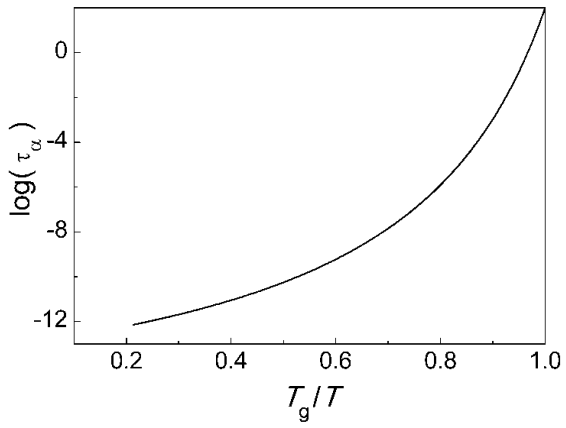

Figure 1. The Angell plot of the super-Arrhenius behavior of glass transition.

The temperature dependence of τ_α or η typically becomes more steep when temperature approaches T_g from above, and this "super-Arrhenius" behavior is shown in Figure 1. The figure is called the Angell plot and the curve can be closely approximated by the empirical Vogel-Fulcher-Tammann (VFT) expression,

$$\tau_\alpha(T) = \tau_0 \exp\left(\frac{DT_0}{T-T_0}\right), \text{ or,}$$

$$\eta(T) = \eta_0 \exp\left(\frac{DT_0}{T-T_0}\right) \qquad \text{Equation 1}$$

where T_0 is a non-zero temperature below T_g, and D is a material-specific constant. The expression is also called Williams-Landel-Ferry (WLF) formula in the polymer science community. The slope of the curve at T_g was defined by Angell as the "fragility"[9], an important parameter of glassy materials. The fragility of a material describes the deviation of the dynamics of glass molecules from Arrhenius behavior. Numerous attempts have been made over the years to look for empirical correlation, with varying degrees of robustness, between fragility and other glassy material properties, such as the

degree of non-exponential behavior of the relaxation function[10,11,12], the heat capacity jump at T_g, and non-ergodicity parameter[13]. Nowadays, the notion of fragility appears in connection with the temperature evolution of transport properties.[14,15,16,17]

Cooperatively Rearranging Regions

If one tries to define an effective activation energy for the glass formation process using the slope of the curve in Figure 1, one finds that this energy increases when the temperature decreases. This increase of energy barriers immediately suggests that the glass transition is a collective phenomenon, or, when glassy polymers are concerned, a long range cooperative motion. This led Gerold Adam and Jullian H. Gibbs to postulate the Adam-Gibbs (AG) entropy model[18], one of the classical phenomenological models to explain the glass transition phenomenon. In this model, the temperature dependence of relaxation behavior in glass forming materials is explained in terms of the temperature variation of the size of the *cooperatively rearranging region* (CRR). The effective activation energy for the relaxation of this CRR is equal to the typical energy barrier per molecule, which is taken as independent of temperature, multiplied by the number of molecules that constitutes the CRR. The latter is then determined by configuration restrictions in these glass forming materials and is inversely proportional to the *configurational entropy* per molecule $S_c(T)$, as shown in the following equation:

$$\tau_\alpha(T) = \tau_0 \exp\left(\frac{C}{TS_c(T)}\right) \qquad \text{Equation 2}$$

where C is a constant. In practice, because the configurational entropy S_c cannot be determined from experiments, the excess entropy of a glass with respect to its corresponding crystal, S_{ex}, is usually employed instead.

Extrapolation of the experimental S_{ex} curve below T_g apparently indicates that the S_{ex} vanishes linearly at some finite temperature, called T_K, where the subscript stands for Kauzmann, who recognized T_K as an important temperature for the physics of glasses.[19] For most glasses, T_K is in remarkable coincidence with T_0, the temperature constant in the VFT equation: the ratio T_K/T_0 remains close to 1 for materials with T_g's that vary from 50 to 1000 K. This is in fact one of the strongest experimental arguments for the AG entropy model, although Tanaka[20] questioned the validity of this relationship.

Static and Dynamic Correlation Lengths

The collective, or cooperative, nature of the glass transition has been at the core of research interest for many years. Recently, there has been a major effort to go beyond heuristic or *ad hoc* definitions of length scale in glass-forming materials, such as the cooperative length of the CRR introduced in the AG model introduced above. However, after several decades of intensive research, an "amorphous order" related to this length scale in the glassy state cannot be identified. The *a priori* difficulty lies in the fact that, despite the dramatic change in the dynamics, the static structure in the supercooled regime is not much different than that in the glassy state; a snapshot of a supercooled liquid configuration looks just like a glass configuration.[21] A structure factor that measures the spatial correlations of particle positions does not show any diverging peak at glass transition, in contrast with what happens during a crystallization phase transition. Therefore, until now there have been no strong indications of a diverging static length scale, or a growing structural correlation, as one approaches the glass transition.

On the other hand, more progress has been made concerning the growing correlations in the dynamics. It has been realized that the dynamics can be described by

introducing appropriate correlation functions which are in principle computable. Information on the corresponding "dynamical" correlation length can be extracted from these functions that describe how far the dynamics at a given point in space affects the dynamics at another point.[22,23,24] So far the most widely studied correlation function is a four-point correlation function G_4, which measures the spatial correlation of a dynamic two-point correlation, C_2. Experiments and numerical simulations known to date suggest that no spatial anomaly of any kind appears in C_2 as the glass transition is approached, but the measurements of χ_4, the dynamic susceptibility of the four-point correlation function, have indicated that dynamics becomes spatially increasingly correlated when temperature decreases. χ_4 is directly proportional to the variance of the spontaneous fluctuations of C_2 averaged over a volume V, which is of order $\xi^{2-\eta}/V$, where ξ is the length scale over which C_2 is significant correlated. The study of the evolution of G_4 and the growth laws of χ_4 and ξ contains useful information to unveil the complexity of the relaxation processes.[25] Furthermore, the growth of ξ suggests that the glass transition is indeed a collective phenomenon characterized by the growing time scales and length scales. However, it remains to establish a clear and conclusive understanding of the relationship between the increasing length scale obtained from G_4 and the growing relaxation time as well as the viscosity.

Dynamic Heterogeneity

Another significant feature of glass transition is dynamic heterogeneity, which is characterized by nontrivial spatiotemporal fluctuations of dynamics in supercooled liquids and glasses. The phenomenon now plays a central role in modern descriptions of glasses.[26,27] The discovery of the existence of dynamic heterogeneity stemmed from the

search for an explanation of the non-exponentiality of relaxation processes in glasses, which is related to the existence of a broad relaxation spectrum. For example, the temperature evolution of the imaginary part of the dielectric susceptibility of a glass former benzophenone measured over more than 10 decades of relaxation times is shown in Figure 2.[28] The dielectric susceptibility is related by the fluctuation-dissipation theorem to the time correlation of polarization fluctuations. Fittings to the data suggest that at high temperature the dynamics is represented well by an exponential relaxation in the time domain, whereas when temperature is decreased the relaxation spectra become broad and strongly non-exponential and exhibit "fat" tails (note the curves' different shapes). In fact, the low temperature curves can be well fitted in the time domain for times corresponding to the α relaxation with a stretched exponential function $\exp\left[-(t/\tau_\alpha)^{\beta_K}\right]$ ($\beta_K < 1$), which can be decomposed into a series of simple exponential decays with fast and slow decay rates that are reflective of fast and slow dynamics within the glass.

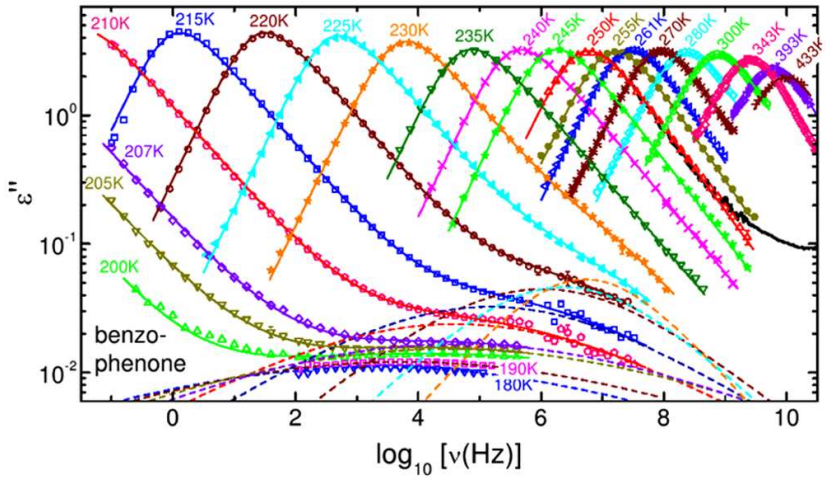

Figure 2. Temperature evolution of the dielectric susceptibility of the glass-former benzophenone measured over more than 10 decades of relaxation times.[28,28] Dynamics slow down dramatically as temperature is decreased and relaxation spectra become broad

and non-exponential at low temperature. Note the existence of additional "secondary" relaxation processes (reproduced from reference with permission[26]).

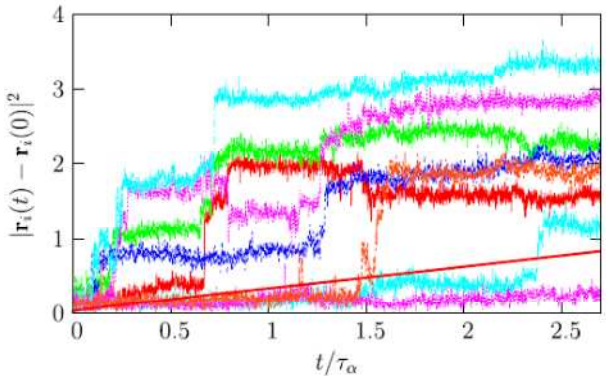

Figure 3. Time-resolved squared displacements of individual particles in a simple model of a glass-forming liquid composed of Lennard-Jones particles above its T_g (reproduced from reference with permission[26]).

Dynamic heterogeneity is more clearly revealed in computer experiments, which in recent years played an increasingly important role in glass transition studies.[29] Molecular dynamics can now be resolved in both space and time by computer simulations. Figure 3 shows the squared displacements of individual particles as a function of time in a simple model of a glass forming material composed of Lennard-Jones particles above its T_g.[26] The particle trajectories are composed of long periods of time during which particles vibrate around well-defined positions, separated by rapid jumps that are widely distributed in time and displacement. A two-dimensional spatial map of single-particle displacements recorded during the simulation of a binary Lennard-Jones mixture, shown in Figure 4, clearly demonstrates that the dynamics within a glass varies from one particle to another. More importantly, Figure 4 also unambiguously reveals the existence of spatial correlations between the dynamic fluctuations, corroborating the numerical calculation results from four-point correlation functions.

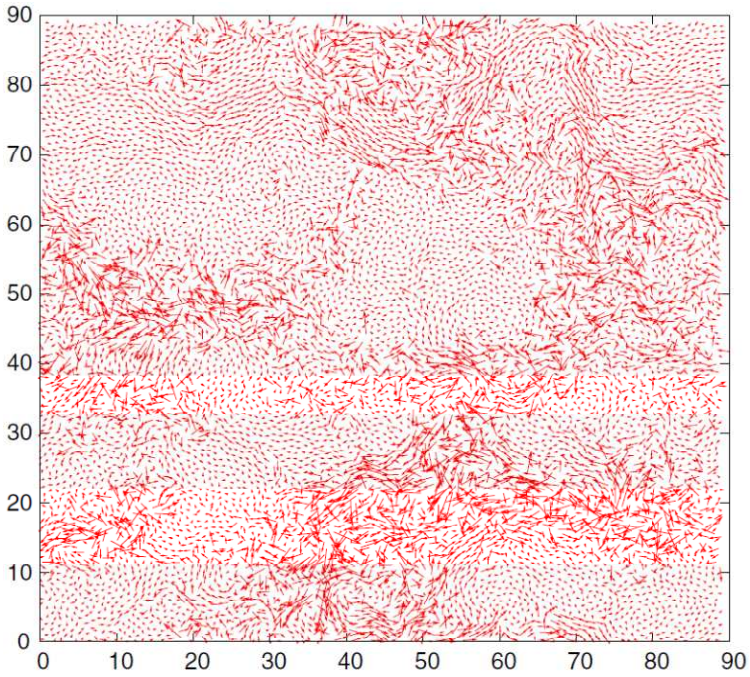

Figure 4. Spatial map of single-particle displacements in the simulation of a binary mixture of Lennard-Jones mixture in two dimensions. Arrows show the displacement of each particle in a trajectory of length comparable to the structural relaxation time. The map reveals the existence of particles with different mobilities during relaxation, but also the existence of spatial correlations between these dynamic fluctuations (reproduced from reference with permission[26]).

A physical characterization of dynamic heterogeneity requires the determination of the typical lifetime of the heterogeneities, as well as their typical length scales. This type of measurements of molecular dynamics resolved in time and space, as demonstrated in Figures 3 and 4 by computer simulations, is out of reach of most experimental techniques. Only a few pioneering works have been performed to obtain temporally or spatially resolved dynamic information using four-dimensional (4D) NMR spectroscopy,[30,31,32] or by directly probing fluctuations at the nanoscopic scale using microscopy techniques. Vidal Russell and Israeloff reported direct observations via atomic force microscopy of molecular cooperativity near the glass transition of polyvinylacetate (PVAc), using nanometer-scale probing of dielectric fluctuation.[33] The

results suggest that cooperativity takes the form of nanometer-sized transient molecular clusters and the signals reveal that the dynamics is intermittent in time: It switches between moments with intense activity and moments with no dynamics at all, indicating that extended regions of space indeed transiently behave as fast and slow regions. In the 4D NMR experiments by Spiess et al., the spatial information is gained from a proton spin diffusion experiment combined with two 2D ^{13}C exchange sequences via appropriate back and forth transfer of magnetization between ^{13}C and ^{1}H spins.[34] Their measurements showed that the molecular clusters near T_g have a diameter of 3 ± 1 nm in PVAc, compared to 1 nm in glycerol, a small molecule glass.[31,32] The time scale of this dynamic heterogeneity on the other hand was determined by 4D solid-state exchange NMR experiments to be the same as the α relaxation process itself.[30] Although these experiments yield undisputed information about the typical lifetime of dynamic heterogeneities as well as the dynamic correlation length scale, they are quite difficult to perform. Besides, the supermolecular lengths, as determined from 4D NMR experiments and some other calculations[27], never seem to grow bigger than a few nanometers, thus rendering them hard to find experimentally.

One influential phenomenon related to the existence of dynamic heterogeneity is the decoupling of self-diffusion and viscosity. It has been shown experimentally that, fragile liquids on supercooling exhibited a breakdown in the scaling between the diffusion constant D_s and the shear viscosity η.[17,35] In the high-temperature liquid, self-diffusion and viscosity are related by the Stokes-Einstein relation, $D_s\eta/T$ = const. It is commonly found that D_s^{-1} does not increase as fast as η/T so that at T_g the product $D_s\eta/T$ is 2-3 orders of magnitude larger than its Stokes-Einstein value. A natural explanation of

this effect is that different observables probe differently the underlying distribution of relaxation times.[36] For example, the self-diffusion coefficient of a tracer particle is dominated by the more mobile particles, whereas viscosity and other measures of structural relaxation probe the time scale needed for every particle to move. The study of dynamic heterogeneity is therefore of interest because a good transport property in mechanically robust materials is highly desired for applications such as breathable cloths, fuel cell films, etc. As mentioned above, a correlation between fragility and non-exponential relaxation behaviors of glasses seems to exist, although not on very solid ground.[10,11,12] More fragile liquids are characterized by broader relaxation spectra and therefore larger dynamic heterogeneity. Recent work by Sokolov and coworkers demonstrated that the temperature dependence of ionic conductivity can be decoupled from structural relaxation.[14,16] The strength of decoupling correlates with the steepness of the temperature dependence of structural relaxation, i.e., the fragility. They speculated that employment of more fragile polymers might lead to the design of polymers with higher ionic conductivity.

To summarize, the glass transition is characterized by the dramatic increase in α relaxation time and viscosity when temperature approaches T_g, following a super-Arrhenius behavior. Adam and Gibbs, through defining a conceptually attractive cooperatively rearranging region, related the collective behavior to the configurational entropy of the system. This phenomenological model gives a satisfactory explanation on the super-Arrhenius behavior of relaxation times, but it was not constructed within a solid equilibrium statistical mechanics framework, and has received many critiques.[37] Efforts in the past decades have been to find a static length scale or a dynamic length scale

defining the collective behaviors of glass transitions. Although it remains unclear whether a correlation in the static structure exists, numerical calculations, especially the studies of multiple-point correlations, demonstrate that dynamics are spatially correlated, with correlation length growing upon decreasing temperature towards T_g. Another focus of research in recent years is the study of dynamic heterogeneity during glass transition. Dynamic heterogeneity is related to the presence of both fast and slow dynamics within glassy materials, which have been clearly confirmed in molecular dynamics simulations. However, experimental determination of spatially and temporally resolved dynamics is still rare due to technical difficulties and the size of heterogeneity. *A single theory that fully grasps the characteristics of glass transition is so far unavailable.*

Secondary Relaxations

Most glass transition theories focus on the dynamic development approaching T_g from the high temperature liquid side because of the fascinating slowing down of α relaxation dynamics. However, the dynamics are also interesting when viewed from the solid side in the glassy state where cooperative α relaxations are frozen in because the thermal energy k_BT is not able to activate the collective motions. In particular, there are some secondary molecular motions in the glassy state. These high frequency processes are already present but convoluted with the α relaxation in the liquid or supercooled state, and only become identifiable when the temperature drops blow T_g.[38]

Secondary Motions

Secondary relaxations in polymers are often thought to be “simple motions” of trivial origins, involving only part of the molecules such as side group motions, short segmental motions, or simple phenylene ring rotations and methyl group rotations.

Unlike α relaxations, these motions usually follow the Arrhenius-type temperature dependence of motional rates, with an activation energy E_a:

$$\tau(T) = \tau_0 \exp\left(\frac{E_a}{RT}\right) \qquad \text{Equation 3}$$

where R is the gas constant.

Despite of their simple nature, secondary relaxations exhibit different degrees of cooperativity, *i.e.*, short range cooperative characteristics. Starkweather suggested that the correlation lengths of cooperative motions were reflected in their activation energies.[39] By combining the Eyring equation and the Arrhenius equation, the activation energy of a secondary motional process can be expressed as:

$$E_a = RT_\beta \left[1 + \ln\left(\frac{kT_\beta}{2\pi hf}\right)\right] + T_\beta \Delta S \qquad \text{Equation 4}$$

where T_β is the temperature of maximum relaxation, f is the frequency (τ_c^{-1}), k is the Boltzmann constant, and h is the Plank's constant. Here, ΔS is defined as the configurational entropy that a molecular motion invokes, and a larger second term on the right side of the equation reflects a higher degree of cooperativity of the molecular motion studied. On the other hand, the first term on the right side defines the activation energies for simple motions, $E_{a,simple}$, as shown in Equation 5:

$$E_{a,simple} = RT_\beta \left[1 + \ln\left(\frac{kT_\beta}{2\pi hf}\right)\right] \qquad \text{Equation 5}$$

$E_{a,simple}$ are used to create a zero activation entropy line which distinguishes simple from cooperative motions. The line in Figure 5 shows the zero entropy line according to Equation 5 where a value of f = 1 Hz is used. Activation energies for simple motions lie

on the line; activation energies for cooperative motions are above it. The higher the activation energies are above the line, the more cooperative the motions are. Comparison of E_a to $E_{a,simple}$ values allows the determination of ΔS for each motion. The cooperativity of a motion based on the distance from the zero activation entropy line is defined as:

$$\Phi = \frac{T_\beta \cdot \Delta S}{E_a} \times 100\% \qquad \text{Equation 6}$$

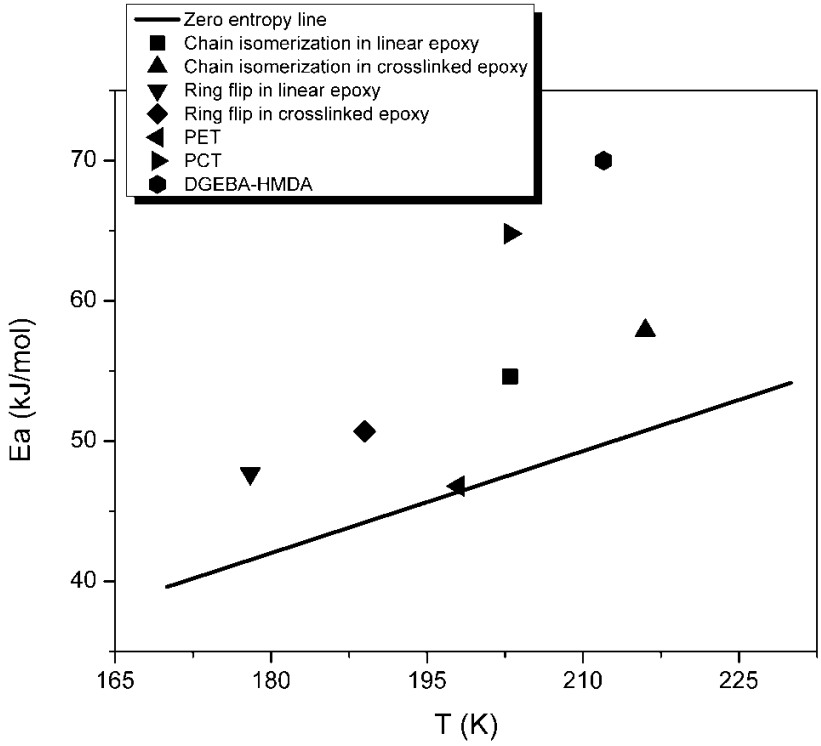

Figure 5. Starkweather plot showing the E_a for several cooperative motions as well as the zero entropy line.

Johari-Goldstein β Relaxations

There is one type of secondary motions that is of non-trivial origins, but involves motions of an entire molecule, or a repeat unit in the case of polymers. This type of motions was first discovered by Johari and Goldstein in their observation of secondary

relaxations in rigid molecules such as toluene or chlorobenzene that do not have intramolecular degrees of freedom.[40] Therefore the secondary relaxations in the glassy state of such molecules must originate from motions of the entire molecules. It is later found out that such motions are universally present in all types of glasses.[41,42] In non-rigid glass formers, such relaxations involve the motions of essentially all parts of the basic structural unit, and it is not required that all parts have to move altogether rigidly. For example, the secondary relaxations in the poly(methyl methacrylate) (PMMA) and poly(ethyl methacrylate) (PEMA) involve not only a 180° flip of pendant carboxyl group of the side chain, but also the rocking motions of the repeat unit on the main chain, the amplitude of which increases with temperature.[43,44,45] In honor of Johari and Goldstein's important discovery, this type of secondary motions of glasses is designated as Johari-Goldstein (JG) β relaxations.[46]

JG β relaxations bear a strong connection to α relaxations in all the dynamic properties.[42,46] The following example demonstrates such connection: Usually, elevated pressure *P* slows down the α relaxation, but this effect can be compensated by raising temperature *T*. Therefore, different combinations of *P* and *T* can give rise to a same α relaxation time τ_α. Under such conditions, the stretched exponential β_K which describes the shape of the α relaxation peak (see the Dynamic Heterogeneity section), and the JG β relaxation time τ_{JG} remain also unchanged, while other properties including density vary.[42,47,48] Therefore, JG β relaxations are believed to be coupled to α relaxations. In fact, the JG β relaxation bears a striking resemblance with the primitive α relaxation in the Coupling Model proposed by Ngai,[49,50] the latter considered the precursor of the cooperative α relaxation. The relaxation time of the primitive α relaxation τ_0, calculated

from the cooperative α relaxation time τ_α through the model, is found to be close to the experimentally determined JG β relaxation time τ_{JG}.[51] Meanwhile, the two relaxation times exhibit similar sensitive dependence on pressure and aging, in contrast with other secondary motions of trivial origins, which have relatively mild dependency. The similarity between the JG β relaxation and the primitive α relaxation has led to the general belief that JG β relaxation plays the important role as a precursor or local step of the cooperative α relaxation. One interesting empirical equation between the activation energy of the JG β relaxation and the T_g of the material is[52]

$$E_a^{JG} = (24 \pm 3)RT_g \qquad \text{Equation 7}$$

A more quantitative version of the equation can be derived based on a coupling model for glass transition.[53,54] Therefore, a good glass transition theory will need to take into consideration all the close connections between the JG β relaxation and the α relaxation

Potential Energy Landscape

Here, one of the statistical mechanics models for glass transition will be introduced that involves the generation of a "potential energy landscape" (PEL) image to explain and predict glass transition behaviors from high temperatures down into the glassy state. However, again, the statistical mechanics background of the model[55] will be shunned, and only general concepts and qualitative relevance to glass transition will be described.

The glass transition is featured by the existence of an exponentially large number of amorphous configurations, where different density fields give rise to different free energies *F*. The PEL is the hypersurface generated by scanning *F* over all possible values

of density profiles. A large number of studies have shown that the potential energy landscape becomes corrugated at low temperatures and characterized by many energy valleys and hills.[55,56,57,58] Each of these valleys and hills might further consist of small valleys and hills, i.e., local minima and saddle points. A metabasin is defined as a broad energy valley that is corrugated at the bottom. Figure 6a shows a simplified 2D representation of the PEL.

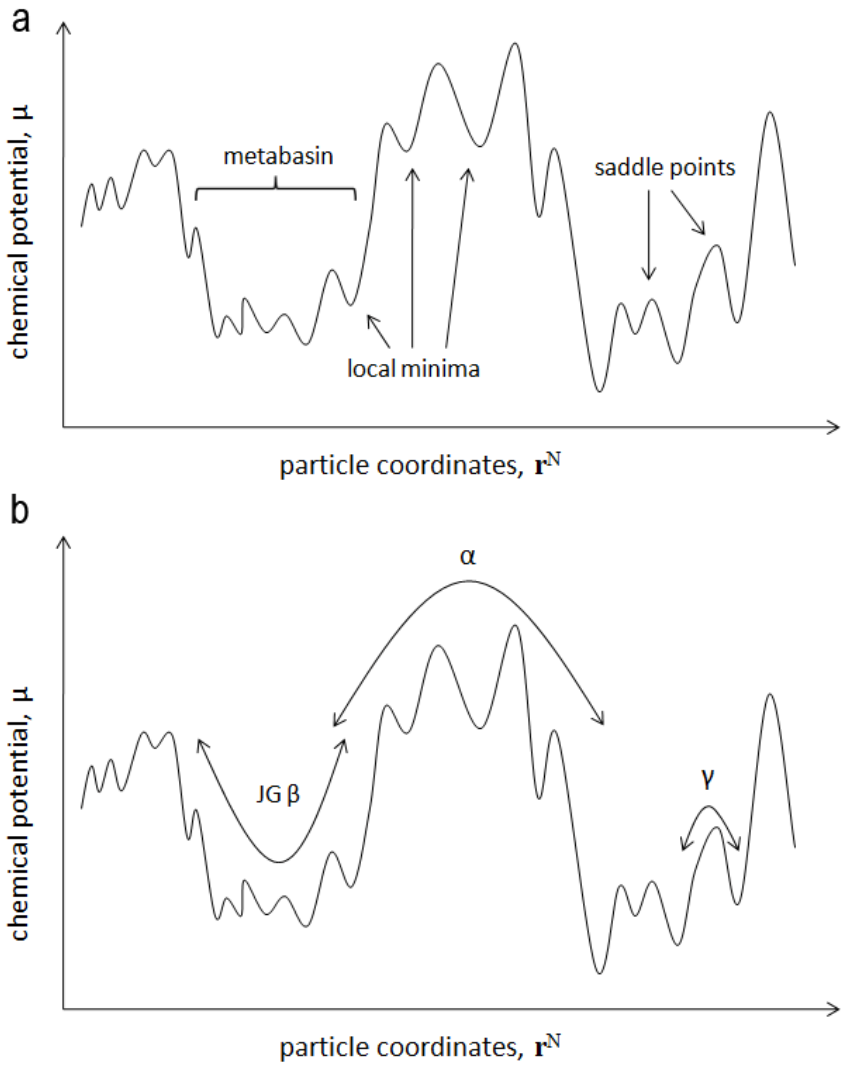

Figure 6. Simplified 2D representation of potential energy landscape.

Features of the PEL are related to the relaxation processes in glasses (Figure 6b). Molecular vibrations are readily described as molecules or functional groups attempting to escape local minima and transitions between neighboring minima represent γ-relaxations of trivial molecular origins. Molecular dynamics simulations gave evidence that transitions between metabasins are involved in the α process.[59] The origin of the JG β relaxation is more controversial: it was speculated that it resulted from either transitions between local minima[60] or from exploration of metabasins[61], but this hypothesis has been questioned, because it was noticed that the known activation energies for the JG β relaxation are too high for intra-basin processes.[55] Goldstein suggested that the JG β relaxation also involved transitions between metabasins, but with lower energy barrier heights.[62] The difference between the cooperative α relaxation and the JG β relaxation could be that the α process involves ergodic transitions that can lead to all accessible basins of the PEL and the JG β relaxation is limited to small clusters of metabasins connected by somewhat lower barrier heights and from which ergodic pathways are not available at the temperature at which the JG process is usually observed.[62,63,64]

NMR Study of Molecular Dynamics

The quest for understanding the relationships between macroscopic properties and molecular dynamics in solid polymers has piqued the interest of scientists since the founding of polymer science. Several modern analytical techniques are currently widely employed to investigate the structure and dynamics of polymers. With the advancement of characterization techniques, the traditional separation between the determination of structure and the elucidation of dynamics becomes more and more artificial. Instead, the

determination of structure and morphology can facilitate the understanding of dynamic properties and *vice versa*.[4] In fact, determination of the molar mass by dynamic light scattering[65], well-established in the polymer field, provides an instructive example as there the size of the macromolecule (structure) is determined from measuring their translational diffusion, i.e., a dynamic phenomenon. Among all the techniques that can probe the interplay between structure and dynamics in complex polymeric systems, nuclear magnetic resonance (NMR) spectroscopy stands out to be a particularly powerful and versatile tool in polymer science.

In the late 1970's, Jacob Schaefer and coworkers demonstrated that molecular motions in solid polymers can be studied through solid-state ^{13}C NMR spectroscopy, and they were the first scientists to attempt to relate molecular motion data from NMR spectroscopy to mechanical properties.[66,67,68] Solid-state NMR spectroscopy is well suited to study molecular motions not only because of its advantageous site-selectivity, but also because of the orientation dependence of various anisotropic spin interactions. Since then, the application of the technique to investigate molecular motions in solid polymer abounds. So far the NMR studies of molecular motions and cooperativity in bisphenol A polycarbonate (BPAPC) and poly(methyl methacrylate) represent the highest level of achievements.[69,70,71]

Various NMR experiments (^{1}H, ^{2}H, and ^{13}C solid-state NMR) have been used to investigate the secondary transitions of BPAPC, and have provided lots of information on the motions of methyl, phenyl ring and carbonate groups in solid BPAPC. The effect of intermolecular packing has also been clearly evidenced. By combining all the results, a comprehensive picture of the motions occurring in BPAPC is reached. The γ relaxation

at very low temperatures is associated with the rotations of the methyl groups of the isopropylidene unit around the C_3 axis. The β transition at around -100 °C is more complex: it is believed to involve the intra-molecular cooperative motion of the carbonate groups and the two phenyl rings attached to the same isopropylidene unit, accompanied by small amplitude (rms 10° at room temperature) main chain fluctuations.

The β transition of PMMA, determined from similar NMR experiments, is attributed to jumps of the ester side group. The jumps, however, require the reorientation of the main chain to remove sterical restrictions that otherwise prohibit the accommodation of the side group in the new orientation. This finding, together with the main chain fluctuations seen in BPAPC, gives rise to an interesting question in polymer science: whether or not β relaxations of polymers necessarily involve the participation of main chains. However, due to the localized nature of NMR spin interactions detected in relatively simple NMR methods, no definitive answers can be given regarding the extent of cooperativity involved in secondary relaxations of polymers.

Research Overview

The goal of this research is to gain a better understanding of the structure-dynamics-property relationships of glassy epoxy networks. Specifically, the molecular motions of different molecular groups within two epoxy networks of isomeric structures will be investigated through solid-state deuterium (^2H) NMR spectroscopy to explain the differences in their macroscopic properties. The isomeric networks are crosslinked epoxies fully cured at 1:1 stoichiometric equivalents of diglycidyl ether of bisphenol A (DGEBA) with 3,3'-diaminodiphenylsulfone (33DDS) or 4,4'-diaminodiphenylsulfone (44DDS), denoted hereafter as 33A and 44A, respectively. The structures of the two

networks are shown in Figure 7. Previous work by the Wiggins Research Group has shown that the 33A system has a higher modulus but a smaller compression yield strain, and exhibits a glass transition temperature 40 °C lower than that of the 44A material.[72] In addition, positron annihilation lifetime studies show that the 33A system has a smaller hole-size free volume.[73] These data suggests the 33A epoxy behaves like an anti-plasticized 44A system.

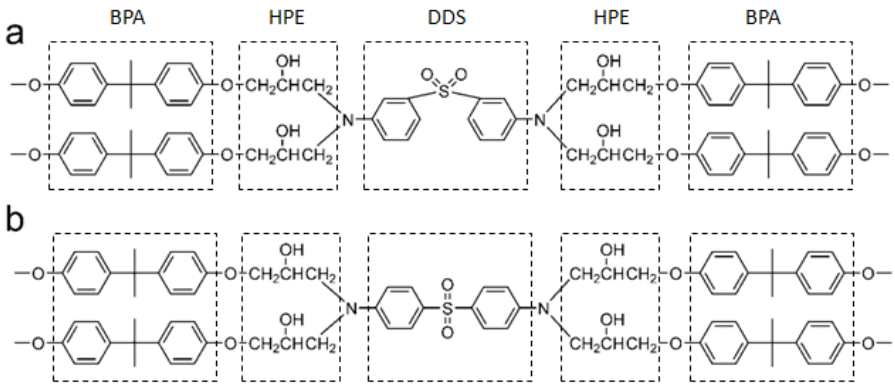

Figure 7. The molecular structures of the isomeric epoxy networks under study: (a) 33A, and (b) 44A.

Solid-state ^{2}H NMR spectroscopy is employed as the main research tool. 33A and 44A epoxy networks were synthesized with targeted molecular groups deuterated; specifically, 33A and 44A networks with deuterated BPA phenylene rings, deuterated DDS phenylene rings, and deuterated HPE moieties, were synthesized for comparison in the dynamics in these molecular units. In Chapter II, the technical background on solid-state NMR spectroscopy was introduced with an emphasis put on ^{2}H line shape analysis. The understanding of NMR principles and techniques constitutes a good part of the author's graduate endeavor and functions as a basis for the dissertation research. In Chapter III, the BPA phenylene ring motions in 33A and 44A networks were studied

through quadrupolar echo line shape analysis to exhibit very similar dynamic behaviors in the glassy state. The study discovered a growing correlation length of molecular motions within the epoxy networks which finally developed into glass transition. In Chapter IV, the DDS phenylene ring motions in the two epoxies were characterized through similar routes. The anti-plasticization effect observed in 33A is attributed to the meta-substitution on the 33DDS diamine phenylene rings which suppresses large amplitude motions and leads to more compact packing in 33A. In Chapter V, the HPE chain molecular motions in 33A and 44A were studied. The HPE segments start to exhibit different dynamics a temperature lower than the corresponding temperature for BPA rings, due to the proximity of HPE groups to the crosslink, above which the HPE motions in 33A are slower because of its connection to the relatively static 33DDS moiety. A summary is given in Chapter VI.

CHAPTER II

TECHNICAL BACKGOUND ON SOLID-STATE NMR SPECTROSCOPY

Solid-state NMR spectroscopy is a powerful probe of atomic-level structure and dynamics in polymeric systems.[74,75,76] NMR spectroscopy combines a number of features that make it an almost ideal tool: it is non-destructive, sample preparation is easy, and the possibility to observe different nuclei and isotopes provides extreme structural selectivity. Moreover, dynamic features can be studied over many decades of characteristic time scales, from picoseconds to minutes, and length scales from inter-atomic distances in the 100 pm range up to a meter or so in NMR imaging.[76,77]

NMR Signals

The nature of NMR signals will be introduced first, the knowledge of which, according to the author's personal experience, will promote unambiguous understanding of the subject. Readers are highly recommended to read the book *Spin Dynamics* written by Malcolm H. Levitt for NMR fundamental principles if interested.[78]

Nuclei possess the property of spin which, like mass and electric charge, is an intrinsic property. Nuclear spin is in some ways similar to a tiny magnet, the "north pole" of which defines the spin polarization. For an ensemble of nuclei or spins, spin polarization will point in all directions, as shown in Figure 8. When a magnetic field B is applied, the spin polarizations start to move on a cone, keeping a constant angle between the spin polarization and the field. The interaction of the spin with the magnetic field is called the Zeeman interaction, with the motion of the spins called precession. *In NMR spectroscopy, it is the precession frequencies of nuclei that are detected.*

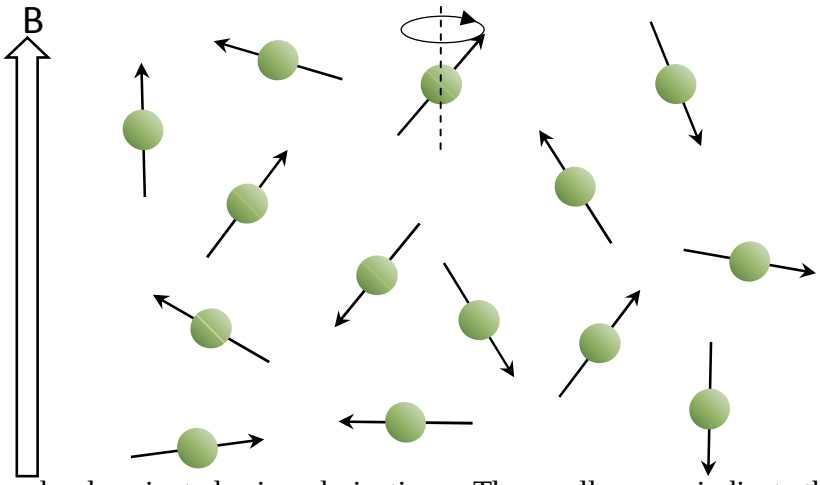

Figure 8. Randomly oriented spin polarizations. The small arrows indicate the spin polarizations. The large arrow is the direction of the applied magnetic field. The circle with one of the particles is representative of the spin precession on a cone around the magnetic field.

The frequency of precession is linearly proportional to the strength of the magnetic field; each NMR-active nucleus is characterized by its gyromagnetic ratio γ: $\omega_0 = -\gamma B_0$, where ω_0 is termed the Larmor frequency, and B_0 is the magnetic field strength. For example, the magnetogyric ratios of ^{1}H, ^{2}H, and ^{13}C nuclei are 267.5, 41.1, and 67.3 × 10^{6} rad·s^{-1}·$Tesla^{-1}$, therefore when placed in a magnetic field of 9.4 Tesla, the ^{1}H, ^{2}H, and ^{13}C nuclei precess at frequencies of 400, 61.4, and 100 MHz, respectively. Modern NMR spectrometers utilize very strong super-conducting magnets having field strengths of 1 to 20 Tesla; in contrast, the Earth's magnetic field ranges from 25 to 65 × 10^{-6} Tesla.

Anisotropic Spin Interactions

If every nucleus precesses precisely at its Larmor frequency, NMR spectroscopy would not be interesting at all. In actual matters, nuclear spins are under the influence of their surroundings. Indeed, *the wealth of information accessible by NMR spectroscopy*

results from the fact that a variety of interactions of the nuclear spins with their surroundings can be exploited. The structural and dynamics information that can be extracted from solid-state NMR spectra is encoded via anisotropic spin interactions including the chemical shift anisotropy, homo- and hetero-nuclear dipole-dipole couplings, and quadrupolar interaction. The chemical shift provides the basis of site selectivity. Geometric parameters such as inter-nuclear distances as well as dihedral angles are encoded in the dipole-dipole coupling. Information concerning intramolecular mobility and orientation can be obtained via the quadrupolar coupling. The anisotropic nuclear spin interactions also offer a means to probe the alignment of molecular chains in partially ordered systems such as drawn fibers[79] or oriented liquid crystals[80]. The following paragraphs give a brief introduction of the nature of these interactions.[77, 78]

Chemical Shift. Nuclei are surrounded by electron clouds. An external magnetic field B_0 induces currents in the electron clouds, which in turn generate magnetic fields. A chemical shift is therefore the shift in the precession frequency of a nucleus due to the magnetic field generated by the movement of the electrons in the molecular structure. Because different molecular geometries have different electron structures, the chemical shift values provide important information on the structures of molecules. This is by far the most commonly used NMR method.

Direct Dipole-Dipole Coupling. A direct dipole-dipole coupling is the interaction between different nuclei simply because a nucleus itself is a magnet and generates a magnetic field. A nucleus that is spatially close to another nucleus, either of the same kind or different, experiences the magnetic field generated by the latter, which causes a

change in the precession frequency of the former. The interaction may be either intramolecular or intermolecular.

Electric Quadrupolar Interaction. This interaction is different in nature from the two interactions mentioned above in that it is related to the electric charge of a nucleus. For a nucleus with a spin number larger than ½, the distribution of electric charge on the nucleus is not spherically symmetric, but is instead quadrupolar in nature. This electric quadrupole moment of the nucleus interacts with the electric potential field, or to be specific, the electric field gradient (EFG), of the surrounding space. For quadrupolar nuclei, the quadrupolar coupling ranges from kHz to MHz.

Orientation Dependence of Spin Interactions

Anisotropic spin interactions have a well-defined orientation dependence. For couplings with magnitudes much weaker than the Zeeman interaction, first-order perturbation theory can be applied, and the resulting orientation dependent NMR frequency is given by:

$$\omega(\theta_\lambda, \phi_\lambda) = \omega_0 + \omega_{iso} + \frac{\delta_\lambda}{2}\left(3\cos^2\theta_\lambda - 1 - \eta_\lambda \sin^2\theta_\lambda \cos 2\phi_\lambda\right) \quad \text{Equation 8}$$

where ω_0 is the Larmor frequency, ω_{iso} is the isotropic frequency component, and the remaining terms describe the angular-dependent contributions. The magnitude of anisotropy is specified by δ_λ, whereas η_λ is the asymmetry parameter describing the deviation from axial symmetry. The subscript λ denotes the three nuclear spin interactions, namely, chemical shift anisotropy (CSA), dipole-dipole coupling (DDC), and quadrupolar interaction (QC). Each of these interactions is defined by a coordinate frame of reference, or the principal axis system (PAS), whereby the interaction tensor is diagonal. The orientation of the PAS with respect to the external magnetic field is

denoted by the polar angles θ_λ and ϕ_λ, as shown in Figure 9. In organic solids, the PAS are often directly linked to the molecular geometry. For example, the unique axis (λ_{zz}) of the ^{13}C CSA for aromatic rings is perpendicular to phenyl plane, whereas the λ_{zz} of the heteronuclear ^{13}C-^{1}H DDC or ^{2}H QC are directly along the C-H bond directions.[76]

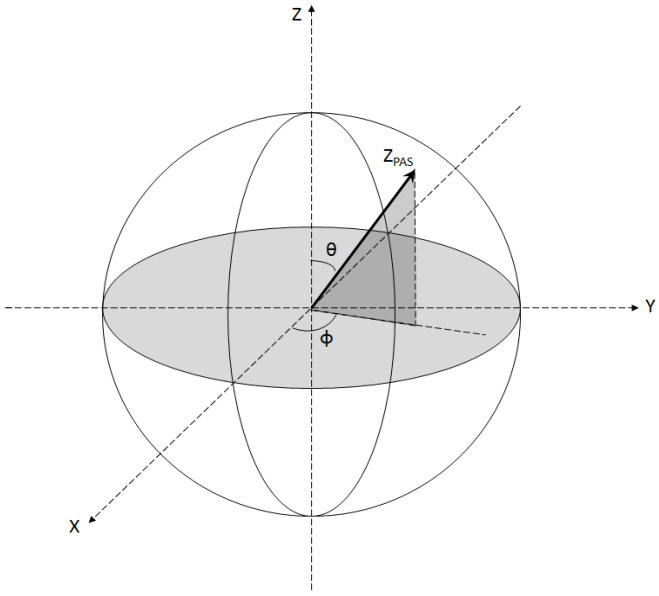

Figure 9. The illustration of the orientation (Z_{PAS}) of the principle axis system of a spin interaction with respect to an external magnetic field along the Z axis.

Static Powder Pattern

The powder average, with equal probability of spin orientation along every direction, yields a broad, yet characteristic NMR spectrum. If the spin ensemble is represented by a sphere, as shown in Figure 10a, spins oriented in the XY plane have the most population, and the spin quantity decreases towards the poles, where the spins have minimal populations. In a simplified case where ω_{iso} is 0 and the asymmetry parameter η is 0, the characteristic spectrum is shown in Figure 10b. The width of the spectrum reflects the magnitude of the anisotropic spin interaction.

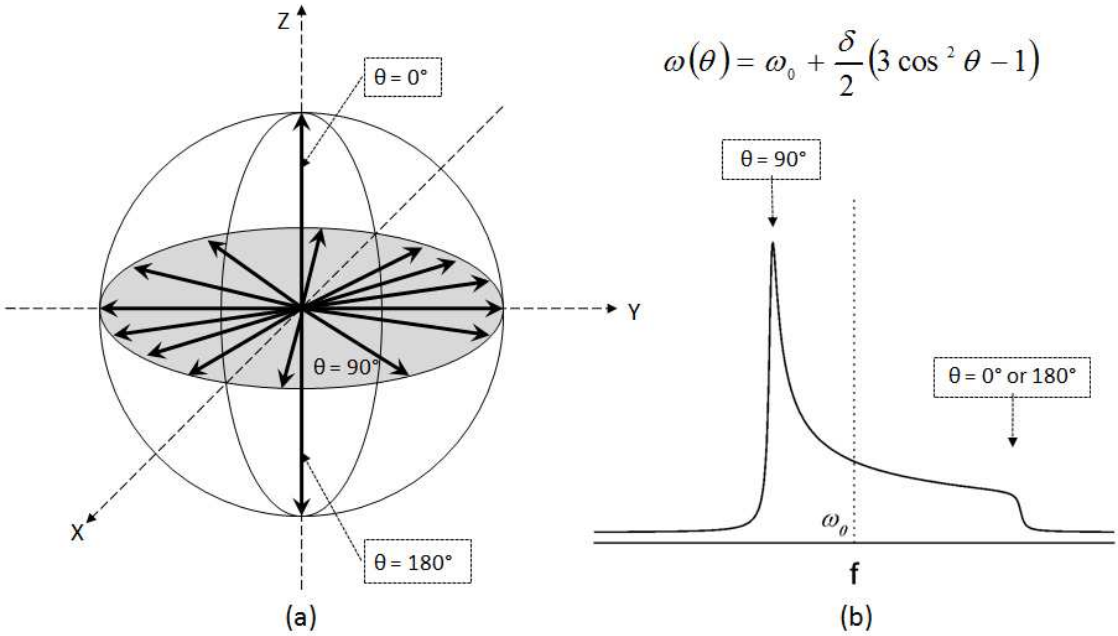

Figure 10. (a) Spin ensemble represented by a sphere where spins oriented equally along every direction, and (b) a static powder pattern from a spin interaction with single transition assuming an η value of 0.

The spectrum shown in Figure 10b is typical for, e.g., chemical shift anisotropy of spin-½ nuclei, where only one transition is detected. For the case of DD coupling, or a quadrupolar spin-1 nucleus, the characteristic static powder pattern is a superposition of two static powder patterns, one being the opposite of the other, as is shown in Figure 11. This is the Pake pattern. The frequency difference between the two 90° doublets equals δ, the intensity of the spin interaction.

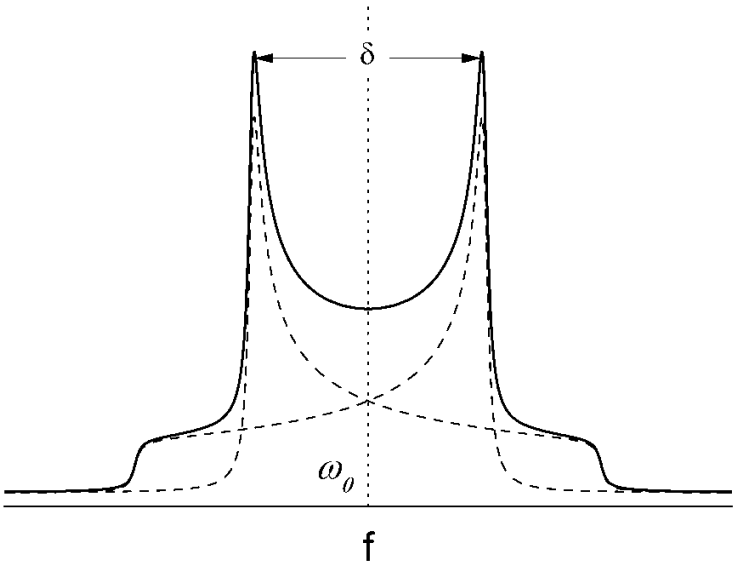

Figure 11. The static Pake pattern.

The width of the powder patterns varies with interaction being observed. The chemical shift anisotropy results for ^{13}C systems in powder patterns that are approximately 20 kHz at a field strength of 9.4 T. The magnetic dipole-dipole coupling of nuclei leads to broad NMR lines covering approximately 50 kHz for ^{1}H-^{1}H homonuclear coupling and approximately 25 kHz for ^{1}H-^{13}C heteronuclear coupling. For ^{2}H (I= 1) in C-^{2}H bonds the quadrupolar coupling leads to spectral splitting of approximately 250 kHz. Typical chemical shift anisotropy, dipole-dipole coupling and quadrupolar interaction static line shapes for samples undergoing slow molecular motions ($\nu_c << \delta_\lambda$) are shown in Figure 12; note that the chemical shift anisotropy line shape differs from the one shown in Figure 10b, due to a non-zero asymmetry parameter η:

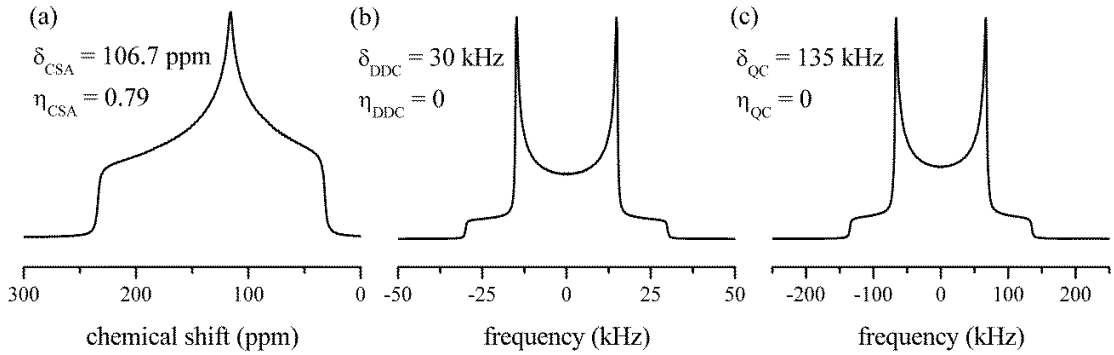

Figure 12. Typical chemical shift anisotropy, dipole-dipole coupling and quadrupolar interaction line shapes under no magic angle spinning.

Solid-state ^{2}H NMR Spectroscopy

The broadening effects of quadrupolar nuclei ($I > ½$), once viewed as a hindrance to performing such experiments in the solid state, are now often exploited to provide invaluable information on solid state chemistry, structure and dynamics. Deuterium (^{2}H), a spin $I = 1$ nucleus, has a relatively small quadrupolar coupling constant compared with other quadrupolar nuclei, typically around 10^5 Hz. Deuterium NMR spectroscopy is an established probe of site-specific dynamics for compounds where hydrogen atoms within a specific chemical moiety have been selectively deuterated.[81,82,83]

Strengths of ^{2}H NMR Spectroscopy

The main advantages of ^{2}H NMR methods can be summarized as follows[81]: (*a*) deuterons are well-defined nuclear spin labels, because the NMR parameters of ^{2}H are almost exclusively governed by the quadrupolar interaction with the electric field gradient tensor (EFG) at the ^{2}H site. Because the EFG originates from the electrons in the C-^{2}H bonds, it is entirely intramolecular in nature and, moreover, axially-symmetric ($\eta_{QC} = 0$) about the C-^{2}H bond in aliphatic compounds and to a good approximation in aromatic compounds as well. Thus, in ^{2}H NMR molecular order and mobility are

monitored through the orientation of individual C-^{2}H bond directions; (*b*) Deuterium NMR is highly selective. Actually the most severe drawback of the method, namely that isotopically enriched samples have to be used, can be turned into an advantage: By selective deuteration the mobility of different groups of the monomer unit can be studied separately; (*c*) Deuterium NMR yields almost unique information about molecular motions in polymers. Different types of motion can be clearly discriminated by analyzing ^{2}H line shapes. This will be described in more details later; (*d*) Motional heterogeneity can be detected not only in semi-crystalline materials but in glassy polymers as well. The signals from the mobile and rigid fractions can easily be separated, because the respective values for the spin-lattice relaxation rates often differ by at least an order of magnitude.

The dynamic range over which polymer dynamics can be followed by ^{2}H NMR spectroscopy is extraordinarily broad. Ultra slow motions with correlation times above 1 ms can be detected by 2D exchange NMR techniques. Rotational motions with well-defined reorientational angles give rise to elliptical exchange ridges, from which these angles can be read directly. The line shape analysis of the NMR spectrum is an important source of information. Pake patterns are observed for slow motions with correlation times above approximately 10^{-4} s. Faster motions result in distinctive distortions of the powder patterns, the distortions being dependent on both the geometry and correlation time of the molecular motion.[77] Finally, spin-lattice (T_1) relaxation experiments probe the dynamics at relatively high rates (10^8-10^{10} Hz), the scale being defined by the Larmor frequency. Figure 13 shows the time frames of different ^{2}H NMR techniques.

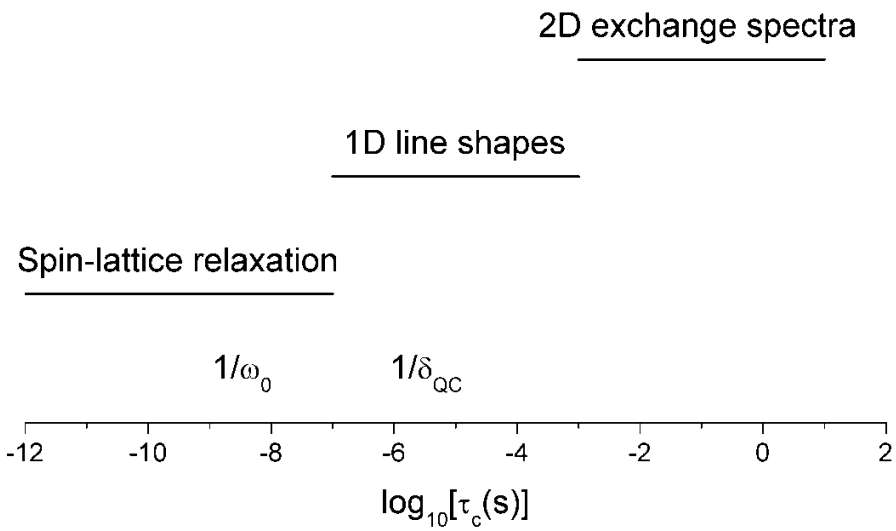

Figure 13. Time windows of different ^{2}H NMR experiments; Larmor frequency ω_0 and coupling constant δ_{QC} as typical for ^{2}H NMR are indicated (adapted from reference with permission[84]).

In the following paragraphs, the emphasis will be on one-dimensional (1D) line shape analysis, because *the time scale of glassy state molecular motions falls into the time window of line shape analysis*. Provided the spectrum contains only a single ^{2}H resonance, i.e. achieved by site-selective deuteration, changes in ^{2}H static powder spectra as a function of temperature due to the averaging of the quadrupolar interaction can be fitted to a model for the dynamic process, so as to yield the geometry, the rate constant and the activation energy.[85] This has been employed as the approach to study the glassy state molecular dynamics throughout this dissertation and have yielded abundant information on molecular motional details, thereby providing insights on the structure-dynamics-property relationships of crosslinked epoxy networks.

Quadrupolar Echo

For rigid sites in deuterated organic solids, the full width of the ^{2}H spectrum is over 200 kHz. Such a broad spectrum corresponds to an FID that decays rapidly to

almost zero within around 5 μs of the end of the pulse.[78] In practice, the capture of a rapidly decaying NMR signal is exceedingly difficult with the NMR signal coinciding with the release of accumulated electrical energy from the tuned circuit in the probe at the end of the pulse. Electrical interference makes it essentially impossible to detect the NMR signal until around 5 μs after a pulse has finished, which is too late to detect most of the ^{2}H NMR signal. This time interval is usually called the "dead time".

The problem is overcome by generating a spin echo to displace the NMR signal to a region in time that is well separated from the end of the pulse. In the case of a spin-1 ensemble, a suitable spin echo is generated by a sequence of two strong 90° pulses, with a relative phase shift of 90°, as is shown in the Figure 14 below:

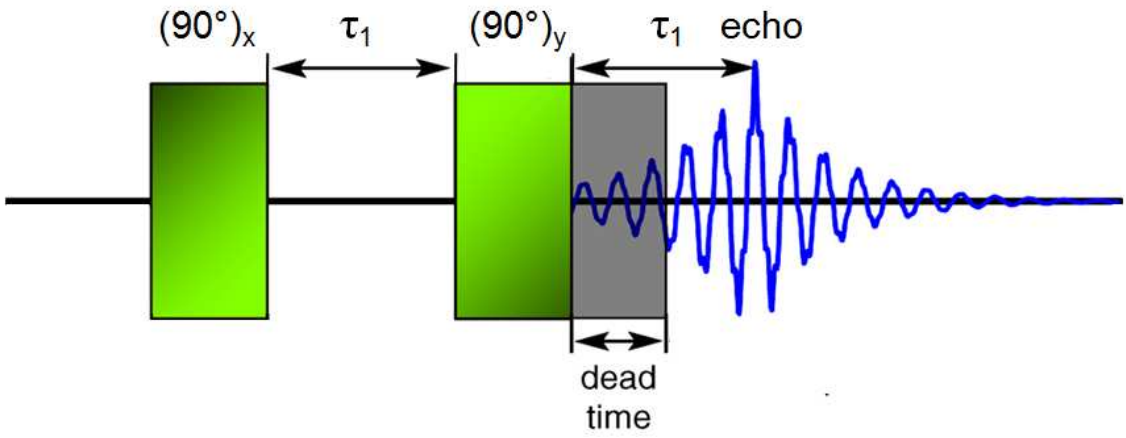

Figure 14. Quadrupolar echo pulse sequence (adapted from reference with permission[86]).

The first pulse rotates the spin magnetization by 90° about an *x* axis into the transverse *xy* plane. Then, the spins begin to diverge because of a process called transverse relaxation, which occurs due to both reversible and irreversible processes. After a time interval termed the echo delay (denoted τ_1) a second 90° pulse is applied

about the *y* axis (phase shift). The second pulse reverses the original free precession rates, so the spins now converge instead of diverge. As a result, reversible processes are refocused and a spin echo forms at a time τ_1 after the end of the second pulse. This type of spin echo is called a *quadrupolar echo*. Using an echo delay τ_1 longer than the dead time, quadrupolar echo experiments allow the entirety of the echo to be observed without any distortion from frequency-dependent phase shifts. Note that the quadrupolar echo cannot refocus all the signal, because irreversible decay processes are also involved. The specific pulse sequence only generates a quadrupolar echo in the case of spin-1 systems. It does not work for higher spin quantum numbers.

Time Scale Dependent Line Shapes

As stated above, anisotropic spin interactions are very sensitive to the *immediate* surroundings. A powder average in the static case yields a broad NMR spectrum that reflects the magnitude of the anisotropic spin interactions. However, when molecular motions are present, coalescence occurs between the lines corresponding to the different molecular orientations which arise during the course of the motion. This in turn causes distinctive distortions of the powder patterns, the distortions being dependent on both the geometry and correlation time of the molecular motion.[77]

The most significant line shape changes occur when the rate molecular motion ν_c is comparable to the quadrupolar coupling constant δ_Q.[76,77] This time scale is well known in solid-state NMR spectroscopy as the "*intermediate exchange regime*". In this regime, anisotropic transverse relaxation (T_2) resulting from fluctuations of the quadrupolar interaction becomes observable in ^{2}H line shapes as a result of the orientation dependence T_2 which distorts the solid echo decay.[87] Magnetization from those regions where $T_2 < \tau_1$

will not be completely refocused because of the interference of the molecular motions, but may be characterized by a quadrupolar echo refocusing efficiency. As an example, Figure 15 shows the line shapes and the refocusing efficiencies resulting from methyl group rotation at different rates. The line shape distortion and drastic signal reduction observed in the intermediate exchange range are highlighted in Figures 15c-g. These figures also show that while the spectrum of methyl rotation with motional rates lower than 10^3 Hz is the static Pake pattern, methyl rotation in the fast motion limit (> 10^7 Hz) yields a reduced but symmetric QC tensor, resulting in a Pake pattern with narrower splittings. Figure 16 shows the integrated signal intensity reduction factor, which is directly related to the refocusing efficiency as a function of methyl rotation rate. When ^{2}H NMR line shapes become independent of motional rate, in the slow ($\nu_c < 10^3$ Hz) and fast ($\nu_c > 10^7$ Hz) exchange limit, the reduction factors are near unity. The reduction factor reaches a minimum near $\nu_c = 10^5$ Hz, which is of the same magnitude of the quadrupolar coupling constant δ_Q of ^{2}H in the C-^{2}H structures.

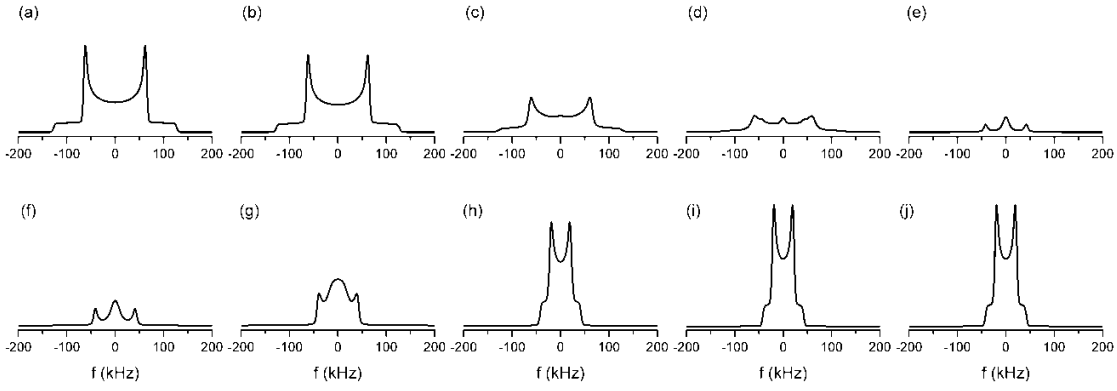

Figure 15. The figures show how the line shapes and the refocusing efficiencies change with different rates for methyl group rotation: log(ν_c) = (a) 2, (b) 3, (c) 4, (d) 4.5, (e) 5, (f) 5.5, (g) 6 , (h) 7, (i) 8, (j) 9.

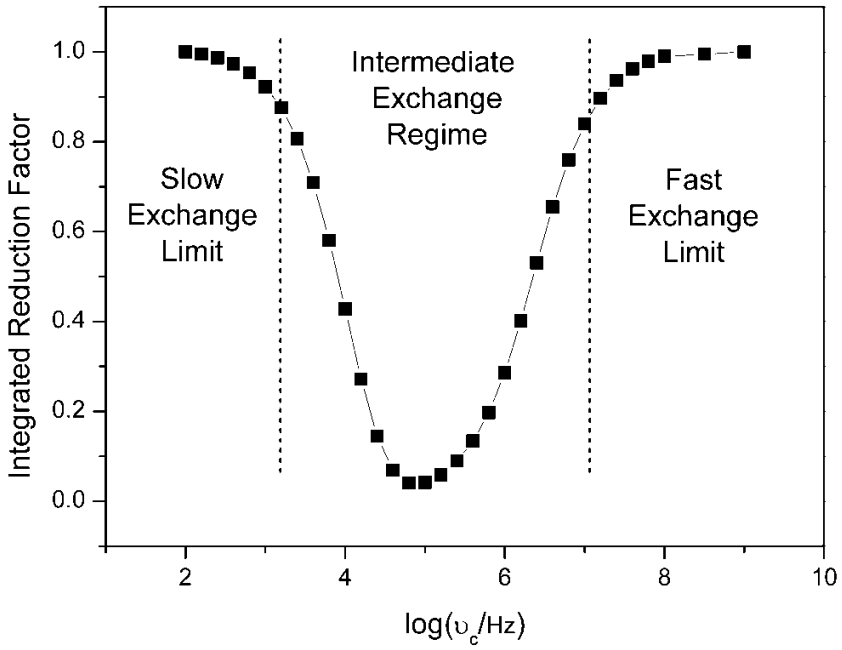

Figure 16. Integrated reduction factor as a function of methyl rotation rate.

The *fast exchange limit* is characterized by the condition whereby the motional rate is much larger than the rigid limit value δ_Q. When this condition is met, time evolution is governed by the quadrupolar coupling tensor, and the explicit time dependent coupling can be replaced by a coupling due to an averaged interaction. Figure 17 shows the averaged line shape for an exact π-flip motion in its fast exchange limit, which is a superposition of two powder patterns whose effective quadrupolar coupling tensor is$[\bar{\delta}_Q, \bar{\eta}_Q]$, where $\bar{\delta}_Q$ is the averaged coupling constant that equals $\frac{5}{8}\delta_Q$ and the effective asymmetry parameter $\bar{\eta}_Q$ is 0.6. Note that due to a $\bar{\eta}_Q$value of 0.6, the line shape is not similar to the averaged line shape for fast methyl rotation, where the averaged tensor is axially symmetric ($\bar{\eta}_Q$=0). For the calculation of averaged tensors, readers are referred to the work of Spiess et al.[88]

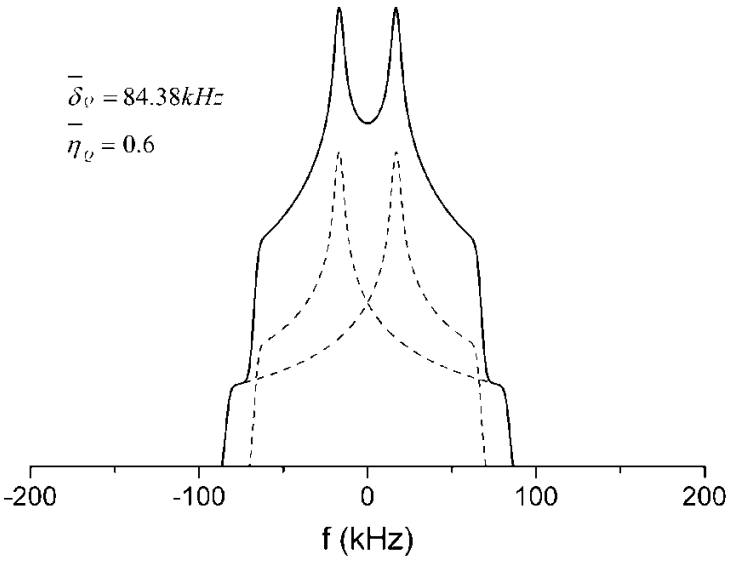

Figure 17. ^{2}H line shape of the exact π-flip motion in the fast exchange limit showing the averaged asymmetric tensor.

Echo Delay Dependent T_2 Anisotropy

The echo delay τ_1 between two 90° pulses in the quadrupolar echo pulse sequence is an important parameter in that it defines the time scale of signal refocusing. Figure 18 shows the line shape distortions due to anisotropic T_2 relaxation for an exact phenylene ring π-flip motion undergoing slow, intermediate, and fast motional rates. The figures clearly illustrate that at extremely slow and fast motion conditions the line shapes do not show T_2 distortion, and the relaxation is entirely controlled by the non-selective static dipolar interaction. In the intermediate exchange regime, both the line shape and the refocusing efficiency are strongly dependent on the echo delay. The refocusing efficiency drops quickly with increasing τ_1 in this regime.

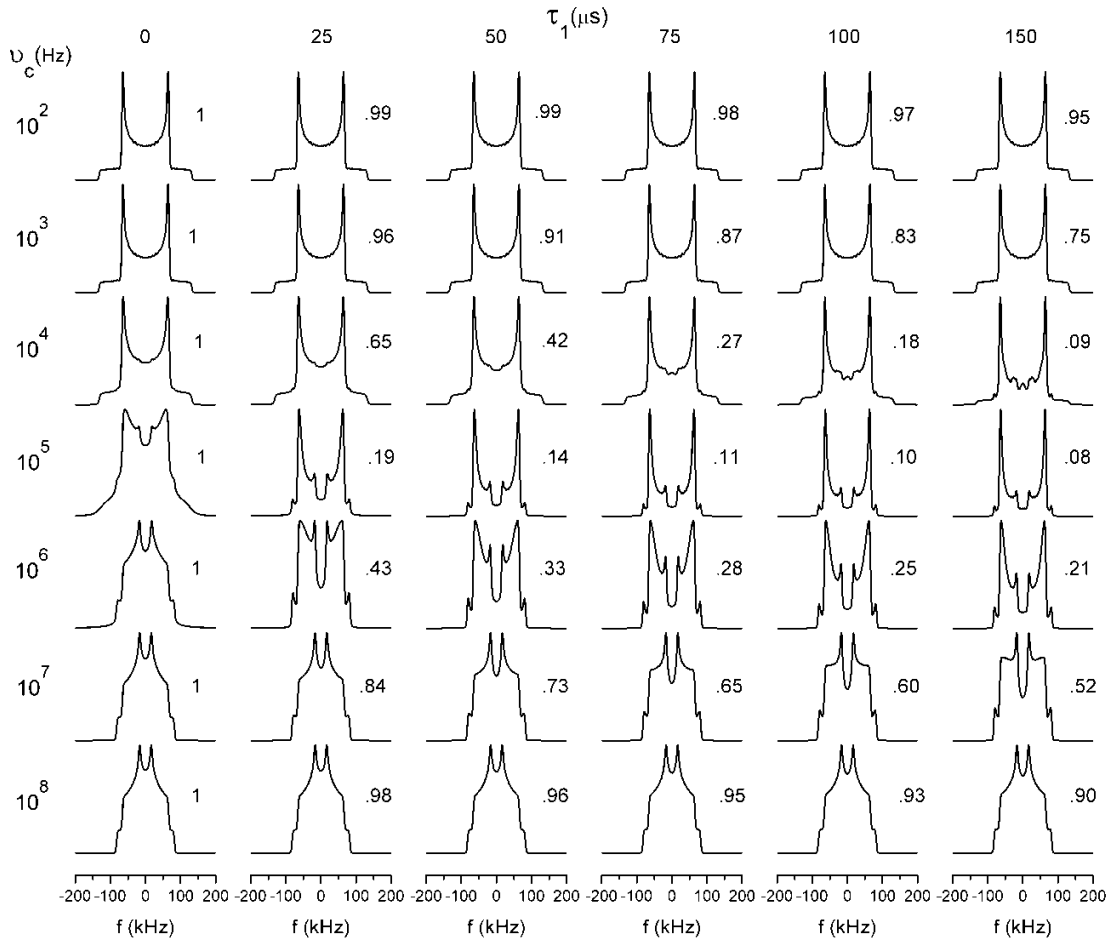

Figure 18. ^{2}H NMR calculated line shapes and refocusing efficiency factors for an exact π-flip model as a function of the motional rate (ν_c) and refocusing time (τ_1).

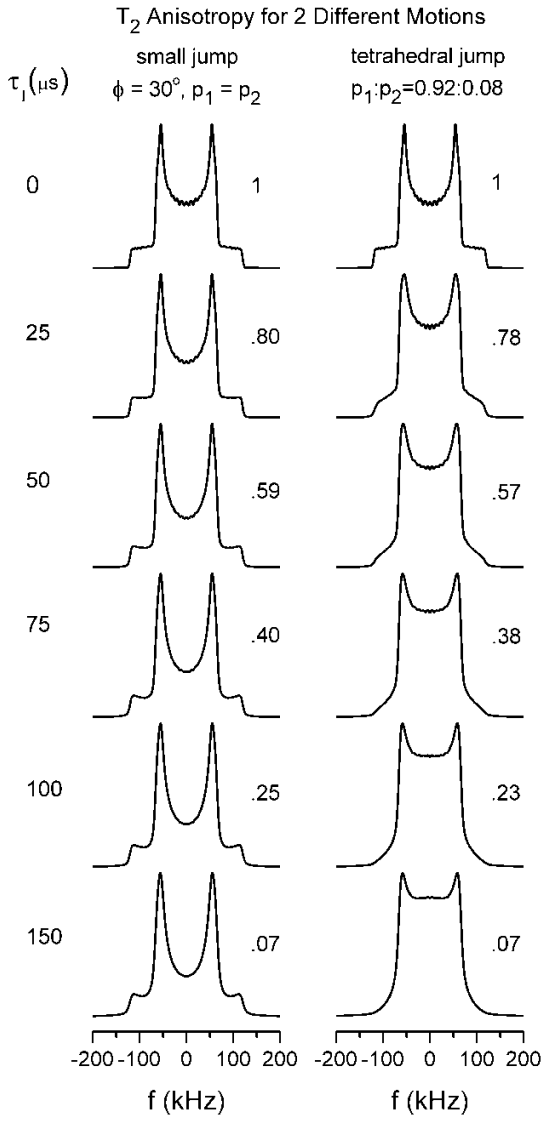

Figure 19. Echo distorted line shapes for two different jump motions ($\nu_c = 10^6$ Hz) about a tetrahedral axis. The line shapes in the left column are those calculated for an equal population jump over an angle of 30°. The line shapes in the right column are those calculated for a model of a tetrahedral jump where the populations of the two sites are in the ratio of 92/8. Numbers next to each line shape are the integrated reduction factors.

Different motional models can result in indistinguishable $\tau_1 = 0$ or small τ_1 spectra. If one predicts the types of motion based on single τ_1 line shapes, erroneous conclusions may be drawn. It is therefore necessary to obtain a series of echo distorted line shapes with varying τ_1 to unambiguously identify different motional models.[120]

Figure 19 shows the echo delay dependent line shapes of two fast restricted motions, a restricted small-angle two-site jump around a tetrahedral axis, and a two-site tetrahedral jump with uneven site populations. The $\tau_1 = 0$ line shapes for the two fast restricted motions are indistinguishable, whereas the T_2 echo distortions are vastly different even when the echo delay τ_1 is relatively short. The figure shows that when the motional rate is in the fast limit but smaller than 10^8 Hz, the relative echo distortions observed in the central region of the line shapes of a tetrahedral two-site jump with $p_1 >> p_2$ model are relatively smaller as compared to the line shapes of a small-angle jump model. Therefore, anisotropic T_2 relaxation significantly expands our ability to differentiate motional models of motion having fast motional rates.

Distributions of Motional Rates and Amplitudes

In heterogeneous systems such as glasses, where dynamics are complex and cannot be described by a single correlation time, an inhomogeneous distribution of correlation times is the simplest modification of the model to accurately depict its dynamics. As shown in Equation 9, the quadrupolar echo spectrum J is then a weighted superposition of a series of individual line shapes $j(k;k_c,\sigma)$ for well-defined motional rates k with the contribution of each individual line shape $P(k;k_c,\sigma)$ governed by a distribution function; common distribution functions include log-Gaussian distribution and stretched exponential function (also called the Kohlrausch-Williams-Watts (KWW) function).

$$J = \int_0^\infty j(k; k_c, \sigma) P(k; k_c, \sigma) \mathrm{d}(k) \qquad \text{Equation 9}$$

When only one trajectory of motion is present, the resultant line shape will show well-defined singularities, regardless of the width of motional rate distribution. However, when the experimental spectra do not shown evidence of well-defined singularities, the molecular motions must be described by an inhomogeneous distribution of motional amplitudes. The distribution can be introduced in the same way as the distribution of motional rates by simply calculating the population-weighted superposition of the line shapes according to a proper distribution function. The angular distribution broadens the "singularities" in the line shapes and increases the intensity in the central portion of the line shapes.

CHAPTER III

CONTRIBUTIONS OF BISPHENOL A PHENYLENE RING MOTIONS TO THERMOMECHANICAL PROPERTIES AND RELATION TO T_g

Introduction

Amorphous crosslinked epoxies of high glass transition temperatures (T_g) are widely used in the matrix chemistries of aerospace carbon fiber reinforced polymer composites (CFRP) because of their excellent physical properties, manufacturability, and low cost. However, the application of CFRP is limited by the performance of epoxy matrices, which are inherently brittle because of high crosslink densities. Therefore, toughened epoxies with high moduli and high T_g's are desired. Two model epoxy networks that exhibit substantial differences in their thermal, mechanical, and morphological properties due to structural isomerism have been studied.[72,73,89] The isomeric networks are crosslinked epoxies fully cured at 1:1 stoichiometric equivalents of diglycidyl ether of bisphenol A (DGEBA) with 3,3'-diaminodiphenylsulfone (33DDS) or 4,4'-diaminodiphenylsulfone (44DDS), denoted 33A and 44A, respectively. The 33A system has a higher modulus but a smaller compression yield strain, and exhibits a T_g 40 °C lower than that of the 44A material.[89] In addition, positron annihilation lifetime studies show that the 33A system has a smaller hole-size free volume.[73] These data suggest the 33A epoxy behaves like an anti-plasticized 44A system.

Glass transition and sub-T_g relaxations are important phenomena that affect the engineering properties of glassy polymers and thus their applications. For example, bisphenol A based polycarbonate (BPAPC) is well-known for its high ductility and low brittle-ductile transition temperature. The ductility is related to a pronounced sub-T_g

relaxation, often referred to as the γ relaxation.[90,91] The molecular origin of this process has been an active topic in the field of polymer physics. It is generally recognized that large amplitude motions of the phenylene rings, or the so-called ring π-flips, are the source or closely related to the cause of the γ relaxation.[69,92] Similar ring π-flip motions have been observed in poly(2-hydroxypropyl ether of bisphenol A) (PHR)[93,94,95], polyethersulfone (PES)[96,97,98,99], poly(*p*-phenyleneterephthalamide) (PPTA)[100,101,102], poly(ethylene terephthalate) (PET)[103,104], and other polymers with para-phenylene rings in the backbone[105,106,107].

The ring flip process has been intensively studied in solid-state NMR line shape analyses involving ^{13}C chemical shift anisotropy (CSA)[94,93,108], ^{13}C-^{1}H dipolar coupling (DC)[91,109], and ^{2}H quadrupolar coupling (QC)[100,101,102,110,111], as well as in solid-state NMR 2D exchange spectra[103,112,113]. In addition, this process has been more recently studied using time-of-flight and backscattering quasi-elastic neutron scattering experiments (QENS)[95,98,99]. The frequencies of the ring flip motions detected by these techniques coincide with the relaxation rates determined from dynamical mechanical analysis (DMA) and dielectric spectroscopy (DES). However, it has been argued that ring π-flipping by itself is not mechanically active, because the polymer chain after a ring flip is in a conformation equivalent to the one before the flip.[94,113,114] For example, despite the facile ring flipping that occurs in amorphous poly(phenylene sulfide) (PPS)[114], this polymer does not show significant secondary relaxations as observed in polymers with similar structures[97]. Spiess et al. suggested that the π-flip motion might be coupled to mechanically active motions and thus act as an indicator for the latter.[112] Indeed, mechanically active main chain fluctuations can be inferred from[103,112,113] the wiggling of

isopropylidene methyl groups in BPAPC[115,116], and have further been confirmed by Horii et al. in their CSA line shape analysis of the phenylene ring quaternary carbons.[94]

In this chapter, the results of an investigation involving the molecular motions of phenylene rings in the bisphenol A (BPA) unit and the DDS structures in 33A and 44A are presented. The molecular motions were studied using ^{2}H line shape analysis. The syntheses of ring deuterated monomers and the preparation of networks comprised of these monomers are presented in the following section. This work shows that the molecular motions, specifically, the ring π-flip motions and the main chain fluctuations, correlate to low temperature mechanical γ relaxations of the epoxy networks. Based on the analysis, a growing correlation length of molecular motion within the networks was found with increasing temperature. No comparable difference was observed in the glassy state dynamics of the BPA rings in the two systems. The anti-plasticization effect is attributed to the meta-substitution on the 33DDS diamine rings which suppresses large amplitude molecular motions and leads to more compact packing in 33A.

Experimental Section

Materials. Epichlorohydrin (≥ 99%), anhydrous sodium hydroxide pellets (NaOH, ≥ 98%), toluene (≥ 99%), 3,3'-diaminodiphenylsulfone (33DDS, 97%), and 4,4'-diaminodiphenylsulfone (44DDS, 97%) were purchased from Sigma Aldrich and used as received. The NaOH pellets were dissolved into deionized water to make a 40%wt. aqueous NaOH solution. Ring deuterated bisphenol A (BPA-d_8, 98%) was obtained from Cambridge Isotope Laboratories, Inc. and used as received.

Ring Deuterated DGEBA-d_8 Synthesis.[117] Ring-deuterated DGEBA (DGEBA-d_8), **1** was synthesized (Figure 20) by the reaction of bisphenol A-d_8 (BPA-d_8) and

epichlorohydrin (ECl) at a stoichiometric equivalent of approximately 10:1 ECl to phenol to minimize epoxy monomer chain extension reactions. In a typical reaction, a two-neck flask fitted with reflux condenser was charged with BPA-d_8 (3.50 g, 15.3 mmol) and ECl (28.2 g, 305 mmol) and heated to 120 °C under magnetic stirring. Aqueous 40 wt% sodium hydroxide (3.1 g, 31.0 mmol NaOH) was added and allowed to reflux for 4 hours. Excess ECl was removed under vacuum and the product was washed with toluene under stirring to precipitate the NaCl salt. The precipitate was filtered and washed again with toluene. Toluene was distilled from the filtrate to leave the reaction product DGEBA-d_8 which was dried overnight *in vacuo* at 50 °C. Yield: 90%; ^{13}C NMR (DMSO-d_6) δ ppm: 34.11, 47.81, 54.22, 65.68, 72.96, 116.88, 130.05, 144.94, 159.35.

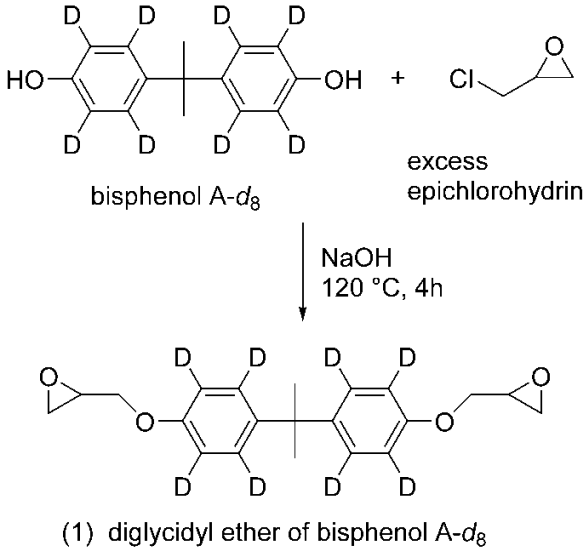

Figure 20. Synthesis of DGEBA-d_8.

Network Syntheses.[117] Deuterated glassy polymer network samples were prepared to comprehensively quantify solid-state ring motions of DGEBA epoxy cured with 33DDS and 44DDS. DGEBA-d_8 was cured with 33DDS and 44DDS into networks,

denoted 33A(BPA-d_8) and 44A(BPA-d_8) respectively, to study the effect of curative amine isomer positioning on ring motions of BPA units. Isomeric epoxy networks were prepared at a 1:1 stoichiometric equivalence of oxirane to active hydrogen. In a typical reaction, 200.0 mg of DGEBA-d_8 (MW = 236.29 g/mol; 0.85 mmol) was charged into a 1.0 mL dry glass vial and partially immersed to slightly above the monomer line into a preheated 100 °C silicone oil bath. After 15 min of equilibration, 105.1 mg of pulverized DDS (MW = 248.30 g/mol; 0.42 mmol) was carefully added over 10-15 min under slight agitation to facilitate dispersion and avoid agglomeration. Upon addition, the temperature was increased to 120 °C and the mixture was agitated until complete dissolution of amine was observed (typically 20 to 30 min) when vials were removed from the oil bath and transferred into a programmable curing oven. Curing prescriptions for all samples were 5 hours at 125 °C followed by 2 hours at 225 °C and subsequently cooled to room-temperature at the natural cooling rate of our oven. Glass vials were sacrificed and the amorphous polymer networks were carefully grounded into particles that fit into 5 mm high-precision NMR sample tubes. The molecular structures of the BPA-deuterated epoxy networks are shown in Figure 21.

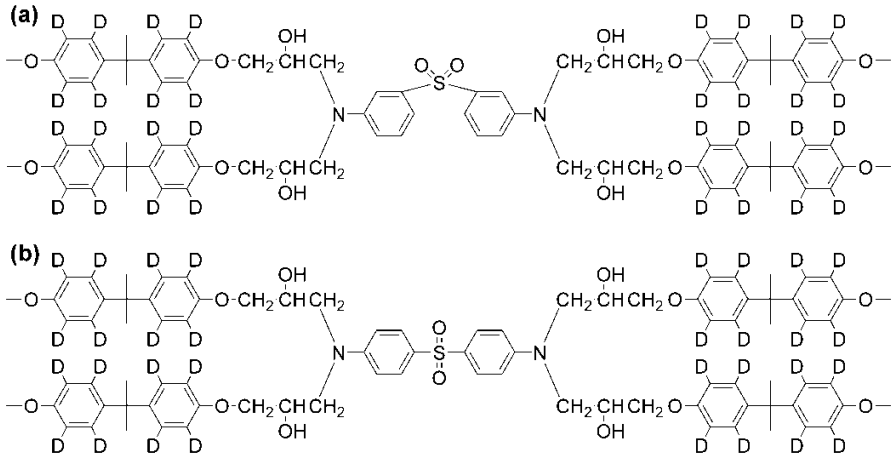

Figure 21. Structures of BPA deuterated epoxies: (a) 33A(BPA-d_8), and (b) 44A(BPA-d_8).

Thermal Characterization. The T_g's of non-deuterated 33A and 44A materials are 160-180 °C and 200-220 °C, respectively, depending on different cure prescriptions. The T_g's of 33A(BPA-d_8) and 44A(BPA-d_8) as determined by DSC are 134 and 168 °C, respectively. The deuterated networks thus have lower T_g's than their non-deuterated counterparts. However, 33A(BPA-d_8)'s T_g is 34 °C lower than that of 44A(BPA-d_8), the same trend as seen in non-deuterated ones. Thus, for comparison purposes it is worthwhile to examine the molecular dynamics within these deuterated networks. The validity of interpretations will be discussed.

Solid-state ^2H NMR Experiments. Solid-state ^2H NMR quadrupolar echo experiments were performed on a Varian ^{UNITY}INOVA NMR spectrometer equipped with a Tecmag wideline ^2H probe operating at 61.4 MHz (B_0 = 9.4 T). Fully relaxed quadrupolar echo spectra were acquired with a standard quadrupolar echo pulse sequence, 90_x-τ_1-90_y-τ_1-echo, with 90° pulse width of 2.5 µs and echo delay times τ_1 of 25, 50, 75, 100 and 150 µs. The spectral width was 2 MHz. The Free Induction Decay (FID) consisted of 2048 data points and was zero-filled to 4096 points. The FID was left-

shifted to the echo maximum, and Gaussian line broadening of 3 kHz was applied prior to application of the Fourier transform. No Lorentzian line broadening was used.

Variable temperature quadrupolar echo spectra were acquired between 0 °C to 200 °C. Temperatures were calibrated by placing a thermocouple beside the RF coil which was removed prior to data acquisition

Experimental Line Shapes

The ^{2}H quadrupolar echo line shapes for the network isomers measured at five echo delay times at different temperatures are shown in Figures 22 and 23.

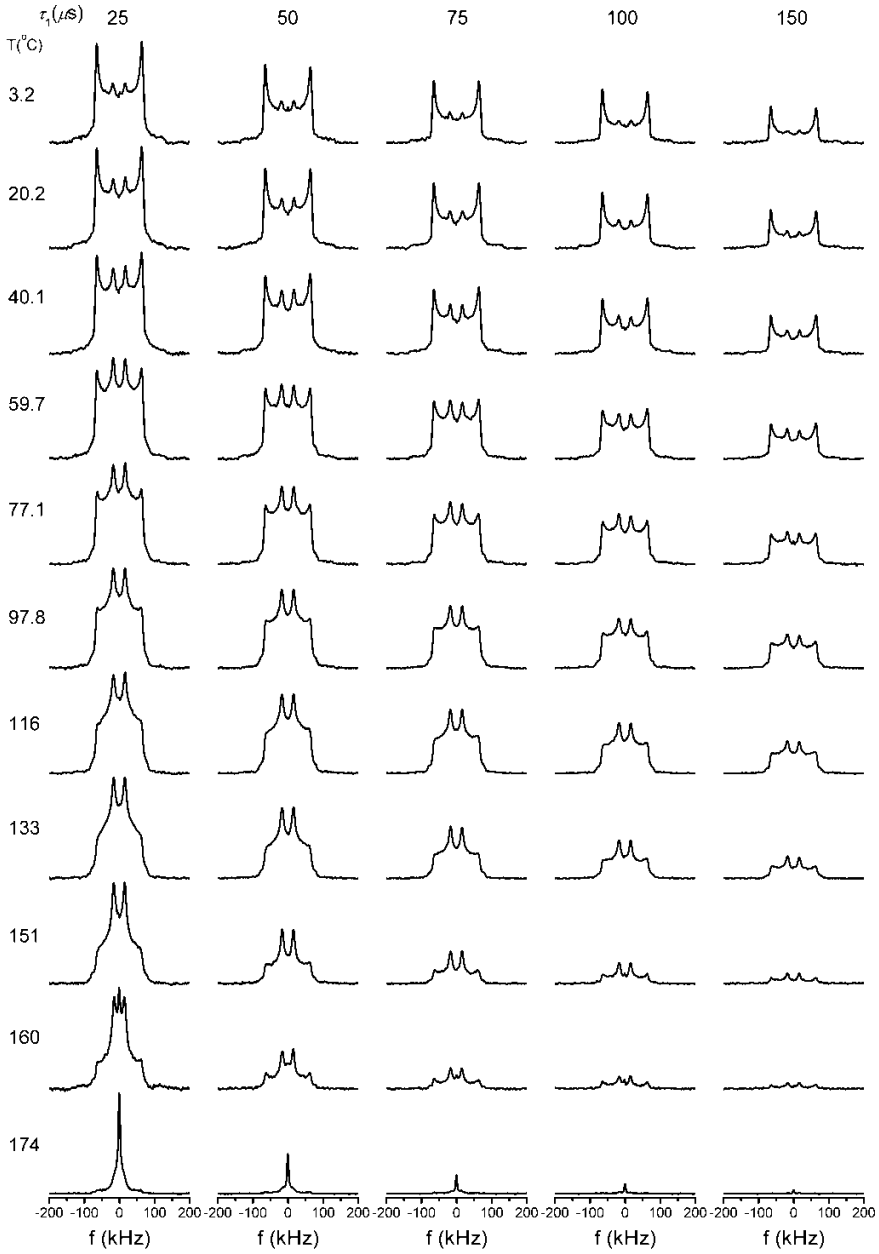

Figure 22. Experimental ^{2}H quadrupolar echo line shapes of 33A(BPA-d_8).

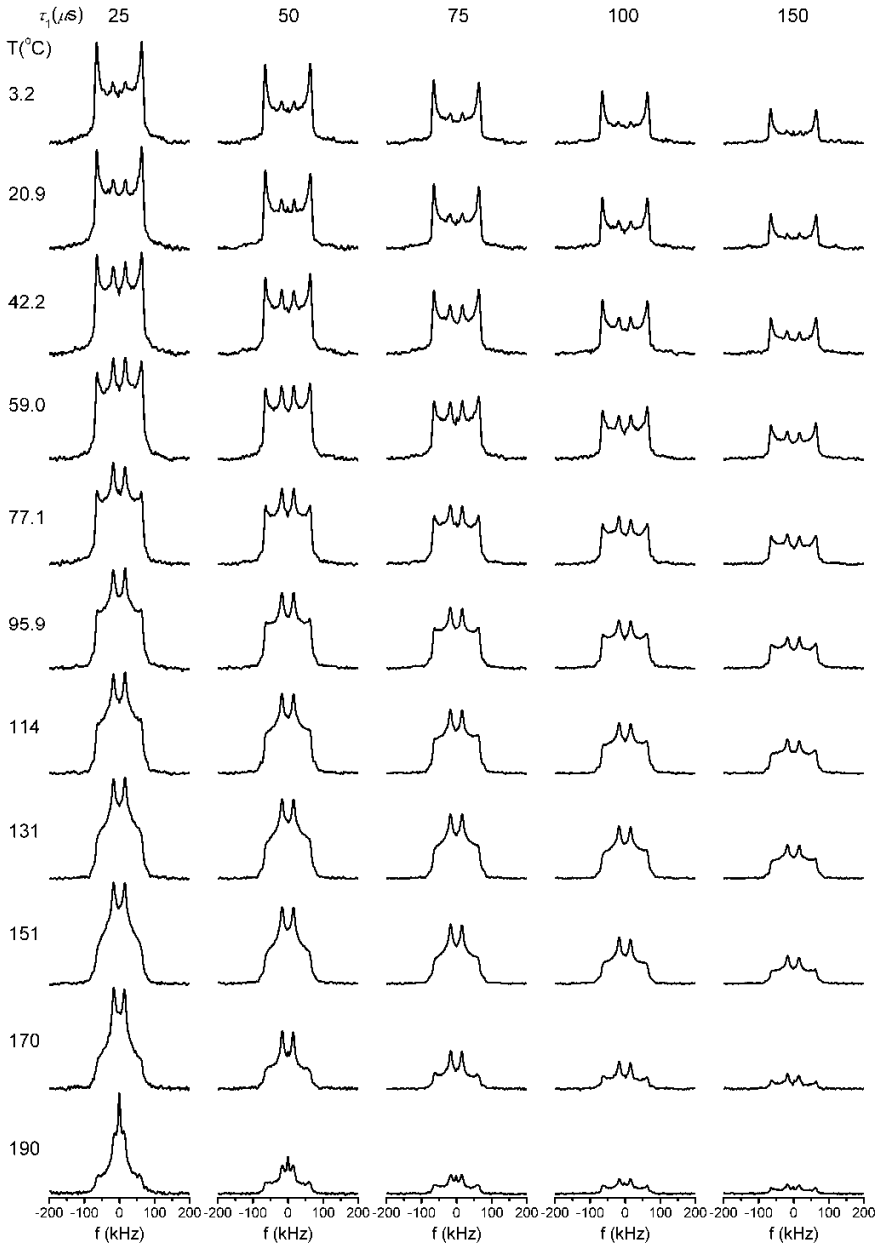

Figure 23. Experimental ^{2}H quadrupolar echo line shapes of 44A(BPA-d_8).

The general trends of the changes of line shape with echo delays and temperature can be described as follows:

1. As the temperature increases, the line shape due to rapid phenylene ring π-flips, characterized by the two inner singularities, becomes more dominant;

2. As the echo delay increases, the singularities characteristic of rapid ring flips decay faster than those of the relatively static rings;

3. At the highest experimental temperatures, molecular motions are such that a "liquid-like" isotropic peak is observed; here, the signal intensity is a strong function of echo delay, with very small magnetization observed at long echo delays (150 μs).

Figure 24 compares the ^{2}H line shapes of 33A(BPA-d_8) and 44A(BPA-d_8) as a function of echo delay and temperature. The spectra of the two are identical from 3 °C to 115 °C (Figure 24a-d). At temperatures above 115 °C, the line shapes exhibit increasingly significant spectral differences (Figure 24e-f). These will be examined in further detail in the Discussion section.

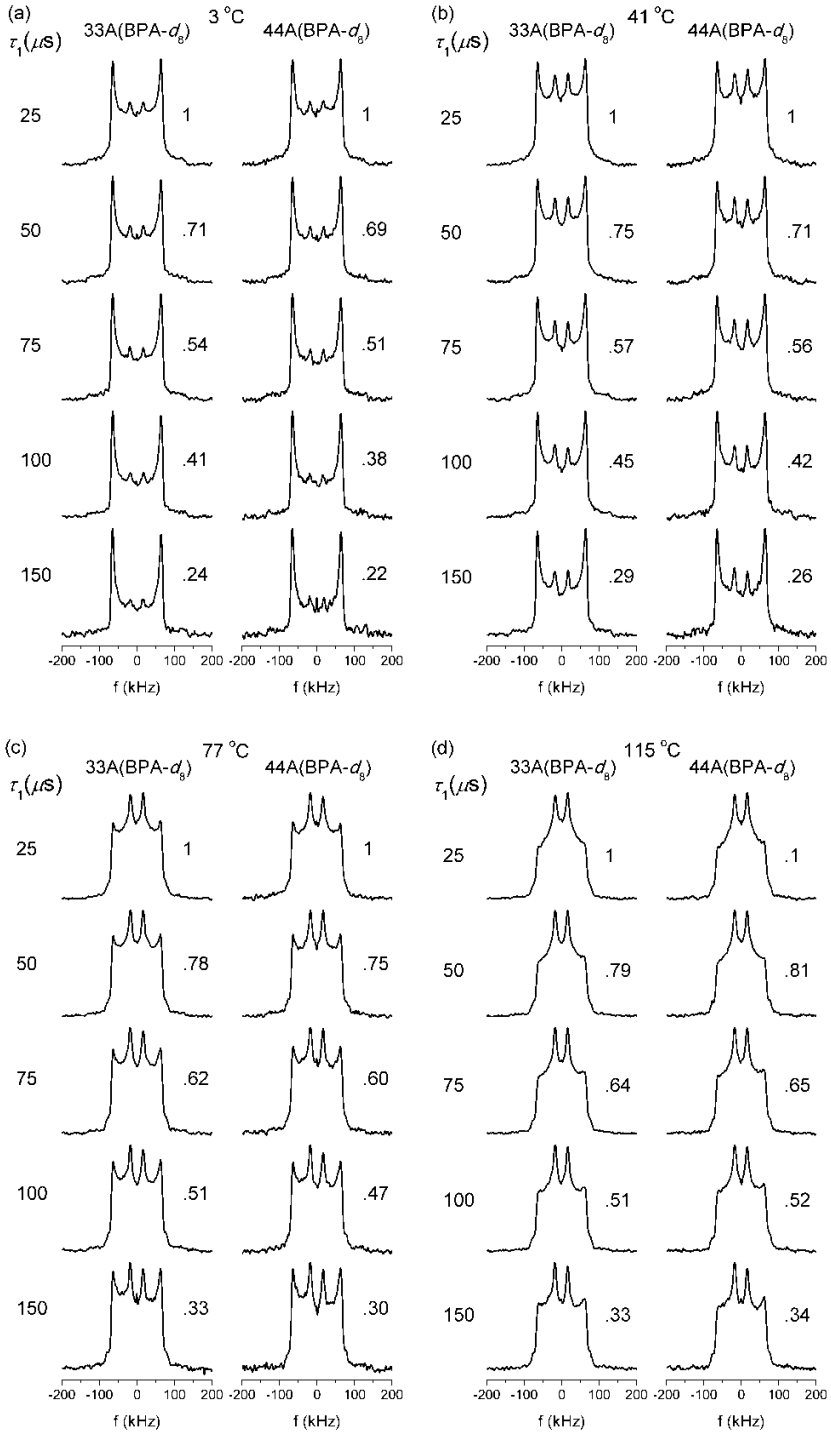
(a)
3 °C
33A(BPA-d_8)
44A(BPA-d_8)
$\tau_1(\mu s)$
25
50
75
100
150
1
.71
.54
.41
.24
1
.69
.51
.38
.22
(b)
41 °C
33A(BPA-d_8)
44A(BPA-d_8)
$\tau_1(\mu s)$
25
50
75
100
150
1
.75
.57
.45
.29
1
.71
.56
.42
.26
(c)
77 °C
33A(BPA-d_8)
44A(BPA-d_8)
$\tau_1(\mu s)$
25
50
75
100
150
1
.78
.62
.51
.33
1
.75
.60
.47
.30
(d)
115 °C
33A(BPA-d_8)
44A(BPA-d_8)
$\tau_1(\mu s)$
25
50
75
100
150
1
.79
.64
.51
.33
.1
.81
.65
.52
.34
-200 -100 0 100 200
f (kHz)

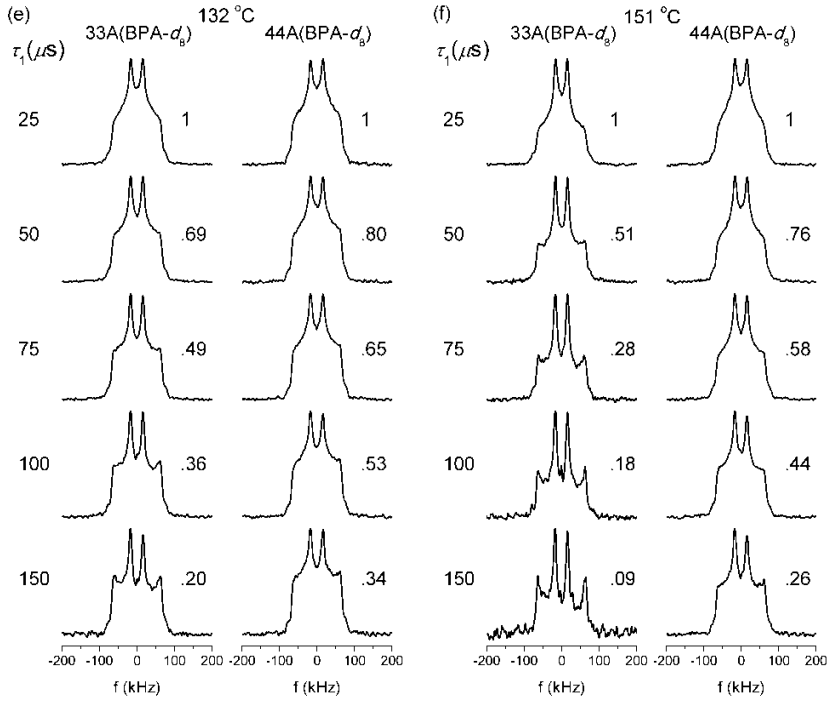

Figure 24. Comparison of the ^{2}H line shapes of 33A(BPA-d_8) and 44A(BPA-d_8) as a function of echo delay and temperature. The echo intensity normalized to the value at τ_1 = 25 μs is shown.

Line Shape Simulation

To determine the geometries, rates, and rate distributions of the phenylene ring motions, experimental spectra were compared to simulated line shapes obtained using EXPRESS (EXchange Program for RElaxing Spin Systems) software developed by Vold et al.[118,119] Simulated deuterium spectra need to match variations in experimental spectra as a result of changes in both temperature and echo delay.[120,121,122] Molecular motions in amorphous glasses are inherently heterogeneous, typically requiring distributions of motional rates and amplitudes in order to accurately describe their behavior.[121,123,124] Therefore, a simulated spectrum is actually a superposition of a series of individual line shapes characterized by single motional rates and amplitudes, and the contribution of

each individual line shape to the overall line shape is governed by a distribution function.[125]

Simulations using either a two-site π-flip model or a two-site π-flip model with additional fast libration could not accurately fit the experimental spectra given here. Especially problematic was properly duplicating the signal decay as a function of echo delay. The singularities due to fast ring flip motions did not decay with increasing τ_1 as rapidly as experimentally observed. The problem is illustrated in Figure 25.

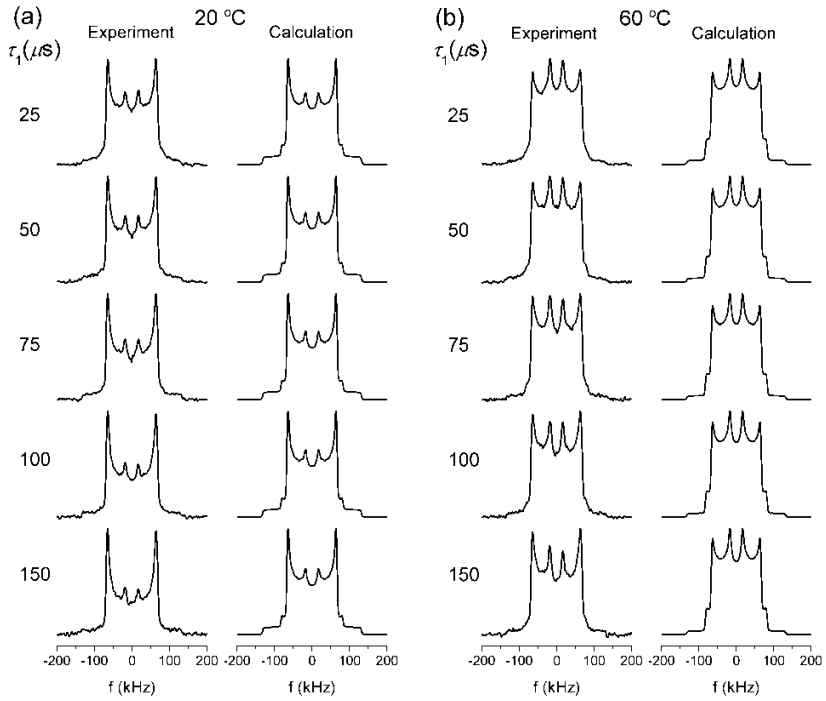

Figure 25. A two-site π-flip model cannot describe in precision the molecular motions of BPA phenylene rings. Note that the simulated 25 μs spectra match the experimental ones satisfactorily, but the inner singularities in the other simulated spectra do not decay as fast as those observed in experiments.

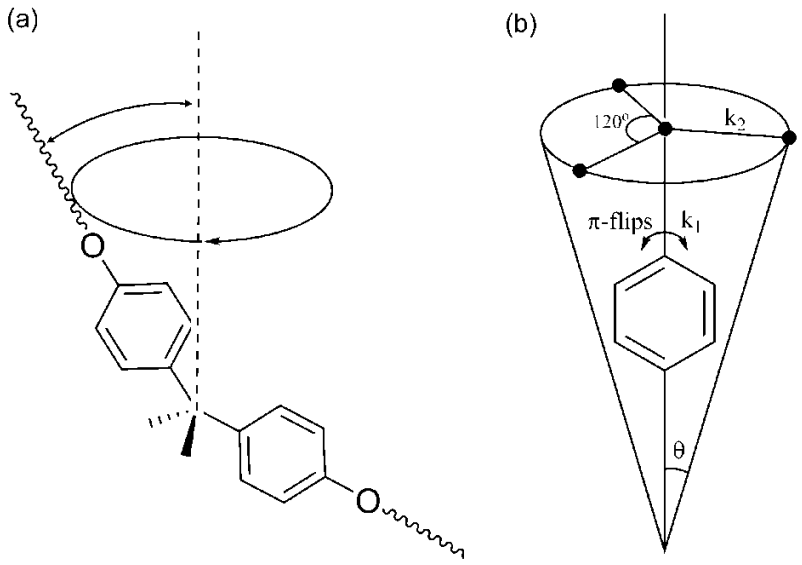

Figure 26. Model of phenylene ring motions. Adapted from reference with permission.[94]

In order to properly simulate the experimental data, ring motions are modeled as π-flips about the C_2 axis with accompanying fluctuation of the axis, illustrated in Figure 26. Here, the ring undergoes π-flips at a rate of k_1, and the fluctuation of the axis is described by a four-site exchange model, with an exchange rate of k_2 between any two of the four sites. The extent of fluctuation is quantified by the cone angle θ which describes the cone swept out by the fluctuation axis. As will be shown in the results, the fluctuation of the ring axis is of magnitude slower than the π-flip motion. This additional motional mode involving the fluctuation of the ring axis provides the mechanism required for rapid signal decay with echo delay at fast rates ($10^7 – 10^9$ s^{-1}). Figure 27 shows that the signal intensity decay behavior of this model differs from the simple π-flip model as the second motion plays a significantly more important role at high π-flip rates.

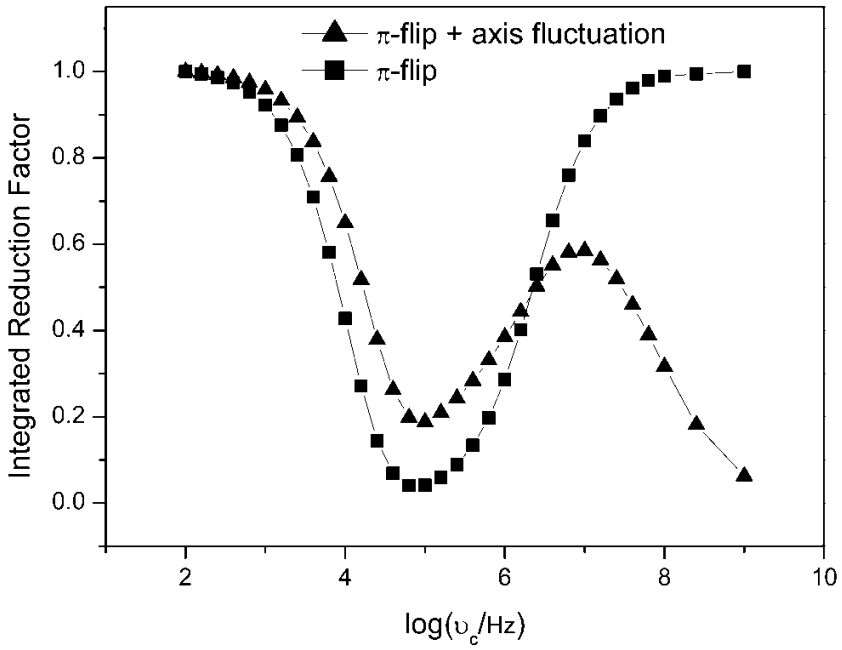

Figure 27. Comparison of the reduction factors of the π-flip and axis fluctuation model and the simple π-flip model as a function of π-flip rate.

Note that no flip angle distribution or fast libration was described by the model, although they have been proven to exist[95,108,126]; this simplification is applied in order to capture the major features of phenylene ring motions. A similar model was used to describe the change of the ^{13}C CSA line shape with temperature for poly(*2*-hydroxypropyl ether of bisphenol A) (PHR).[94] The dynamics of this model is well portrayed by the "open gate" description of ring flip motions by Horii et al.[94] and the molecular dynamics simulations by Yaris et al.[127] In this picture, the phenylene rings constantly undergo fast librations, and due to the kinetic energy fluctuation of the system the librational amplitude sometimes becomes large. The rings then propel neighboring chains. The neighboring chains as a result flex and make space for the propelling rings to flip.

The quadrupolar coupling constant was assumed to be 176 kHz for all simulations, and the asymmetry parameter was set to 0. Calculated FIDs were left-shifted to echo maximums, and Gaussian broadening of 5 kHz was applied prior to application of Fourier transform. Correction for finite pulse width effects was not attempted.[128] A trivariate normal distribution $\{\mu_{k_1}, \sigma_1; \mu_{k_2}, \sigma_2; \mu_\theta, \sigma_\theta\}$ of ring π-flip rate *log*(k_1), fluctuation rate *log*(k_2), and cone angle θ was employed.[129] This distribution and its relationship to the overall deuterium line shape *J* is expressed in Equation 10:

$$J = \int j(k_1, k_2, \theta) \cdot P(k_1, k_2, \theta) d(\theta) d(k_2) d(k_1) \qquad \text{Equation 10}$$

Here, $j(k_1,k_2,\theta)$ is the deuterium line shape resulting from phenylene ring undergoing a specific motion as described by the model, and $P(k_1,k_2,\theta)$ is the probability density of such rings in the system.[125] For the calculations of 3D line shape basis sets $j(k_1,k_2,\theta)$ and 3D probability density $P(k_1,k_2,\theta)$, one is referred to Appendixes A and B. Intuitively, some correlation between the ring flipping and the axis fluctuation motions is expected; in order to make calculations tenable, the three covariances $\{r_{(k_1,k_2)}, r_{(k_2,\theta)}, r_{(\theta,k_1)}\}$ that describe the correlations between the three variables are all set to 0.7. This empirical value for the covariances was adequate for properly simulating the experimental results. Coarse calculations showed that good simulations can be obtained using covariance values in the range of 0.7 ± 0.1. Better simulation fits may be possible if the three covariance values are allowed to vary independently; however, such calculations are too cumbersome and time consuming to be implemented at this time.

Simulation Results

The experimental versus calculated ^{2}H quadrupolar echo line shapes as a function of increasing quadrupolar echo delay and temperature for 33A(BPA-d_8) and 44A(BPA-d_8) are shown in Figures 28 and 29.

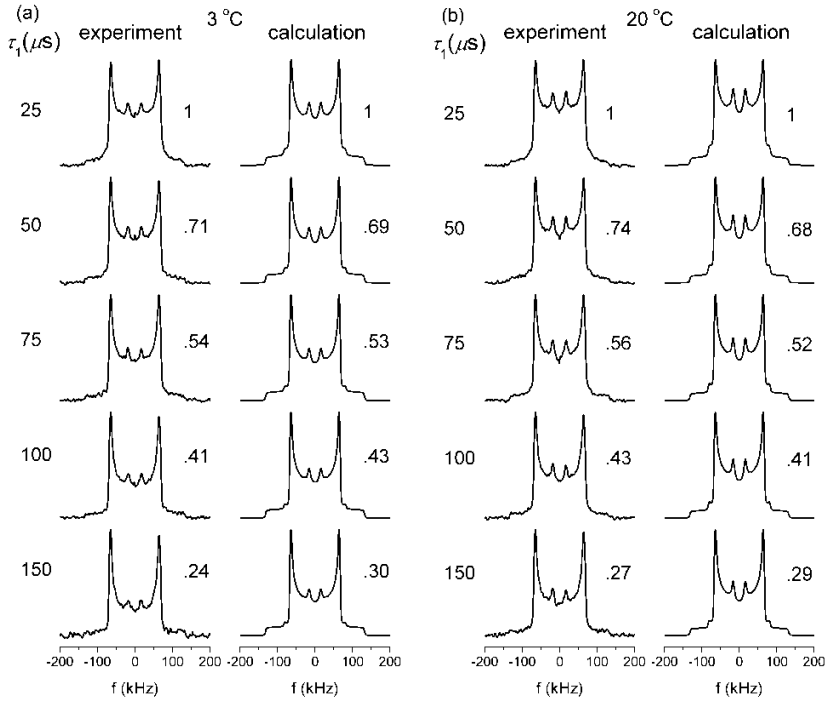

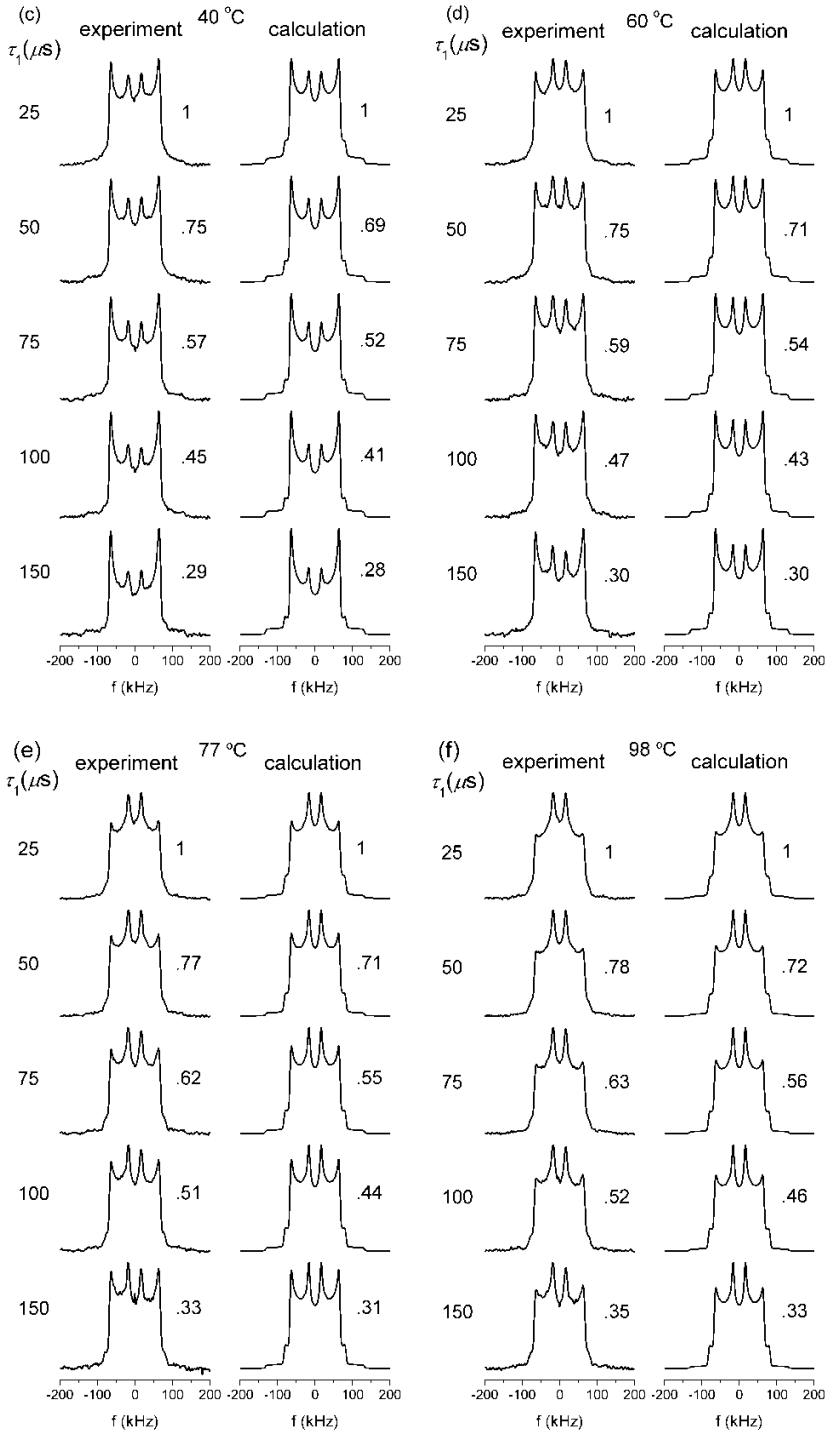
(c)
40 °C
experiment
calculation
$\tau_1(\mu s)$
25
50
75
100
150
1
.75
.57
.45
.29
1
.69
.52
.41
.28
-200 -100 0 100 200
f (kHz)
(d)
60 °C
experiment
calculation
$\tau_1(\mu s)$
25
50
75
100
150
1
.75
.59
.47
.30
1
.71
.54
.43
.30
-200 -100 0 100 200
f (kHz)
(e)
77 °C
experiment
calculation
$\tau_1(\mu s)$
25
50
75
100
150
1
.77
.62
.51
.33
1
.71
.55
.44
.31
-200 -100 0 100 200
f (kHz)
(f)
98 °C
experiment
calculation
$\tau_1(\mu s)$
25
50
75
100
150
1
.78
.63
.52
.35
1
.72
.56
.46
.33
-200 -100 0 100 200
f (kHz)

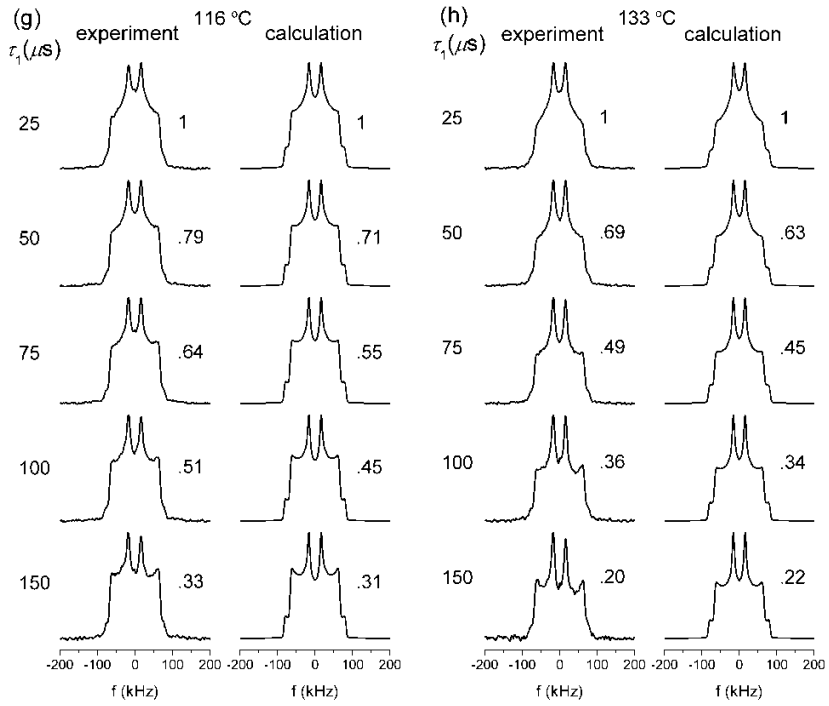

Figure 28. Experimental and calculated ^{2}H quadrupolar echo line shapes for 33A(BPA-d_8). The echo intensity normalized to the value at τ_1 = 25 µs is shown.

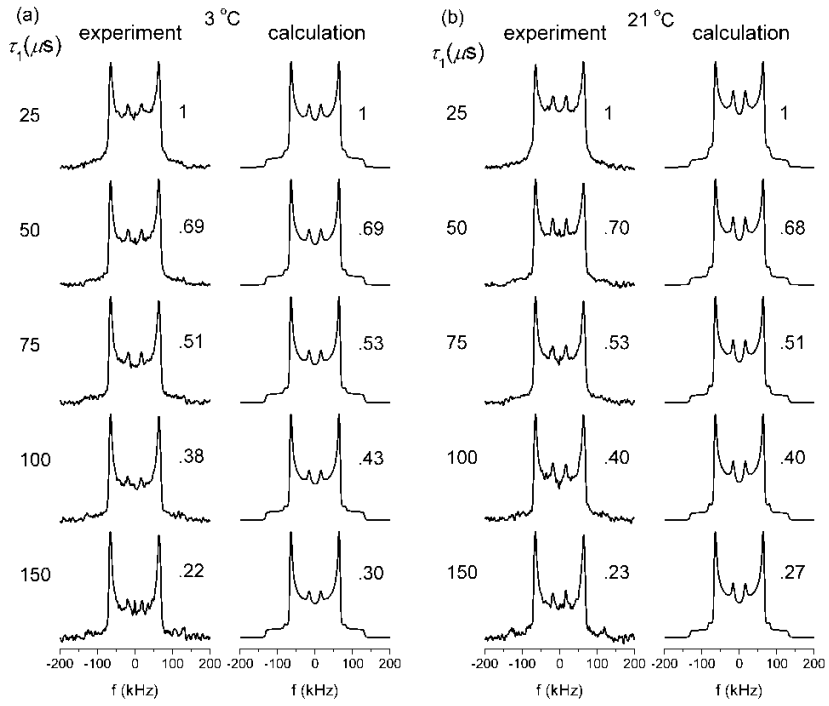

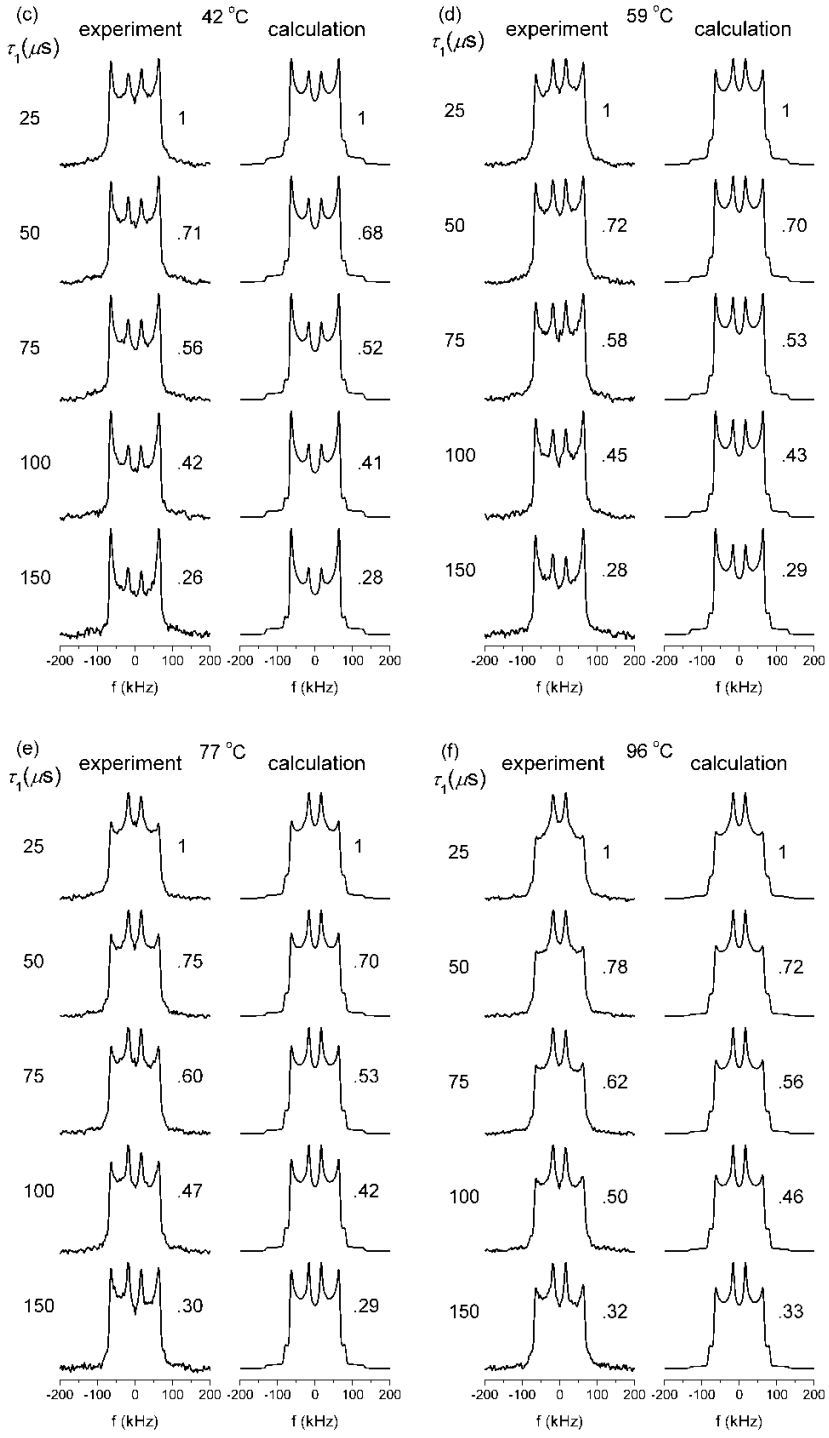
(c)
42 °C
experiment
calculation
$\tau_1(\mu s)$
25
50
75
100
150
1
.71
.56
.42
.26
1
.68
.52
.41
.28
-200 -100 0 100 200
f (kHz)
(d)
59 °C
experiment
calculation
$\tau_1(\mu s)$
25
50
75
100
150
1
.72
.58
.45
.28
1
.70
.53
.43
.29
-200 -100 0 100 200
f (kHz)
(e)
77 °C
experiment
calculation
$\tau_1(\mu s)$
25
50
75
100
150
1
.75
.60
.47
.30
1
.70
.53
.42
.29
-200 -100 0 100 200
f (kHz)
(f)
96 °C
experiment
calculation
$\tau_1(\mu s)$
25
50
75
100
150
1
.78
.62
.50
.32
1
.72
.56
.46
.33
-200 -100 0 100 200
f (kHz)

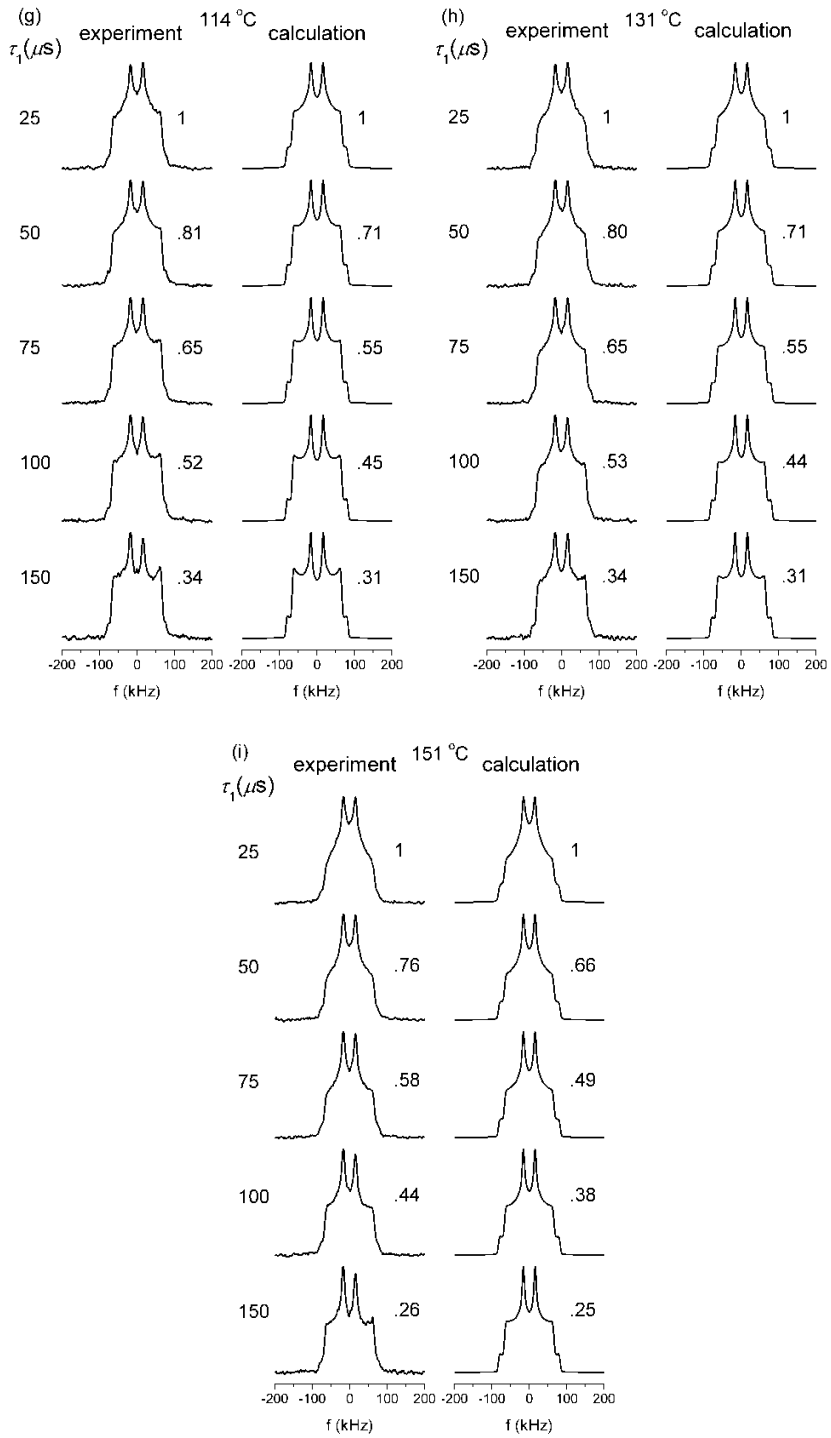

Figure 29. Experimental and calculated ^{2}H quadrupolar echo line shapes for 44A(BPA-d_8). The echo intensity normalized to the value at τ_1 = 25 µs is shown.

The simulation parameters are summarized in Tables 1 and 2; here, $\tau_{c,1}$ is the π-flip correlation time (inverse of mean π-flip rate k_1), $\tau_{c,2}$ is the correlation time of ring axis fluctuation ($4/k_2$), and θ is the cone angle of the fluctuation. The variances σ_1, σ_2, and σ_θ indicate the widths of the corresponding distributions. The effective T_2 value based on the integral area of the full line shape for each temperature is also included in the tables. The rate and cone angle distributions for 33A(BPA-d_8) at about 116 °C are graphically shown in Figure 30.

Table 1

Simulation parameters for 33A(BPA-d_8)

T (°C)	$\log(\tau_{c,1}/s)$	σ_1	$\log(\tau_{c,2}/s)$	σ_2	θ (°)	σ_θ (°)	T_2 (μs)
3.2	-3.5	2.2	-1.4	1.5	0	4	600
20	-4.0	2.2	-1.6	1.25	0	5	800
40	-4.4	2.3	-1.7	1	0	7	900
60	-4.8	3	-1.8	1	0	8	900
77	-5.4	3	-1.9	1	0	8	1200
98	-6.0	3	-1.9	1	0	8	1200
116	-6.6	2	-2.0	1	0	9	1500
133	-7.2	2	-2.6	1	0	15	1500

Table 2

Simulation parameters for 44A(BPA-d_8)

T (°C)	$\log(\tau_{c,1}/s)$	σ_1	$\log(\tau_{c,2}/s)$	σ_2	θ (°)	σ_θ (°)	T_2 (μs)
3.2	-3.5	2.2	-1.4	1.5	0	4	600
21	-4.0	2.2	-1.6	1.25	0	5	700
42	-4.4	2.3	-1.7	1	0	7	900
59	-4.8	3	-1.8	1	0	8	800
77	-5.4	3	-1.9	1	0	8	900
96	-6.0	3	-1.9	1	0	8	1200
114	-6.6	2	-2.0	1	0	9	1500
131	-7.2	2	-2.2	1	0	12	2000
151	-7.8	1.5	-2.6	1	0	15	2000

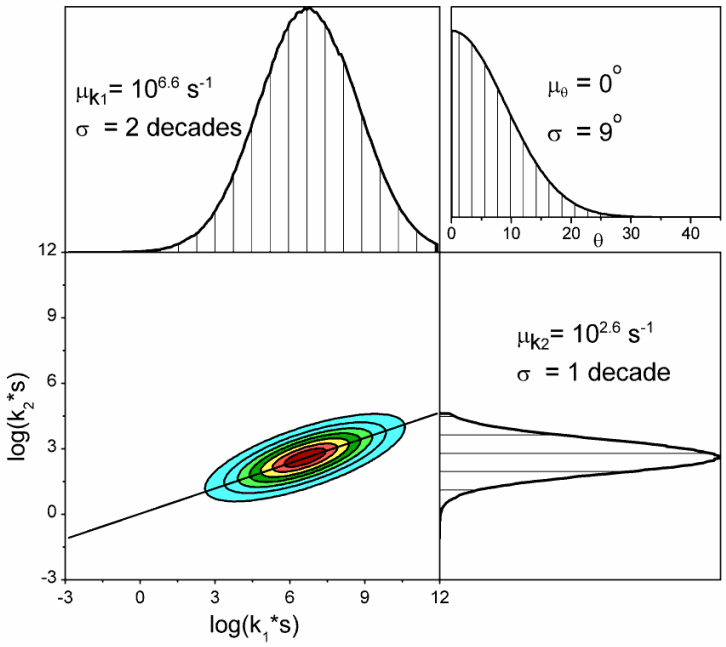

Figure 30. Plot showing the distributions of ring motional parameters in 33A(BPA-d_8) at 116 °C. The mean values and distribution widths of ring flip rate k_1, axis fluctuation rate k_2, and axis fluctuation cone angle θ are shown in the upper left, bottom right, and upper right figures, respectively. The bottom left figure shows the correlation between the distributions of k_1 and k_2.

Discussion

All of the three key parameters of ring motions, k_1, k_2, and θ, increase with increasing temperature. The average cone angle θ of main chain fluctuations determined here is about 5° at room temperature, which is smaller than the values for PHR (10-12°)[94] and for BPAPC (10-15°)[115,116]. This is due to the fact the chain packing in crosslinked epoxies is more compact than that in linear polymers. The fluctuation rate k_2 and cone angle θ undergo a large increase when temperature approaches T_g of the materials, as can be seen from 33A(BPA-d_8) (T_g = 134 °C) at 133 °C and 44A(BPA-d_8) (T_g = 168 °C) at 151 °C. It is interesting to compare the BPA ring motions of the two epoxies at around

132 °C. Although the line shapes of the two epoxies at this temperature can be fitted using the same ring flip motion parameters (k_1 and σ_1), different values of k_2 and θ are required to reflect the difference in T_g.

The BPA ring π-flip rates observed here between 0 °C and T_g are similar to those determined by Jones et al. for BPA rings in a crosslinked epoxy based on DGEBA cured with 4,4'-methylene dianiline (MDA).[111] The π-flip rate distributions for 33A and 44A systems are broader than the MDA cured system but correlate well with the distribution width determined by Horii et al. for PHR.[93] With a closer examination the temperature dependence of π-flip rates is found to go through a change of slope at about 67 °C for 33A(BPA-d_8) and 44A(BPA-d_8), as shown in Figure 31.

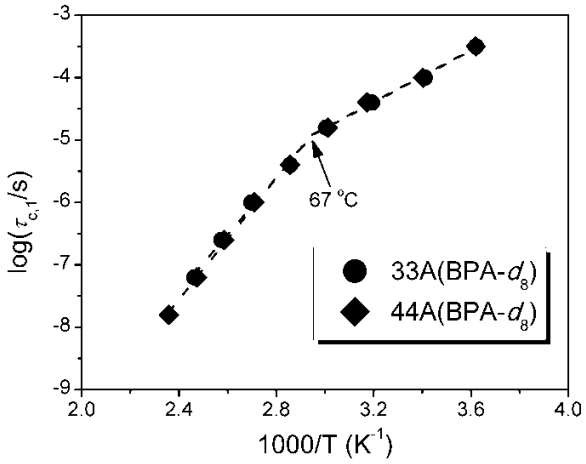

Figure 31. The Arrhenius plot: the temperature dependence of ring flip rates.

The Arrhenius Plot. The apparent activation energies for ring flip motions can be obtained from the slopes of the linear fittings in the Arrhenius plot (Figure 31). For BPA ring motions, a change of slope is observed at about 67 °C; the activation energies below and above this temperature were therefore calculated and denoted $E_{a,\gamma}$ and $E_{a,\beta}$,

respectively. The fittings were extrapolated to a 1 Hz time scale (the frequency of dynamic mechanical testing) in order to predict the temperature at which maximum mechanical loss induced by ring flips occurs. Calculated results are shown in Table 3. The activation energies $E_{a,\gamma}$ of BPA ring flip motions agree well with literature values (40-55 kJ/mol).[95,97,113]

Table 3

Activation energies and temperatures of 1 Hz phenylene ring π-flips

	$E_{a,\gamma}$ (kJ/mol)	$T(\tau_{c,1}=1s)$ (^oC)	$E_{a,\beta}$ (kJ/mol)	$T(\tau_\beta = 1s)$ (^oC)
33A(BPA-d_8)	40	-85.6	87.5	-25
44A(BPA-d_8)	40	-84.5	93.1	-20

Figure 32 shows the DMA tan δ curves of 33A and 44A in the sub-T_g temperature range. Both systems exhibit a broad γ relaxation spanning from below -100 °C to room temperature or higher. In addition, weak β relaxations are also observed at approximately 75 °C. Based on the extrapolated NMR ring flip rate data, the BPA ring motions contribute to the low temperature region (-85 °C, see Table 3) of the γ relaxation spectra of 33A and 44A. However, the exact temperature of this contribution is unclear due to the different T_g values between the deuterated and non-deuterated networks. Assuming a constant temperature shift in the Arrhenius plot due to deuteration, the NMR results indicate that the ring flip motions contribute to the -60 to -50 °C temperature range.

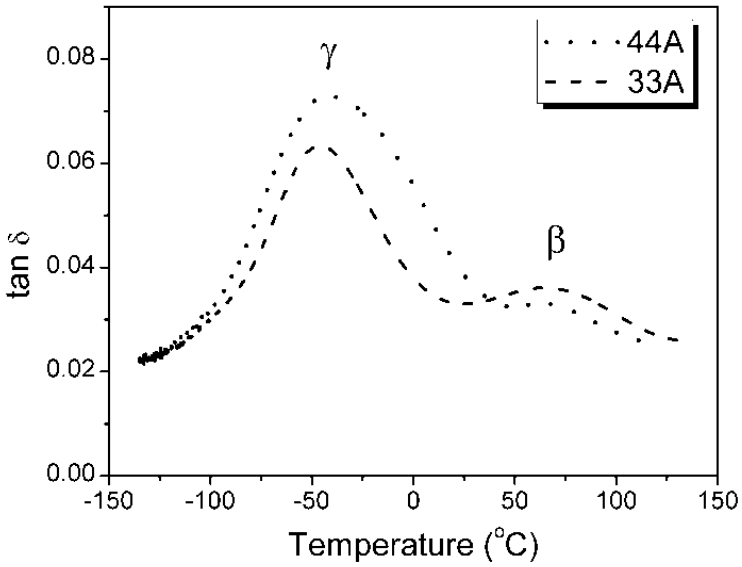

Figure 32. Dynamical mechanical tan δ spectra of 33A and 44A epoxies in the sub-T_g temperature range.

Chain Cooperativity. The slope change in the Arrhenius plot for BPA rings is very interesting. The activation energies become larger when the temperature gets higher than 67 °C. Although the inflection point might actually occur at a higher temperature due to the mismatch of the T_g values, it still falls within the envelope of the β relaxation peaks. According to current glass transition theories, an increase in the activation energy usually indicates an increased correlation length of molecular motion.[8,26,130] The observation of the inflection point in the Arrhenius plot suggests that the β relaxations of the epoxy networks could be due to motions of molecular chains of length scale longer than the BPA moiety. Specifically, the cooperative motion of the DGEBA unit may be the molecular origin of the β relaxations.

It gets interesting when one tries to relate the β relaxations to JG β relaxation. In fact, it is appealing to assign the β relaxations as the JG β relaxations of the epoxy networks because the β relaxations involve the entire DGEBA unit, one of the key

features of a genuine JG β relaxations. Moreover, if one calculates the activation energies for the JG processes of the two epoxies based on their glass transition temperatures using the empirical equation $E_{\mathrm{a}}^{\mathrm{JG}} = (24 \pm 3)RT_{\mathrm{g}}$ (Chapter I), one gets values of 88 kJ/mol and 94 kJ/mol for 33A and 44A systems, respectively. These values are strikingly close to the activation energies $E_{a,\beta}$ (87.5 kJ/mol and 93.1 kJ/mol) of the two networks (see Table 3).

Based on the method proposed by Starkweather for the activation energy of a secondary process, the cooperativities of the β and γ processes can be calculated. The positions of the activation energies in the E_a-T map are shown in Figure 33. The figure clearly indicates that the γ processes are simple local processes that do not generate much configurational entropy, while the β processes are more cooperative as they involve the rearrangement of short range DGEBA molecular segments. The cooperativities of the β processes are calculated to be 33% and 36% for 33A and 44A, respectively. The numbers signify that the motion of DGEBA segment in 44A is more cooperative than that in 33A.

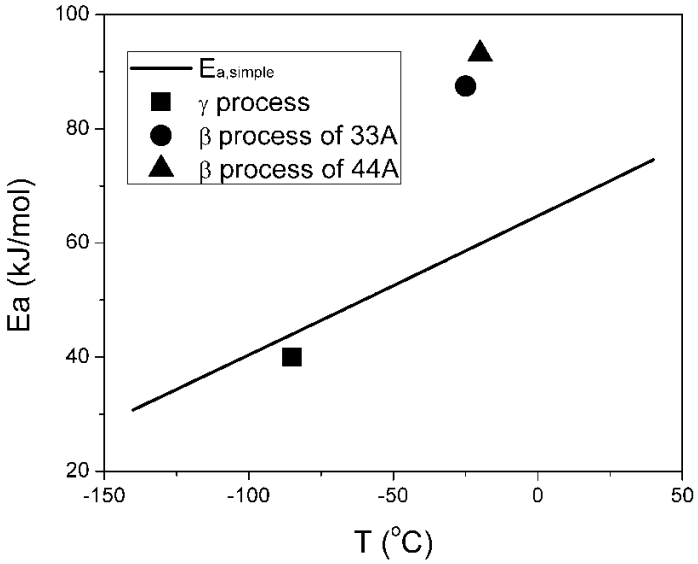

Figure 33. The Starkweather plot showing the activation energies for the γ and β processes that involve the BPA phenylene ring motions.

The observation that the BPA rings at temperatures up to 115 °C (20 °C below the T_g of 33A(BPA-d_8)) exhibit the same motional behaviors in both systems suggests that the local environment of the BPA rings is similar for the isomers at such temperatures. The diamine crosslinkers therefore do not significantly affect the BPA ring dynamics, indicating that the molecular motions of BPA rings are localized in the glassy state. It is not until the temperature gets above T_g(33A) - 20 °C that the DDS amines begin to influence the BPA ring dynamics: in the case for 44DDS, rapid π-flips and backbone fluctuation of the para-phenylene rings promote cooperative motions with DGEBA segments to effectively dissipate energy; whereas for 33DDS no such energy dissipation mechanism is possible, resulting in a dramatic increase in main chain fluctuations at temperatures much lower than its 44DDS analogue.

Mechanical Relaxation Mechanism. The line shape analysis provided abundant detailed information about the motions of phenylene ring in crosslinked epoxies. To the

best of our knowledge, this is the first work that systematically incorporates main chain fluctuations into ^{2}H NMR line shape simulations. In contrast with Horii's work[94] which implied that the phenylene ring flip motion and the main chain fluctuation are concerted motions of the same frequency, this work demonstrates that the main chain fluctuation is two to four orders of magnitude slower than the ring flips, that is, hundreds to thousands of ring flips happen during one cycle of polymer backbone fluctuation.

There have been debates in literature on whether π-flip motions are mechanically active, as stated in the Introduction. Therefore, the temperature dependence of the main chain fluctuation rates was also studied here. It should be noted that in order to reduce the time required for calculations, the chain fluctuation rate values were determined using larger step values. Extrapolations to a 1 Hz time scale indicate that the contributions of the main chain fluctuations to the mechanical relaxation fall within temperature ranges similar to those of the π-flip motions do. However, the activation energies of these main chain fluctuations are approximately 10-20 kJ/mol, much smaller than the 40-55 kJ/mol values for γ relaxation observed in DMA or dielectric studies. Therefore, the question of whether ring flip motions or main chain fluctuations are the true molecular origin of mechanical relaxation remains[131]: Could the ring flip motion and the main chain fluctuation both contribute to mechanical relaxation? Or is the main chain fluctuation only the molecular rearrangements to accommodate the ring flip motion? Or is the ring flip motion a molecular event that accompanies the main chain fluctuation? The authors tend to agree with the image drawn by Horii and Yaris that the two molecular events are mutually dependent: fast ring librations propel neighbor chains and the chain flexing

enables infrequent ring flipping. To reach a final conclusion, a systematic study in a multi-technique approach is needed.[132]

Conclusions

Isomeric epoxy networks 33A and 44A exhibit substantial differences in thermal, mechanical, and morphological properties, with the 33A epoxy behaving like an anti-plasticized 44A system. Networks synthesized with deuterated BPA rings were used to investigate the differences in ring motions along with their role in the mechanical relaxation. The molecular motions were studied using ^{2}H quadrupolar echo line shape analysis where experimental spectra were compared to simulated line shapes calculated using a model that describes both ring π-flips and ring axis fluctuations.

The BPA ring motions which contribute to the low temperature regions of the mechanical γ relaxations in both 33A and 44A have almost identical behaviors up to a temperature 20 °C below the T_g of 33A, suggesting minimal influence of the crosslinkers on the BPA ring dynamics, which further indicates that the BPA ring motions are localized, and the correlation length of the motions is not longer than the DGEBA unit at these temperatures. The BPA ring motions of both epoxies exhibit an increase in activation energy at a temperature coinciding with the β relaxations of the two networks. This suggests the β relaxations are possibly related to the cooperative motion of the entire DGEBA unit, whereas below the β transition the ring motions have a correlation length equal to the BPA moiety. From the study of BPA ring motions, a picture of gradual development of molecular motions is seen, starting with localized motions that involve only the BPA unit, transitioning to a cooperative motion that has a correlation length scale of a DGEBA unit, and ultimately becoming long range cooperative motions

characteristic of the glass transition. The 40 °C difference in the T_g's of the networks is attributed to the additional energy dissipation mechanism by the 44DDS ring motions.

The study also found that the main chain fluctuation is a possible source of mechanical relaxation, consolidating previous speculations. However, the activation energy of this motional process is very small. Whether ring flip motion or main chain fluctuation is the true molecular origin of mechanical γ relaxation remains a question.

CHAPTER IV

EFFECT OF SUB-T_g MOTIONS IN DIAMINE STRUCTURES ON THE THERMOMECHANICAL PROPERTIES OF ISOMERIC EPOXY NETWORKS

Introduction

In Chapter III, the molecular motions of phenylene rings in the bisphenol A (BPA) structure of two isomeric epoxy networks, 33A and 44A, were studied using ^{2}H NMR line shape analysis. The two epoxy networks were of interest because they show interesting differences in their mechanical, thermal and morphological properties simply due to isomeric substitution on their diamine phenylene rings. It is found that the 33A network has a glass transition temperature (T_g) 40 °C lower than that of the 44A and exhibits mechanical properties of an anti-plasticized 44A system. However, the study of BPA ring motions found little difference in the dynamics of BPA rings in the sub-T_g temperature range, but only suggested a growing correlation length of motion with increasing temperature. Therefore, the differences in the properties of the isomeric networks likely result completely from the different dynamics of the diamine crosslinkers.

In this chapter, the phenylene ring motions in the diamine structure of 33A and 44A were studied through ^{2}H NMR line shapes analysis to further understand the role of these motions in the sub-T_g transitions and to explain at a molecular level the anti-plasticization effect seen in the 33A network. The syntheses of ring deuterated isomeric diamines and the preparation of epoxy networks comprised of these monomers are presented in the following section. The study suggested that the anti-plasticization effect was attributed to the meta-substitution on the diamine phenylene rings which suppresses large amplitude motions and leads to more compact packing in the 33A epoxy.

Experimental Section

Materials. Acetic anhydride (≥ 98%), carbon disulfide (≥ 99%), sulfonyl chloride (≥ 98%), aluminum trichloride (≥ 98%), glacial acetic acid, ammonium chloride (≥ 99%), tetrahydrofuran (THF, ≥ 99%), hydrogen peroxide (≥ 98%), hydrochloric acid (HCl, ≥ 98%), decolorizing carbon, methanol (≥ 99%), potassium nitrate (KNO_3, ≥ 98%), sulfuric acid (H_2SO_4, ≥ 98%), chlorosulfonic acid (≥ 99%), chloroform (≥ 99%), methylene chloride (≥ 98%), dimethyl formamide (DMF, ≥ 99%), and palladium-carbon catalyst were purchased from Sigma Aldrich and used as received. Diglycidyl ether of bisphenol A (DGEBA, MW = 350-360 g/mol) was purchased from Momentive. Ring deuterated aniline (aniline-d_5, 98%), and deuterated benzene (benzene-d_6, 99.5%) were obtained from Cambridge Isotope Laboratories, Inc. and used as received. Hydrogen gas was purchased from Nordan Smith and used as received.

Ring Deuterated 44DDS-d_8 synthesis.[117] Ring deuterated 44DDS (44DDS-d_8) was synthesized as follows (Figure 34). Ring deuterated aniline (aniline-d_5) (2.0 g, 21.6 mmol) was added to 20 ml acetic anhydride and refluxed for 30 min. After cooling to room temperature, 25 ml water was added and heated at reflux for 10 min. The solution was cooled to room temperature and diluted with water to precipitate the product, *N*-acetylaniline-d_5, **1**, which was filtered, washed with water, recrystallized from water, and dried. Yield: 89%; m.p.: 115 °C; IR (KBr) cm^{-1}: 3301, 3174, 3092, 1666; ^{13}C NMR (DMSO-d_6) δ ppm: 24.62, 119.61, 123.63, 129.31, 140.01, 168.92.

N-acetylaniline-d_5, **1** (8.26 g, 61.18 mmol) was suspended in 80 ml carbon disulfide, and aluminum trichloride (15.40 g, 123.6 mmol) and thionyl chloride (3.36 g, 28.28 mmol) were added. After the initial reaction subsided, the mixture was heated at

reflux for 6 hours, cooled to room temperature, and quenched by the addition of a 10% ammonium chloride solution in water. The mixture was filtered, and the solid was washed with water, dissolved in THF, filtered, and the filtrate concentrated under vacuum. The product, 4,4'-di-*N*-acetylaminodiphenyl sulfoxide-d_8, **2** was recrystallized with MeOH/H_2O. Yield: 91%; m.p.: 291 °C; IR (KBr) cm^{-1}: 3306, 3252, 3159, 3082, 1673; ^{13}C NMR (DMSO-d_6) δ ppm: 24.21, 119.31, 125.01, 139.11, 141.62, 168.71.

4,4'-di-*N*-acetylaminodiphenyl sulfoxide-d_8, **2** (8.0 g, 25.4 mmol) was suspended in 100 ml glacial acetic acid; subsequently, 30% H_2O_2 (10 ml) was added dropwise to the suspension, and the mixture was allowed to stand for 3 hours at room temperature. The mixture was then heated to 50 °C for 2 hours and subsequently refluxed until homogenous. The homogenous mixture was cooled to room temperature. Next, 5 ml 30% H_2O_2 was added, and the mixture was stored overnight at 4 °C. The mixture was concentrated *in-vacuo* and recrystallized from MeOH/H_2O to yield 4,4'-di-*N*-acetylaminodiphenyl sulfone-d_8, **3**. Yield: 89%; m.p.: 282 °C; IR (KBr) cm^{-1} : 3335, 3250, 3100, 1682; ^{13}C NMR (DMSO-d_6) δ ppm: 22.41, 117.13, 126.62, 133.32, 141.82, 167.34.

4,4'-di-*N*-acetylaminodiphenyl sulfone-d_8, **3** (6.0 g, 18 mmol) was suspended in 60 ml 10% HCl, and heated at reflux for 1.5 hours. Activated carbon was added to decolorize, and the mixture was refluxed for 1 hour, filtered while hot, and cooled to room temperature. A 10% NaOH solution was added to adjust the pH to 14, and the resulting precipitate was isolated by filtration, recrystallized with MeOH/H_2O, and dried in a vacuum oven to yield 0.5 g of the final product 44DDS-d_8, **4**. Yield: 10%; m.p.: 198

°C; IR (KBr) cm^{-1}: 3480, 3300, 3275; ^{13}C NMR (DMSO-d_6) δ ppm: 113.52, 128.82, 129.23, 153.44.

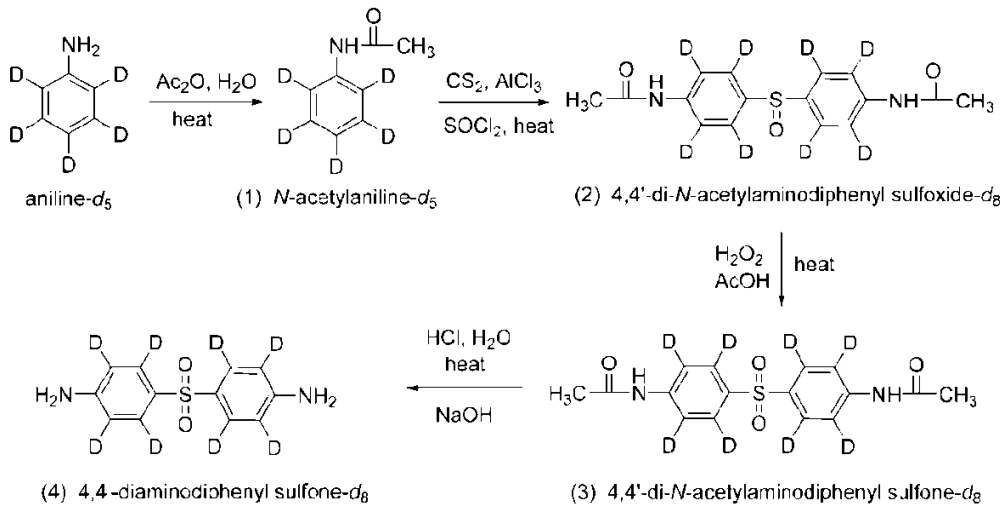

Figure 34. Synthesis of 44DDS-d_8.

Ring Deuterated 33DDS-d_8 Synthesis.[117] Ring deuterated 33DDS (33DDS-d_8), **4** was synthesized as follows (Figure 35). The preparation of 100% nitric acid by the reaction of sulfuric acid with potassium nitrate was necessary for use in the synthetic procedure. Vacuum distillation was used to collect the nitric acid. The first step in the synthesis for 33DDS-d_8, **4**, was the dropwise addition of chlorosulfonic acid (11.65 g, 0.1 mol) to benzene-d_6 (16.82 g, 0.2 mol). The reaction mixture was kept at 20 °C and allowed to stir for 30 min. The reaction mixture was decanted onto ice and extracted with chloroform. Chloroform was distilled from the reaction mixture *in-vacuo* when the residue was filtered to leave a filtrate composed of a colorless liquid (benzenesulfonyl chloride-d_5, **1**) and a white filter cake product of diphenyl sulfone-d_{10}, **2**. Yield: 75%; m.p.: 128 °C. ^{13}C NMR (DMSO-d_6) δ ppm: 128.01, 129.98, 134.11, 141.91.

Diphenyl sulfone-d_{10}, **2** (10.96 g, 0.048 mol) was suspended in 30 ml of methylene chloride and dissolved with the aforementioned 100 wt% nitric acid (7.55 g, 0.117 mol). 14.8 g of 96 wt% sulfuric acid was then added dropwise under reflux with stirring over 4 hours at the boiling temperature of the solution (50 °C). Upon cooling to 20 °C the reaction product, 3,3'-dinitrodiphenyl sulfone-d_8, precipitated out of solution and was filtered off, washed twice with 100 ml of methylene chloride, once with water and dried at 100 °C. 3,3'-dinitrodiphenyl sulfone-d_8, **3** was purified by recrystallizing from DMF. Yield: 98%; m.p.: 203 °C. ^{13}C NMR (DMSO-d_6) δ ppm: 124.21, 131.89, 134.26, 136.12, 146.19, 152.17.

DMF was added dropwise to the 3,3'-dinitrodiphenyl sulfone-d_8, **3** (14.88 g, 0.047 mol) until fully dissolved, and 10 wt% palladium catalyst on wet carbon powder (0.74 g) was added. This mixture was placed into the hydrogenation flask of a Parr hydrogenation reactor to reduce the nitro groups to amines. Hydrogenation was carried out under a pressure of 3.5 atm H_2 at ambient temperature to completion. The catalyst was filtered off, and the filtrate was placed *in-vacuo* at 80 °C to remove solvent. The final product, 33DDS-d_8, **4**, was a yellow solid which was purified by recrystallization from MeOH and charcoal; m.p.: 174 °C. ^{13}C NMR (DMSO-d_6) δ ppm: 123.87, 131.91, 134.13, 135.89, 146.01, 151.46.

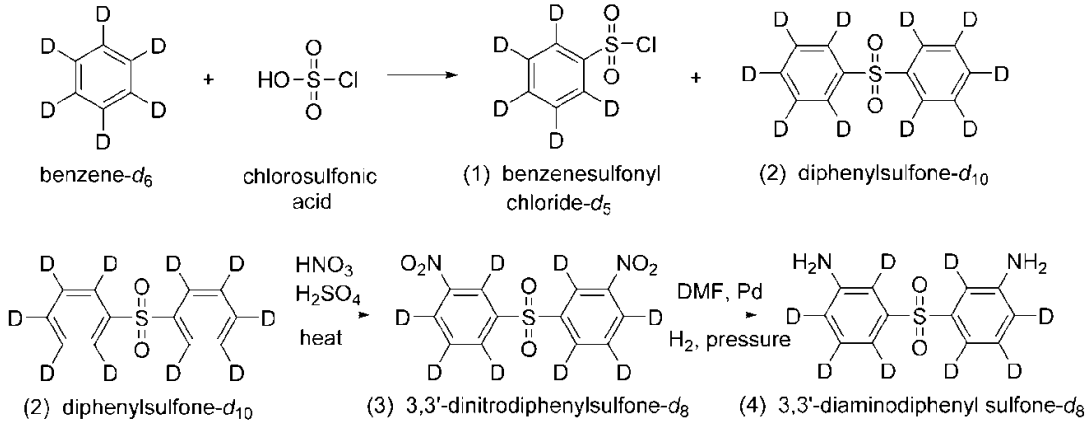

Figure 35. Synthesis of 33DDS-d_8.

Network Syntheses.[117] Diamine ring deuterated isomeric epoxy networks were prepared by reacting DGEBA with 33DDS-d_8 and 44DDS-d_8 at a 1:1 stoichiometric equivalent of oxirane to active hydrogen. Preparation steps are similar to the process for synthesizing BPA deuterated epoxies. The diamine-d_8 samples were observed to progress at a lower kinetic rate and require a long cure time. The molecular structures of the DDS deuterated epoxy networks are shown in Figure 36.

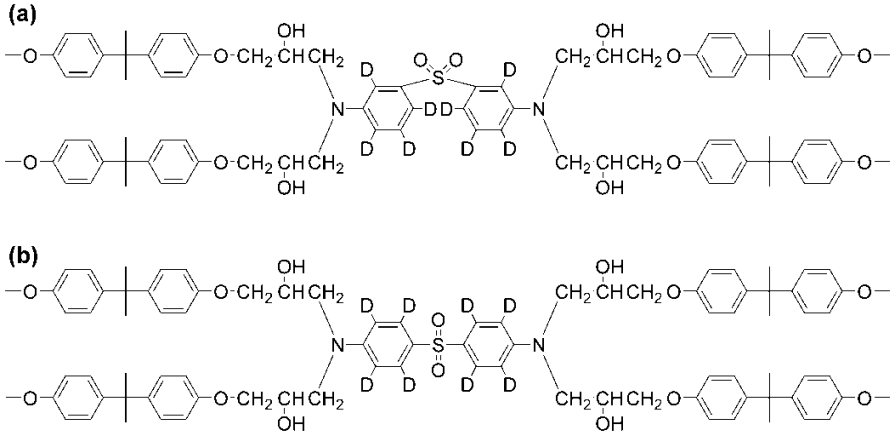

Figure 36. Structures of DDS deuterated epoxies: (a) 33A(DDS-d_8) and (b) 44A(DDS-d_8).

Thermal Characterization. The T_g's of 33A(DDS-d_8) and 44A(DDS-d_8) determined by DSC are 143 and 208 °C, respectively. 33A(DDS-d_8)'s T_g is about 20 °C lower than the T_g of non-deuterated 33A. 44A(DDS-d_8) has the same T_g as non-deuterated 44A.

Solid-state ^2H NMR Experiments. Solid-state ^2H NMR experiments were performed on a Varian UNITYINOVA NMR spectrometer equipped with a Tecmag wideline ^2H probe operating at 61.4 MHz (B_0 = 9.4 T). Fully relaxed quadrupolar echo spectra were acquired with a standard quadrupolar echo pulse sequence, 90_x-τ_1-90_y-τ_1-echo, with 90° pulse width of 2.5 µs and echo delay times τ_1 of 25, 50, 75, 100 and 150 µs. The spectral width was 2 MHz. The Free Induction Decay (FID) consisted of 2048 data points and was zero-filled to 4096 points. The FID was left-shifted to the echo maximum, and Gaussian line broadening of 3 kHz was applied prior to application of the Fourier transform. No Lorentzian line broadening was used.

Variable temperature quadrupolar echo spectra were acquired between -20 °C to 200 °C. Temperatures were calibrated by placing a thermocouple beside the RF coil which was removed prior to data acquisition.

Experimental Line Shapes

The ^2H quadrupolar echo line shapes for the network isomers measured at five echo delay times at different temperatures are shown in Figures 37 and 38.

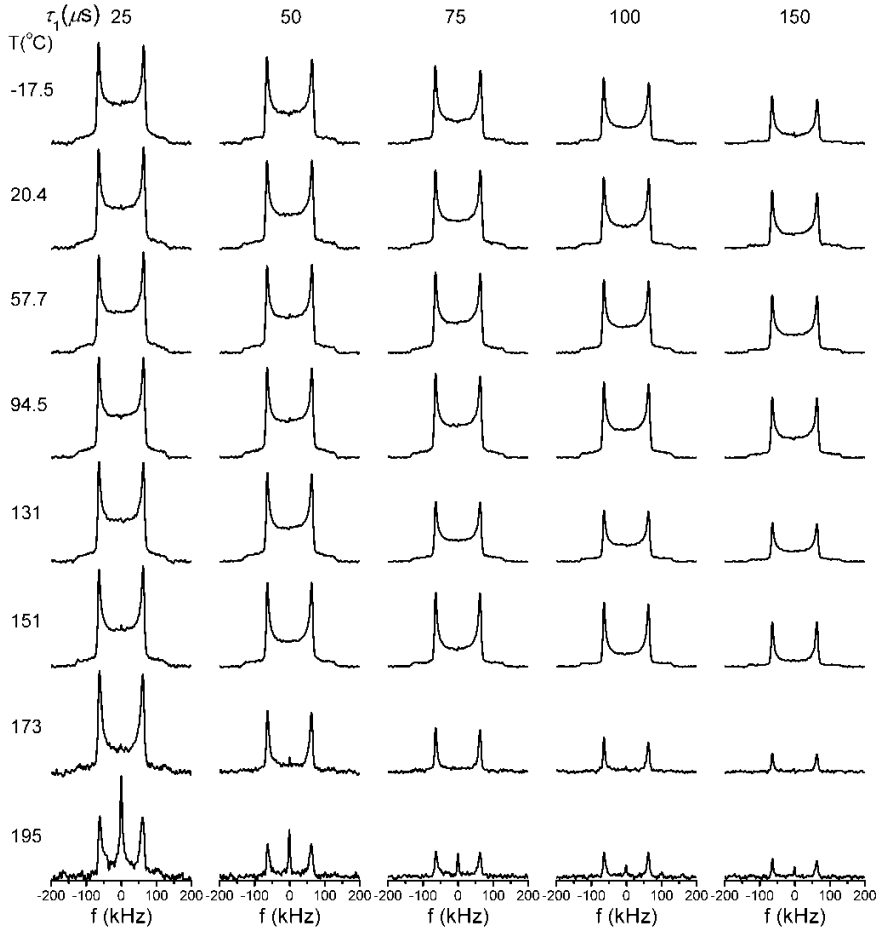

Figure 37. Experimental ^{2}H quadrupolar echo line shapes of 33A(DDS-d_8).

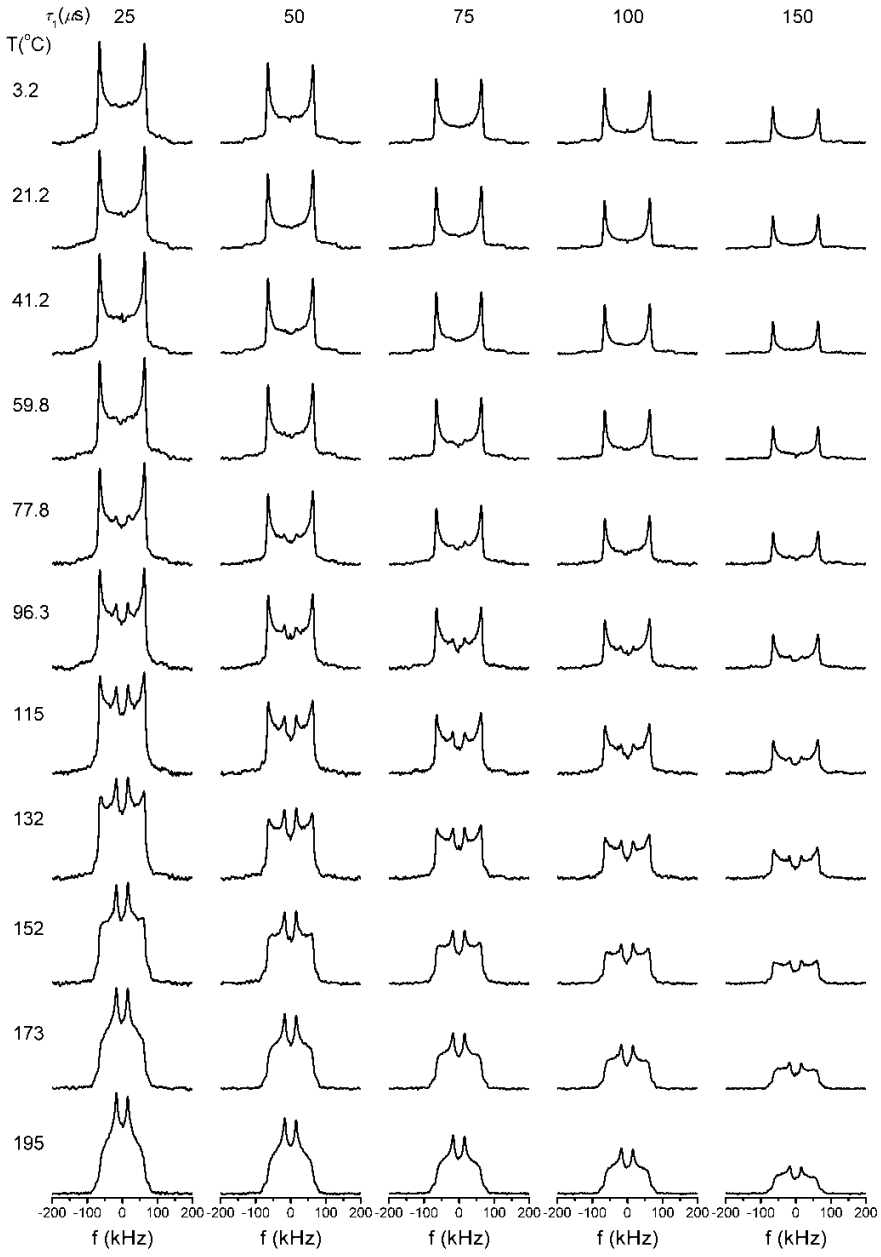

Figure 38. Experimental ^{2}H quadrupolar echo line shapes of 44A(DDS-d_8).

The same characteristic changes of line shapes with temperature and echo delay were observed for 44A(DDS-d_8) as for deuterated BPA rings in the epoxy networks (Chapter III), except that the 44DDS amine ring motions are slower than those of the

BPA rings (Figure 39); simulations (shown later) indicate that overall the DDS ring motions are approximately 10 times slower.

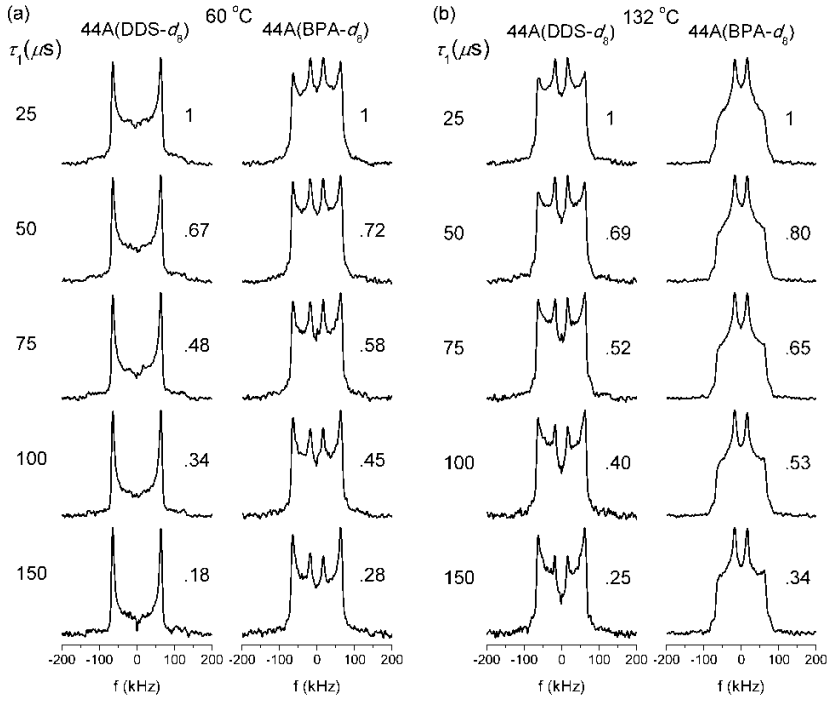

Figure 39. Comparison of the ^{2}H quadrupolar echo line shapes of 44A(DDS-d_8) and 44A(BPA-d_8) as a function of echo delay at 60 and 132 °C. The number next to each line shape is the echo intensity normalized to the τ_1 = 25 μs intensity.

The line shapes of 33DDS rings, on the other hand, are well represented by static Pake patterns at most sub-T_g temperatures, which indicates that these rings undergo no detectable large amplitude motions in the sub-T_g temperature range. Figure 40 shows the 33A(DDS-d_8) phenylene ring ^{2}H line shapes at 58, 94, 131, and 151 °C. At 58 and 94 °C static Pake powder patterns were observed, and only the center region of the Pake patterns decays slightly with increasing echo delay. This behavior is likely due to the presence of fast small-angle fluctuation.[120] At 131 and 151 °C the decay of the center region became more significant, indicating more dramatic chain fluctuation as

temperature reached T_g (143 °C). Simulations were not made to interpret the line shapes of 33A(DDS-d_8) and only fast small-angle fluctuation is presumed to be present.

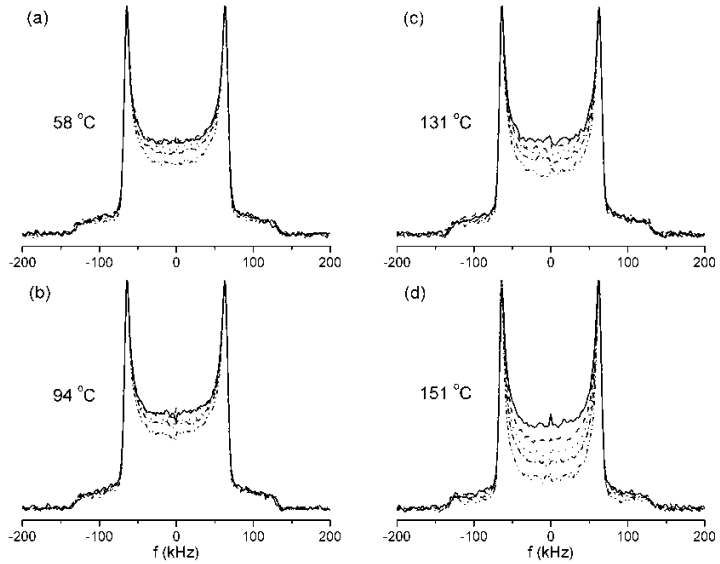

Figure 40. Normalized ^{2}H line shapes of 33A(DDS-d_8) phenylene rings at 58, 94, 131, and 151 °C. The center region of the Pake-like pattern diminishes as echo delay increases.

Line Shape Simulation Results

Simulation was made to interpret the experimental line shapes of 44A(DDS-d_8) following the procedure in Chapter III. Simulated spectra are obtained from a superposition of a series of line shapes calculated using a motional model combining ring π-flips and ring axis fluctuation; the contribution of each line shape to the overall spectrum is governed by a trivariate normal distribution. The experimental versus calculated line shapes for 44A(DDS-d_8) shown in Figure 41.

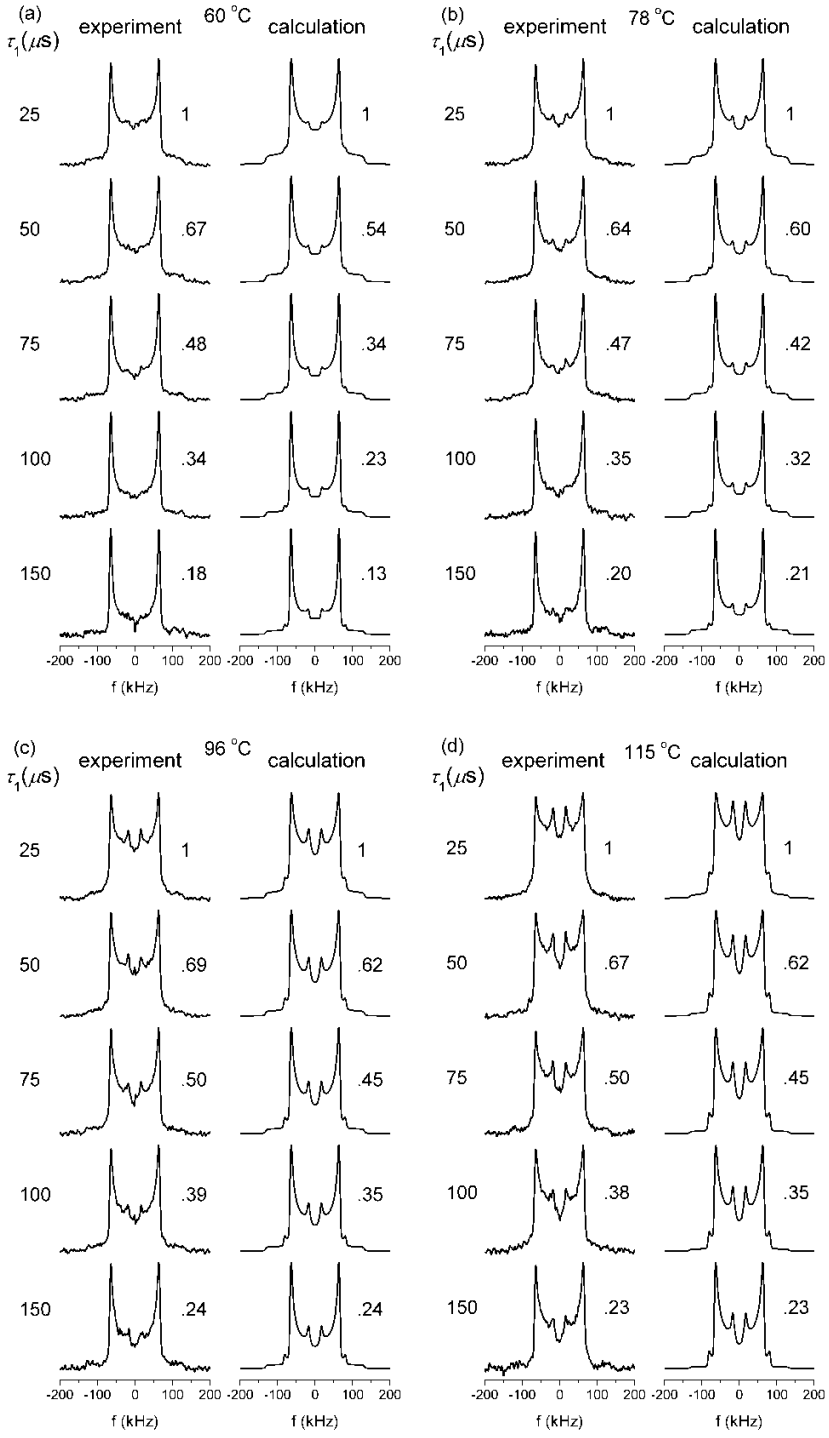
(a)
$\tau_1(\mu s)$
experiment
60 °C
calculation
25
50
75
100
150
1
.67
.48
.34
.18
1
.54
.34
.23
.13
-200 -100 0 100 200
f (kHz)
(b)
$\tau_1(\mu s)$
experiment
78 °C
calculation
25
50
75
100
150
1
.64
.47
.35
.20
1
.60
.42
.32
.21
-200 -100 0 100 200
f (kHz)
(c)
$\tau_1(\mu s)$
experiment
96 °C
calculation
25
50
75
100
150
1
.69
.50
.39
.24
1
.62
.45
.35
.24
-200 -100 0 100 200
f (kHz)
(d)
$\tau_1(\mu s)$
experiment
115 °C
calculation
25
50
75
100
150
1
.67
.50
.38
.23
1
.62
.45
.35
.23
-200 -100 0 100 200
f (kHz)

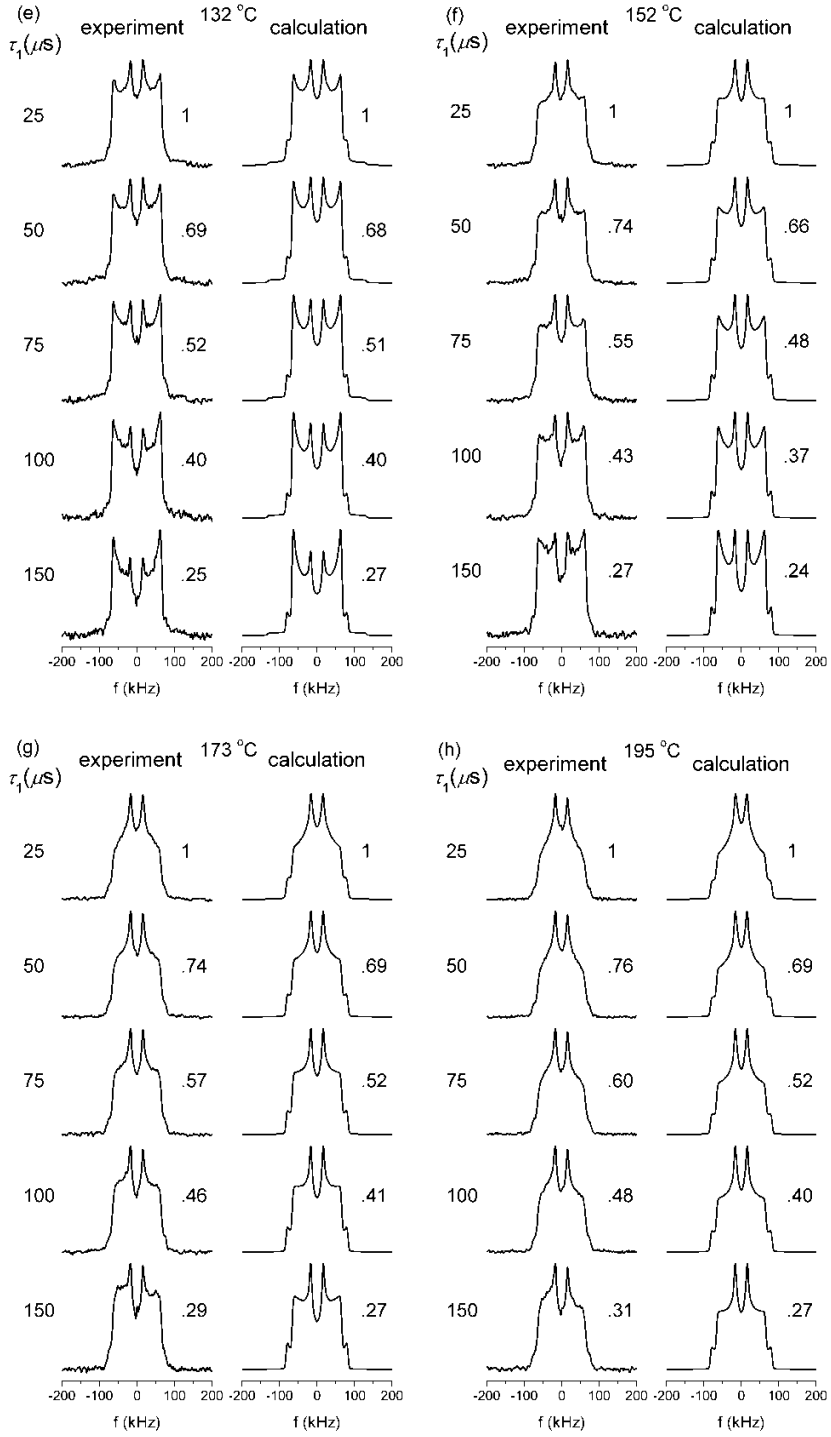

Figure 41. Experimental and calculated ^{2}H quadrupolar echo line shapes for 44A(DDS-d_8). The number next to each line shape is the echo intensity normalized to the τ_1 = 25 μs intensity.

The simulation parameters are summarized in Table 4, where $\tau_{c,1}$ is the π-flip correlation time (inverse of mean π-flip rate k_1), $\tau_{c,2}$ is the correlation time of ring axis fluctuation ($4/k_2$), and θ is the cone angle of the fluctuation. The variances σ_1, σ_2, and σ_θ indicate the widths of the corresponding distributions. The effective T_2 value based on the integral area of the full line shape for each temperature is also included in the table. The rate and cone angle distributions for 44A(DDS-d_8) at about 115 °C are graphically shown in Figure 42.

Table 4

Simulation parameters for 44A(DDS-d_8)

T (°C)	$\log(\tau_{c,1}/s)$	σ_1	$\log(\tau_{c,2}/s)$	σ_2	θ (°)	σ_θ (°)	T_2 (μs)
60	-4.1	0.5	-1.2	1	0	4	1000
78	-4.7	0.75	-1.5	1.5	5	2	1000
96	-5.2	1	-1.7	1.5	6	2	1000
115	-5.7	1	-1.8	1.5	8	2	800
132	-6.2	1.5	-2.0	1	8	2	800
152	-6.7	1	-2.3	1	8	4	800
173	-7.2	0.5	-2.5	1	8	6	1000
195	-7.7	0.5	-2.8	1	8	6	1000

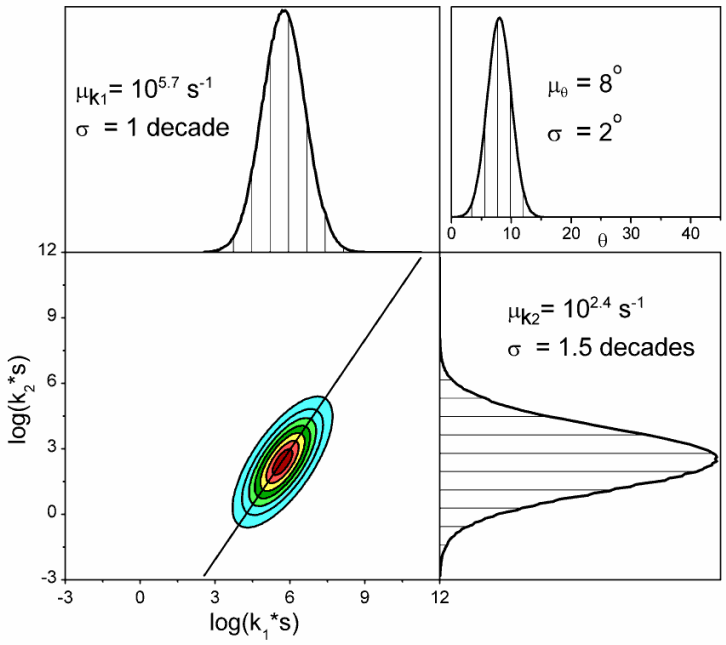

Figure 42. Plot showing the distributions of ring motional parameters in 44A(DDS-d_8) at 115 °C. The mean values and distribution widths of ring flip rate k_1, axis fluctuation rate k_2, and axis fluctuation cone angle θ are shown in the upper left, bottom right, and upper right figures, respectively. The bottom left figure shows the correlation between the distributions of k_1 and k_2.

Discussion

Distinct behaviors of cone angle distributions are found 44DDS rings as compared to BPA rings: while a half-Gaussian distribution centered at 0 is good to describe the dynamics of BPA rings, a full or part Gaussian distribution centered at a non-zero value is necessary for 44DDS rings. The dynamics of the 44DDS rings is found to be less heterogeneous than BPA rings as is manifested by the narrower distributions of the π-flip rates and cone angles of 44DDS rings. The narrower distribution of the π-flip rates is also reflected by the slightly faster decay of signal intensity with echo delay as compared to BPA rings (Figure 39).[122] This less heterogeneity might be related to the more symmetric molecular environment of 44DDS: it has four branches whereas BPA has two.

Linear temperature dependence of π-flip rate is found for 44A(DDS-d_8) as shown in Figure 43. This linear temperature dependency is questionable, however, because the lowest two temperatures simulated coincide with the temperature at which the temperature dependence of the BPA ring π-flip rates changes. Moreover, at 60 °C the reduction factors from simulation do not match those of experimental observation as nicely as they do at other temperatures, indicating that the simulation parameters at 60 °C might not perfectly describe the dynamics at that temperature. However, due to that the line shapes at below 60 °C cannot be fitted to yield useful numbers, effort is not made to address this issue and the linear dependency of π-flip rate on temperature is accepted.

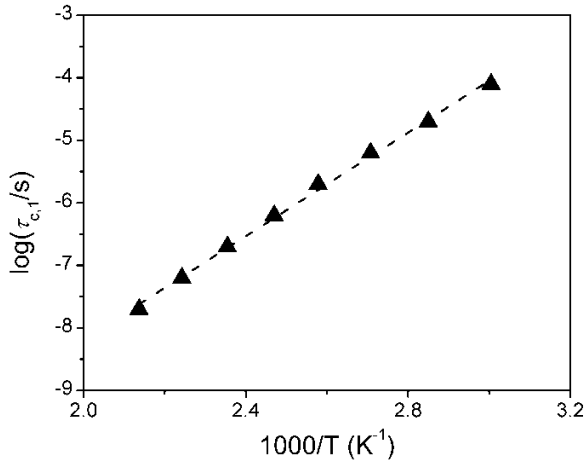

Figure 43. The Arrhenius plot: temperature dependence of 44DDS ring flip rates.

The Arrhenius Plot. An apparent activation energy of 79 kJ/mol for 44DDS ring flip motion is obtained from the slope of the linear fitting in its Arrhenius plot. Such high activation energy value is rarely seen for localized ring π-flip motions; common values are 40-55 kJ/mol. For example, the activation energy of 41 kJ/mol was determined for the ring π-flip motion in PES[95], which also contains a sulfone group between two phenylene

rings. The example of PES thus excludes the possibility that the high activation energy is due to the sulfone group. The value is however very close to the high temperature activation energies of BPA ring motions. Therefore, a question comes whether the DDS ring motion is correlated to the motion of the hydroxypropyl ether group as is the case with the BPA ring motions. However, with the line shapes below 60 °C not interpreted, a definite answer cannot be given. A possible explanation for such high activation energy is the fact that 44DDS is the crosslinker. According to the mechanical relaxation mechanism proposed by Yaris and Horii, phenylene rings need to propel neighboring chains to obtain certain space for the flip.[94,127] The denser packing of molecular chains at the crosslink makes it harder for 44DDS rings to make the flip, thus justifying the observation of high activation energy.

Contributions to γ Relaxations. Extrapolation of the Arrhenius plot to a time scale of 1 Hz shows 44DDS ring flip motions induce maximum mechanical loss at a temperature of -21 °C. Figure 44 is the DMA tan δ curves of 33A and 44A in the sub-T_g range. 44DDS ring flip motions thus contribute to the high temperature part of the γ relaxation of 44A. Note the span of the γ relaxation of 44A is wider than that of 33A; the high temperature part of the γ relaxation of 44A extends to higher temperature. Based on the analysis, this is apparently due to the contribution of the 44DDS ring flip motions to the mechanical relaxation of the 44A network. Very interestingly, the high temperature part of the mechanical relaxation peak of the crosslinked epoxy cannot be fitted in the work of Jones et al.[111] In their work, only the motions of the hydroxypropyl ether group and the phenylene rings were studied. It is likely that the missing part in their fitting was due to the ring motions of the MDA crosslinker.

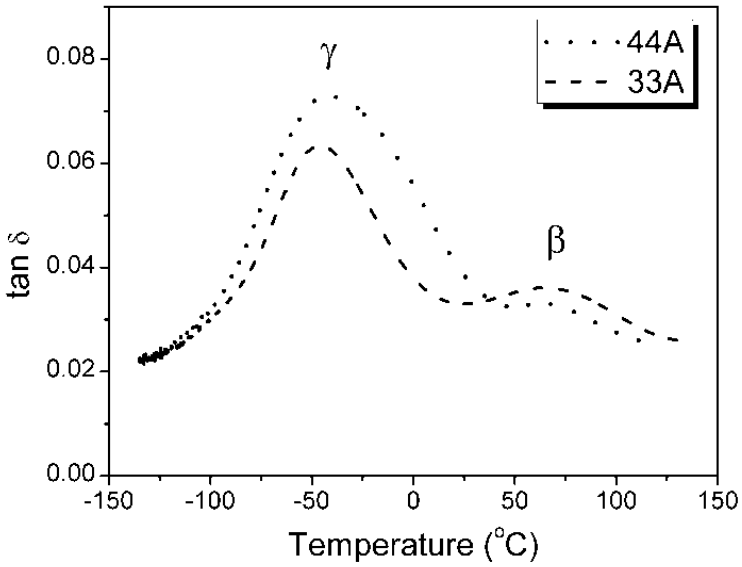

Figure 44. Dynamical mechanical tan δ spectra of 33A and 44A epoxies in the sub-T_g temperature range.

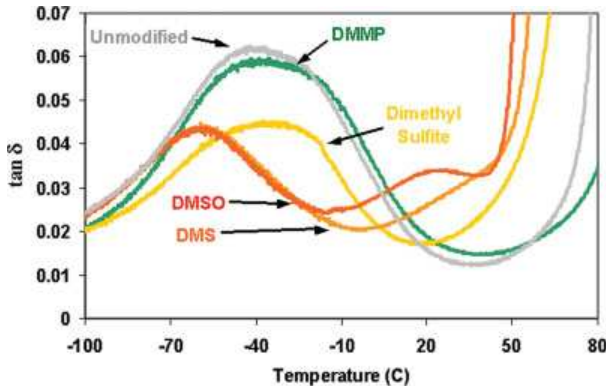

Figure 45. The β relaxations in some epoxies modified with sulfur based compounds. Reproduced from reference with permission.[133]

Anti-plasticization Effect. As mentioned in the introduction, the 33A network resembles an anti-plasticized 44A network in its mechanical and thermal properties. The molecular origin of this anti-plasticization is explained here through solid-state NMR. It is commonly reported in literature that anti-plasticization decreases the magnitude of the higher temperature side of the secondary peak, due to suppression of some molecular

motions.[133,134,135,136] For example, Lesser et al. found that the addition to model epoxies of sulfur based modifiers, including dimethyl sulfoxide (DMSO), dimethyl sulfone (DMS), and dimethyl sulfite, make epoxies stiffer and suppress the high temperature part of their β relaxations, as shown in Figure 45.[133] Multi-technique NMR studies revealed filling of free volume in the epoxies by the additives and a minor decrease of local segmental polymer backbone motion.[136] In our work, the 33DDS diamine ring motions are suppressed and the diamine backbones only undergo fast small-angle fluctuation, whereas the 44DDS diamine rings undergo flip motions and the diamine backbones actively fluctuate and sweep out certain molecular space. The occurrence of molecular motions in solid polymers is known to decrease their mechanical moduli.[69] That explains why 44A has a lower modulus than 33A. The swept-out space, on the other hand, is evidenced in free volume measurements, which find that the averaged hole-size free volume of 44A is larger than that of the 33A system.[73] Therefore, the anti-plasticization effect is related to the meta-substitution on the phenylene rings in the 33DDS diamine which suppresses large amplitude motions and leads to more compact packing in 33A.

Conclusions

Isomeic epoxy networks 33A and 44A exhibit substantial differences in thermal, mechanical, and morphological properties. Especially, 33A resembles an anti-plasticized 44A. Deuterated 33A and 44A networks with deuteration on their diamine rings were synthesized to investigate the role of these motions in the mechanical relaxation of the two networks and explain at a molecular level the anti-plasticization effect through ^{2}H NMR line shape analysis.

The 44DDS ring motion is found to contribute to the high temperature part of 44A's γ relaxation. The activation energy of 44DDS ring flip motion is high, possibly due to the rigid nature of 44DDS, as well as it being the crosslink. The 44DDS diamine rings undergo flip motions and the diamine backbones actively fluctuate and sweep out certain molecular space. The occurrence of 44DDS ring motions decreases the modulus of 44A and the swept-out space from the fluctuation of the 44DDS ring axis explains the higher hole-size free volume. 33DDS rings do not exhibit large amplitude motions but only undergo fast small-angle fluctuations, which results in a decrease in the magnitude of the high temperature part of the γ relaxation of 33A, a phenomenon often seen in the anti-plasticization process. Therefore the anti-plasticization effect is attributed to the meta-substitution on the diamine phenylene rings which suppresses large amplitude motions and leads to more compact packing in 33A.

CHAPTER V

STUDY OF CHAIN SEGMENT MOTIONS IN CROSSLINKED EPOXIES

Introduction

Deuterium (^{2}H) NMR spectroscopy has proven in the last two chapters to be a powerful tool in characterizing the molecular dynamics of the aromatic groups in the 33A and 44A isomeric epoxies and elucidating the structure-dynamics-property relationships of the epoxies. According to the studies, the DDS rings were found to differ greatly due to isomeric substitution positions. The 33DDS rings, which lack a rotation axis due to the meta-substitution, do not show any large amplitude motions but only fast small-angle fluctuations. The 44DDS rings are able to undergo π-flip motions that appear in high temperature mechanical relaxation spectra. The difference in the DDS molecular motions indeed account largely for the anti-plasticization effect seen in the 33A system. On the other hand, the BPA rings in the two systems do not show significant motional differences in the glassy state and they have similar contributions to the secondary relaxation peaks. The fact that the DDS ring dynamics do not affect the BPA ring dynamics is slightly unexpected but is at the same time reasonable.

One other molecular segment in the epoxies that has not been examined yet is the hydroxypropyl ether (HPE) group. The HPE moiety serves as the connecting group of the aromatic groups. Since the difference between the DDS rings in 33A and 44A isomeric networks is the greatest while that of the BPA is minimal, one would expect interesting behavioral differences between the HPE groups of the two.

Experimental Section

Materials. 3,3'-diaminodiphenylsulfone (33DDS, 97%), and 4,4'-diaminodiphenylsulfone (44DDS, 97%) were purchased from Sigma Aldrich and used as received. Custom synthesized diglycidyl ether of bisphenol A with perdeuterated epoxide group (DGEBA-d_{10}, 98%) was provided by Cambridge Isotope Laboratories, Inc., and used as received. Diglycidyl ether of bisphenol A (DGEBA, MW = 350-360 g/mol) was purchased from Momentive.

Network Syntheses. A mixture of DGEBA- d_{10} (20%) and DGEBA (80%) was added to a GPC vial. A GPC vial was used because of the small amount of samples needed which is around 0.5 g when the sample is cured. Diamine powders were added to the epoxy mixture at an equivalent ratio of epoxide groups to reactive amine hydrogens. The GPC vials placed in an oil bath for heating, and a small piece of steel was added into the vials for stirring. The initial temperature was set to 110 °C for the amines to be dissolved in the epoxy and then vacuum was applied to the vials provided by a vacuum pump to drive the dissolved air out of the mixture of epoxy and amine. The stirring and vacuum were applied until a clear looking, homogeneous mixture was obtained. The GPC vials were then placed in a programmable conventional oven to cure the resin. A standard cure procedure which is 125 °C for 5 hours and 225 °C for 2 hours is used. The glass vials containing the cured resins were sacrificed and the resins were broken into small size particles which were enclosed in high precision NMR glass tubes for testing.

The structures of the final products are shown in Figure 46. They will be denoted 33A(HPE-d_{10}) and 44A(HPE-d_{10}) hereafter.

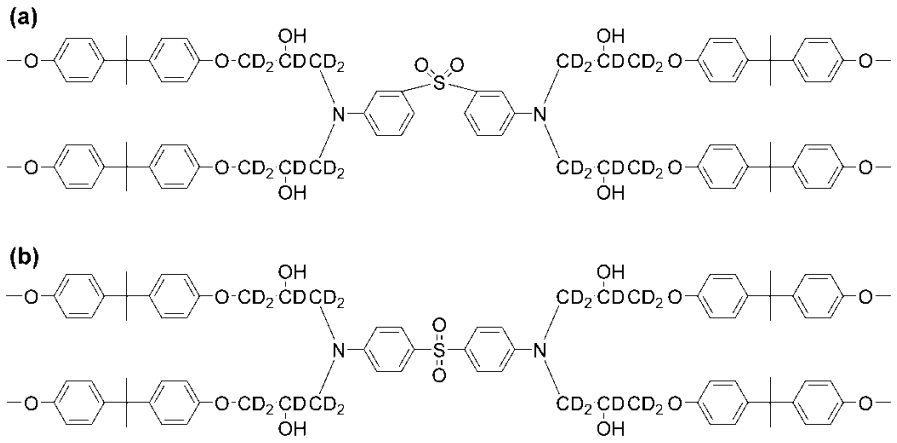

Figure 46. Structures of HPE deuterated epoxies: (a) 33A(HPE-d_{10}), and (b) 44A(HPE-d_{10}).

Thermal Characterization. The T_g's of 33A(HPE-d_{10}) and 44A(HPE-d_{10}) as determined by DSC are 170 °C and 210 °C, respectively, the same values as the non-deuterated materials.

Solid-state ^2H NMR Experiments. Solid-state ^{2}H NMR experiments were performed on a Varian UNITYINOVA NMR spectrometer equipped with a Tecmag wideline ^{2}H probe operating at 61.4 MHz (B_0 = 9.4 T). Fully relaxed quadrupolar echo spectra were acquired with a standard quadrupolar echo pulse sequence, 90_x-τ_1-90_y-τ_1-echo, with 90° pulse width of 2.5 µs and echo delay times τ_1 of 25, 50, 75, 100 and 150 µs. The spectral width was 2 MHz. The Free Induction Decay (FID) consisted of 2048 data points and was zero-filled to 4096 points. The FID was left-shifted to the echo maximum, and Gaussian line broadening of 3 kHz was applied prior to application of the Fourier transform. No Lorentzian line broadening was used. Variable temperature quadrupolar echo spectra were acquired between -20 °C to 200 °C. Temperatures were calibrated by placing a thermocouple beside the RF coil which was removed prior to data acquisition.

Experimental Line Shapes

The ^{2}H quadrupolar echo line shapes for the network isomers 33A(HPE-d_{10}) and 44A(HPE-d_{10}) measured at five echo delay times at different temperatures are shown in Figures 47 and 48.

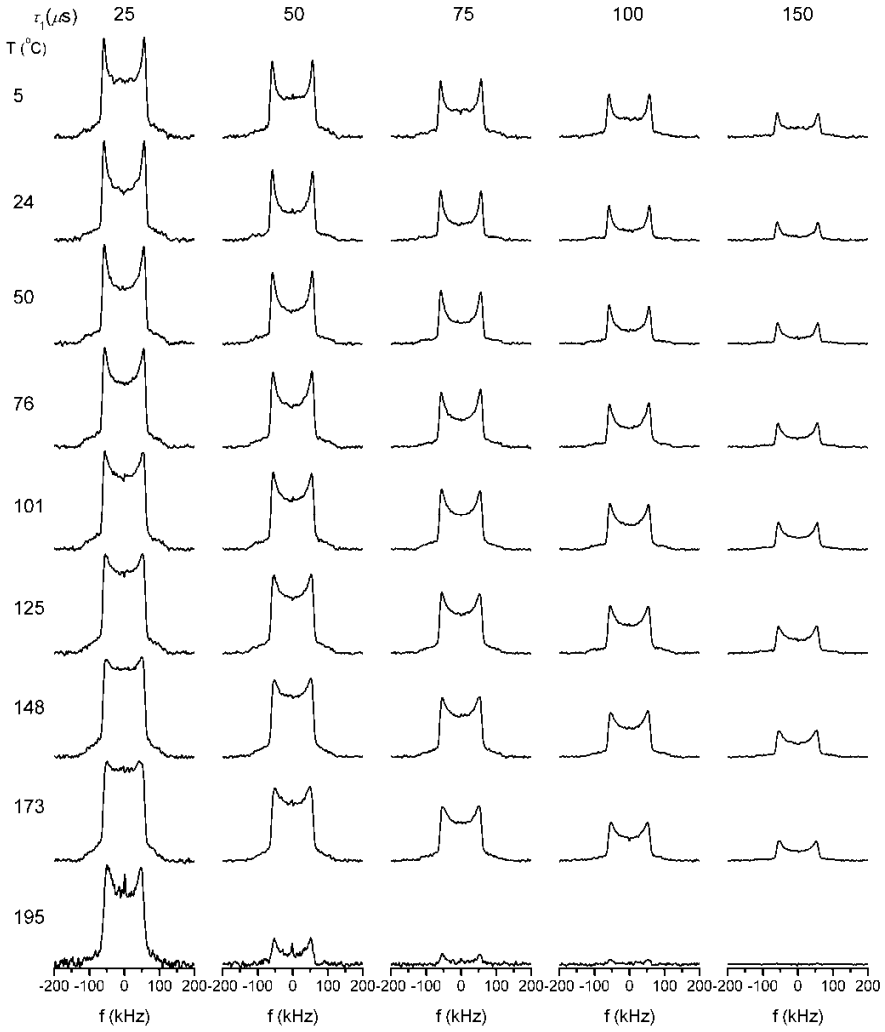

Figure 47. Experimental ^{2}H quadrupolar echo line shapes of 33A(HPE-d_{10}).

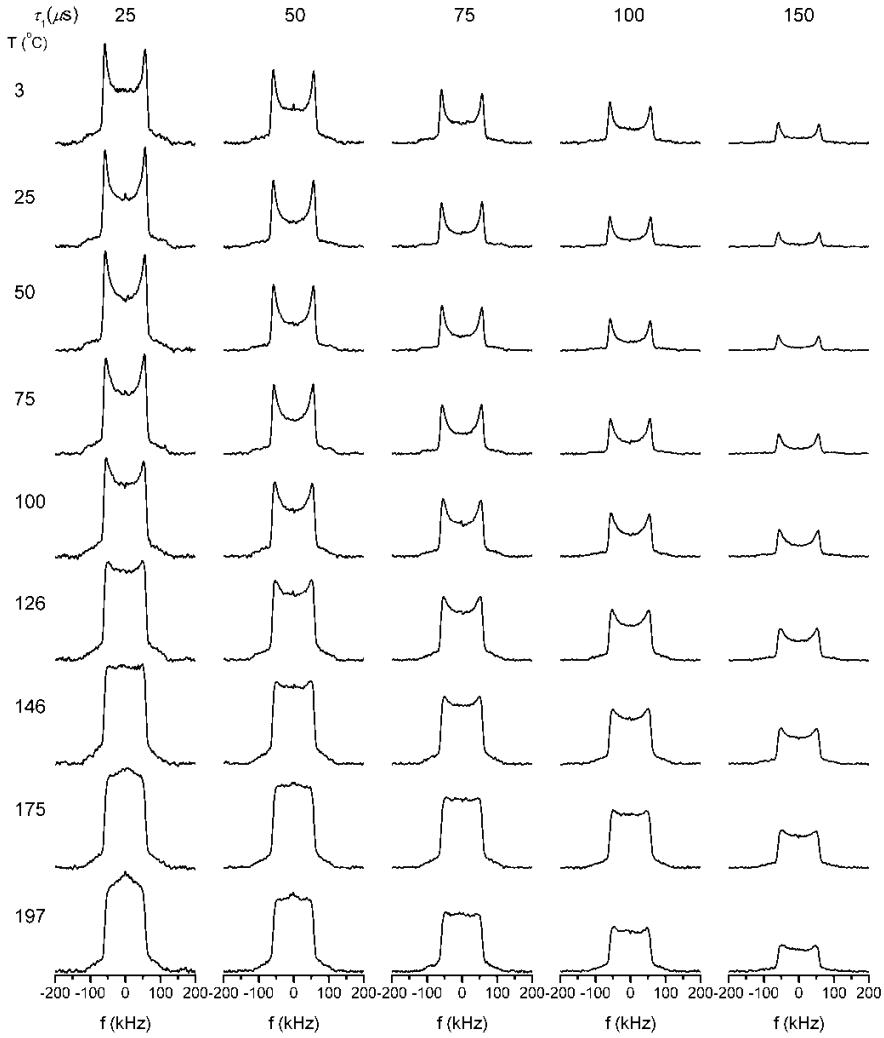

Figure 48. Experimental ^{2}H quadrupolar echo line shapes of 44A(HPE-d_{10}).

These ^{2}H quadrupolar echo line shapes of HPE groups are very different from the phenylene ring line shapes where characteristic singlularities of phenylene ring π-flips were almost always observed, indicating well-defined motional jumps. In contrast, the HPE chain line shapes do not show evidence of any distinctive singularities as temperature increases; only the center region of the line shapes grows. At best, at a temperature close to the glass transition temperature of 44A, the line shape of the 44A(HPE-d_{10}) sample shows a dull peak at zero frequency. Also, the effect of T_g on the

signal intensity is highlighted here. At 195 °C for the 33A(HPE-d_{10}), 20 °C above its T_g, signal decays ultra fast to almost zero at long echo delay (150 μs) due to fast T_2 relaxation.

Figure 49 compares the line shapes of 33A(HPE-d_{10}) and 44A(HPE-d_{10}) as a function of echo delay at all experimental temperatures. The line shapes of the two systems are very similar up to 100 °C, with only minor differences in their reduction factors, (Figure 49a-e). Above 100 °C the center region of the line shape of 44A(HPE-d_{10}) starts to outgrow that of the 33A(HPE-d_{10}) (Figure 49f-i), indicating a faster motional rate for the HPE group in 44A. These will be examined in further detail in the Discussion section.

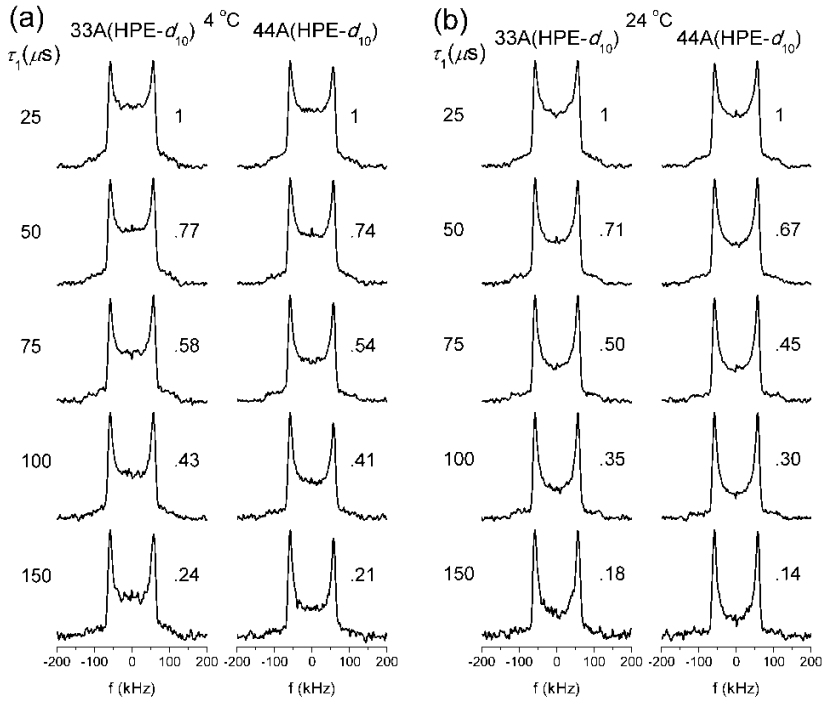

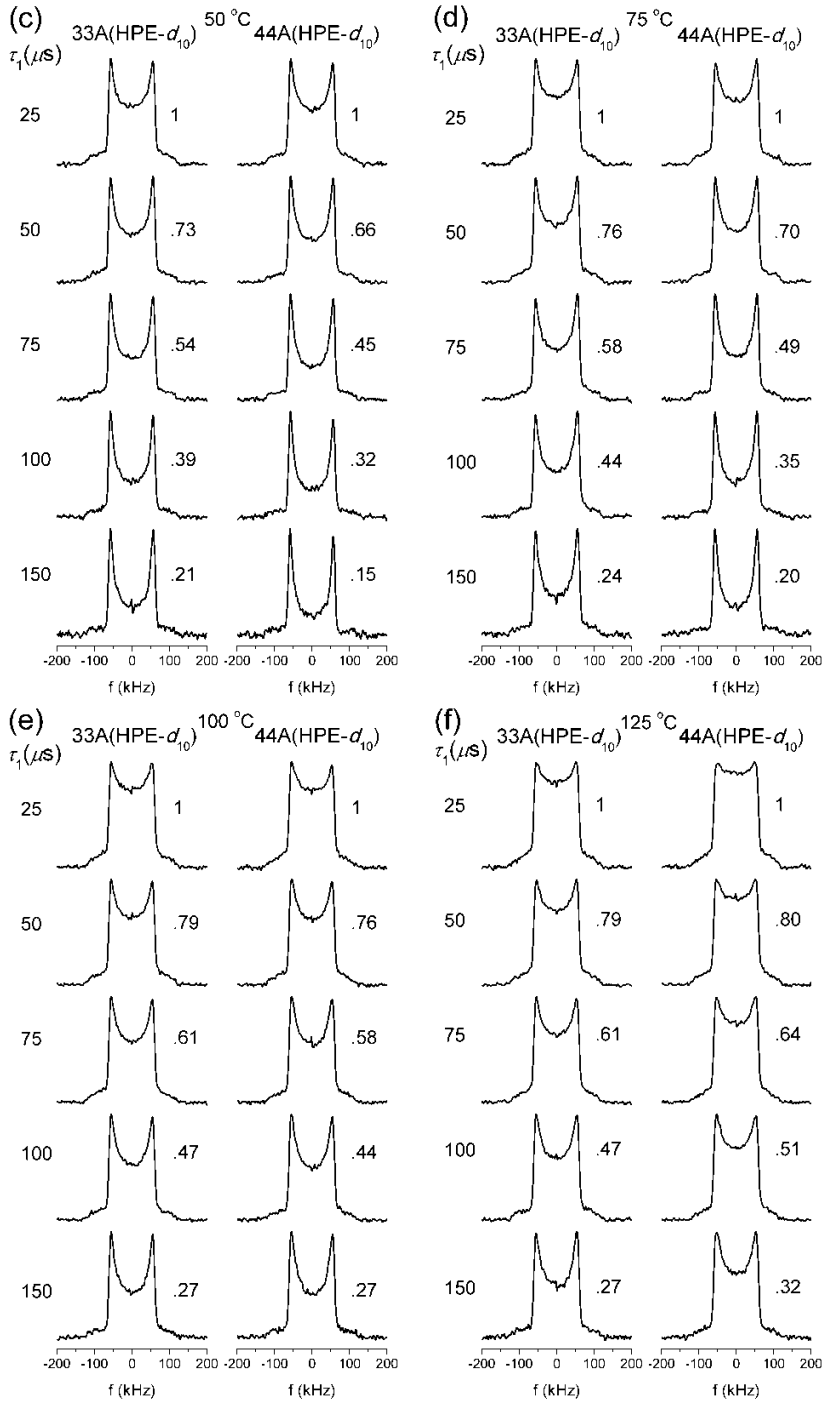
(c)
33A(HPE-d_{10}) 50 °C 44A(HPE-d_{10})
τ_1(μs)
25 1 1
50 .73 .66
75 .54 .45
100 .39 .32
150 .21 .15
-200 -100 0 100 200
f (kHz)
(d)
33A(HPE-d_{10}) 75 °C 44A(HPE-d_{10})
τ_1(μs)
25 1 1
50 .76 .70
75 .58 .49
100 .44 .35
150 .24 .20
(e)
33A(HPE-d_{10}) 100 °C 44A(HPE-d_{10})
τ_1(μs)
25 1 1
50 .79 .76
75 .61 .58
100 .47 .44
150 .27 .27
(f)
33A(HPE-d_{10}) 125 °C 44A(HPE-d_{10})
τ_1(μs)
25 1 1
50 .79 .80
75 .61 .64
100 .47 .51
150 .27 .32

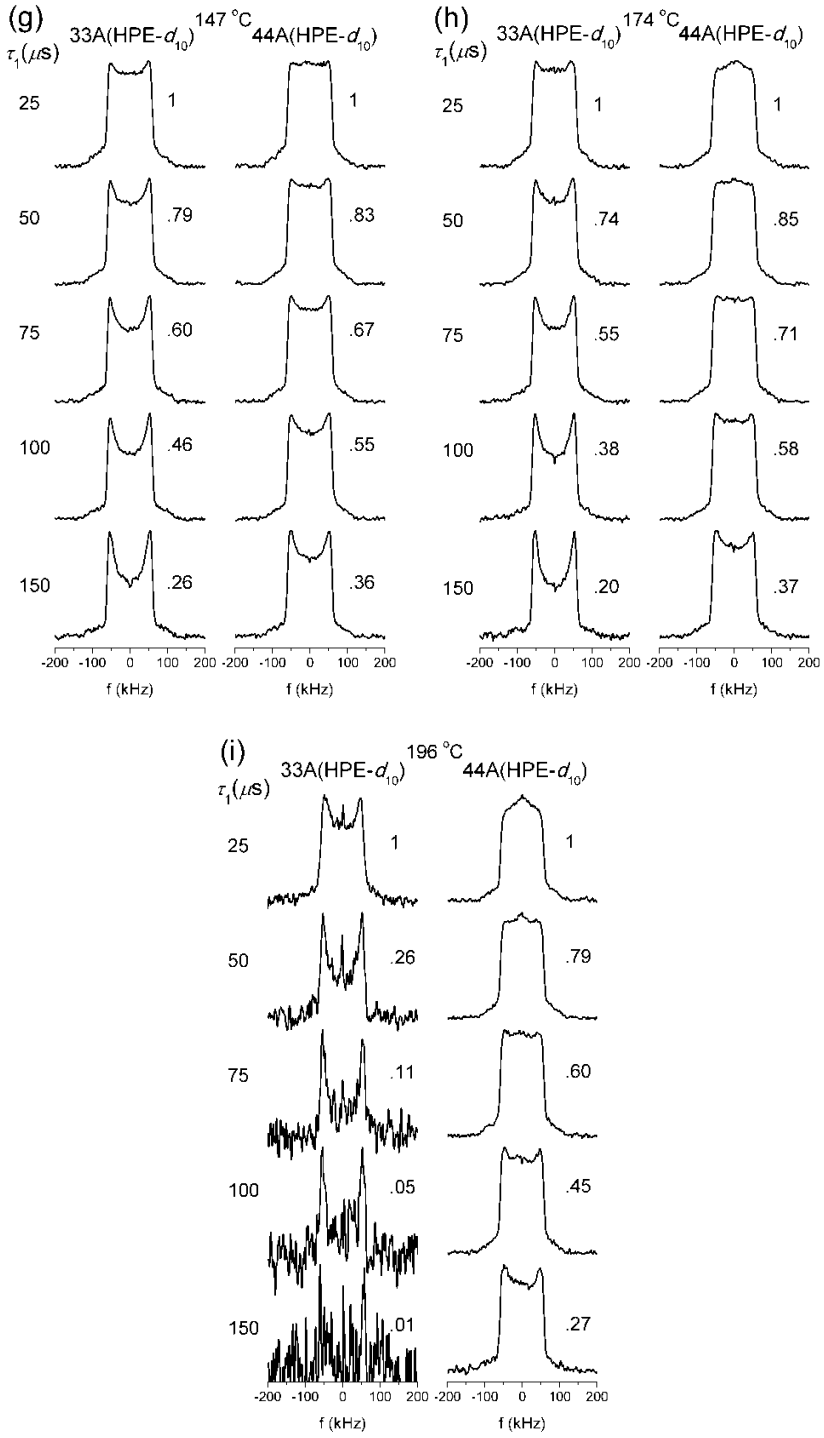

Figure 49. Comparison of the ^{2}H line shapes of 33A(HPE-d_{10}) and 44A(HPE-d_{10}) as a function of temperature and echo delay. The echo intensity normalized to the value at τ_1 = 25 μs is shown. Note the strong effect of T_g on the signal intensities.

Line Shape Simulation

EXPRESS is used to simulate line shapes to determine the geometries, rates and rate distributions of the HPE chain motions.[118,119] The principles that apply to the simulation of phenylene ring line shapes apply here as well. Molecular motions in amorphous glasses are heterogeneous; therefore, a simulated spectrum is a superposition of a series of individual line shapes characterized by single motional rates and amplitudes, and the contribution of each individual line shape to the overall line shape is governed by a distribution function.

A quadrupolar splitting of 120 kHz is measured from room temperature spectra which gives a quadrupolar coupling constant (QCC) value of 160 kHz. This value might be pre-averaged, due to fast libration, from the true QCC which is usually ca. 170 kHz for deuterium connected to an aliphatic carbon. Hereafter, the pre-averaged QCC value 160 kHz will be used. As the temperature increases, the quadrupolar splitting of the line shapes is still ca. 120 kHz, although the center of the pattern grows. In the fast-exchange limit, e.g., the τ_1 = 25 μs spectrum of 44A(HPE-d_{10}) at 196 °C, the spectrum is essentially an η = 1 pattern (largest spectral density at zero frequency, see Equation 8), which suggests that the motional process leading to collapse of static powder pattern has twofold or lower symmetry.[137] Furthermore, the breadth of the pattern (120 kHz) suggests that the motional process involves a conformational transition through an angle whose bisecter is approximately the “magic angle”, or 54.7°.[138] A trans-gauche conformational transition meets such conditions. The process is illustrated in Figure 50.

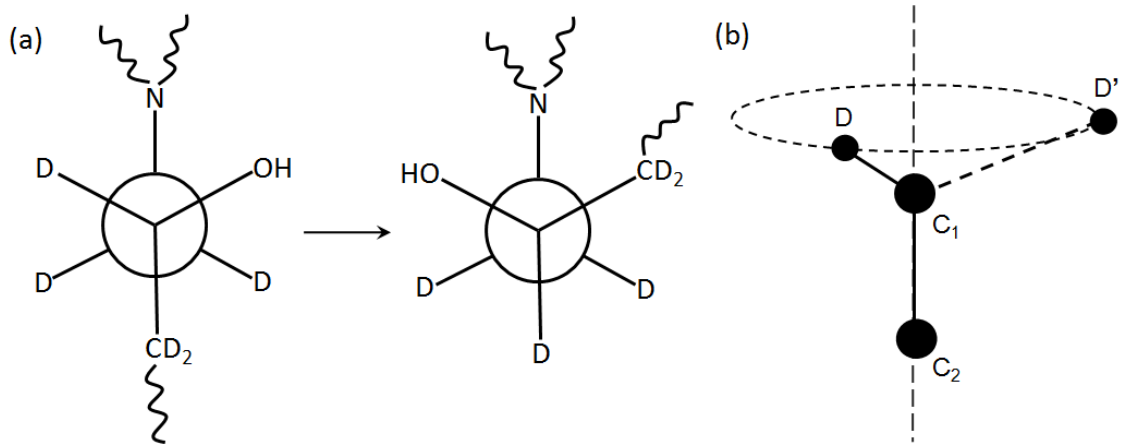

Figure 50. Trans-gauche conformational transition: (a) the C-D bonds rotate around a C-C axis for 120°. (b) A simplified model for the transition: the C_1-D bond orients in the C_1-D' direction after the transition. The actual vector jump angle (D-C_1-D') is 109.5°.

The ^{2}H line shape resulting from a 120° trans-gauche conformational transition is shown in Figure 51, which is characterized by a spectral width of 120 kHz and a sharp peak at zero frequency. Simulation efforts demonstrated that such well-defined motions did not generate line shapes as experimentally observed; distinctive singularities at zero frequency were always present.[101] The center region is not accounted for by simple 120° jumps, even with a superposition of line shapes for different motional rates.

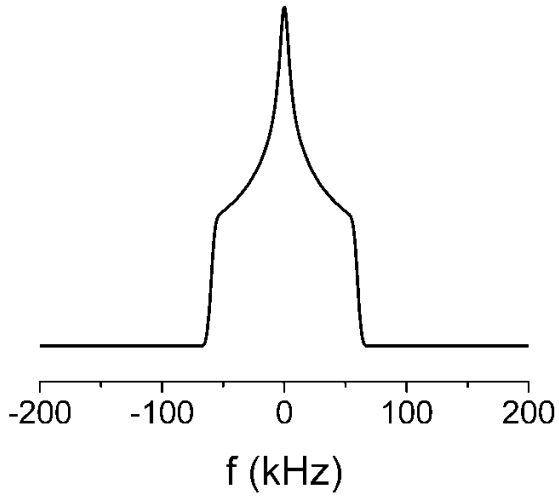

Figure 51. ^{2}H line shape of a 120° trans-gauche conformational transition in the fast motion limit.

English et al. studied the molecular motions of methylene units in Nylon 66 using solid-state ^{2}H NMR line shape analysis.[100,101] Similar line shapes as observed here were found for methylene motions in the amorphous phase of Nylon 66. They precisely described the dynamics of the methylene groups using a bimodal model, with mode I being the librational motion operative in both free and constrained domains and mode II postulated to be trans-gauche jumps operative only in the free domain. The bimodal model also reflected the semi-crystalline nature of Nylon 66 where two different subpopulations were existent due to either morphological (e.g., chain folds / interfacial and free amorphous) or local (hydrogen bonding) constraints. They demonstrated that line shapes for the methylene motions in the amorphous phase could be duplicated using *inhomogeneous distributions of motional amplitudes*, instead of using distributions of motional rates, which has been successfully applied to the simulation of line shapes for phenylene ring motions. Indeed, if the methylene motions are taken as ill-defined, i.e., not centered around 120° jumps, superposition of line shapes with non-zero-frequency

singularities from jumps of different amplitudes smears out the distinctive singularity and results in line shapes as experimental ones.

Here, a model is used that describes ill-defined jumps of a C-D bond around a C-C axis, the angle between the C-D bond and the C-C axis being the tetrahedral angle, as shown in Figure 52. In this model, the C-D bond, while keeping a constant tetrahedral angle 109.5° with the axis it jumps around, is allowed to jump at a rate of *k* between two sites separated by a jump angle φ. Therefore, two variables of the model are the jump amplitude ϕ and jump rate *k*. Three line shapes calculated for jumps based on the model are shown in Figure 53 to provide a visual aid to understand how the positions of the singularities change with φ and *k*.

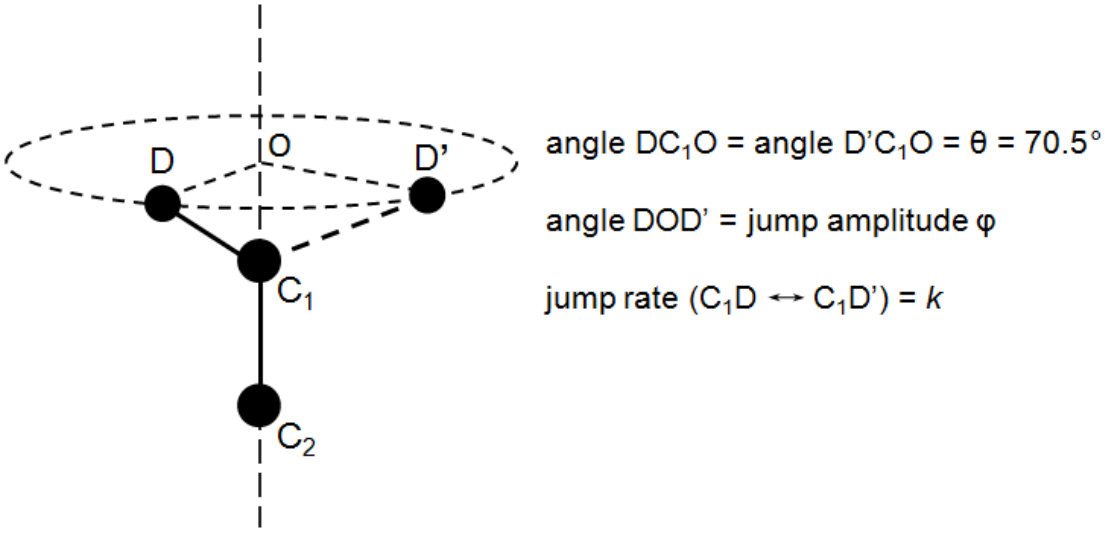

Figure 52. Model for HPE chain motion.

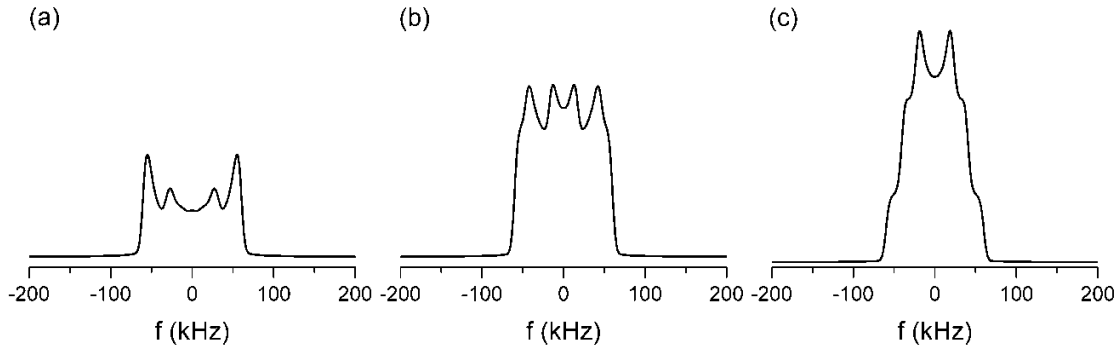

Figure 53. Line shapes calculated based on HPE motional model: (a) φ = 96°, $k = 10^5$ s^{-1}; (b) φ = 108°, $k = 10^6$ s^{-1}; (c) φ = 90°, $k = 10^7$ s^{-1}.

The QCC value of 160 kHz was used for all simulations, and the asymmetry parameter was set to 0. Calculated FIDs were left-shifted to echo maximums, and Gaussian broadening of 8 kHz was applied prior to application of Fourier transform. Correction for finite pulse width effects was not attempted.[128] A bivariate normal distribution $\{\mu_k, \sigma_k; \mu_\varphi, \sigma_\varphi\}$ of methylene jump rate log(k) and jump amplitude φ was employed. This distribution and its relationship to the overall line shape J is expressed in Equation 11:

$$J = \int j(k,\varphi) \cdot \mathrm{P}(k,\varphi) d(\varphi) d(k) \qquad \text{Equation 11}$$

Here, $j(k,\varphi)$ is the deuterium line shape resulting from HPE chain undergoing a specific motion as described by the model, and P(k,φ) is the probability density of such rings in the system. The covariance $r_{(k,\varphi)}$ that describes the correlation between the jump rate and the jump amplitude is set to 0.6.

Simulation Results

The experimental versus calculated ^{2}H quadrupolar echo line shapes as a function of increasing echo delay and temperatures for 33A(HPE-d_{10}) and 44A(HPE- d_{10}) are shown in Figures 54 and 55, respectively.

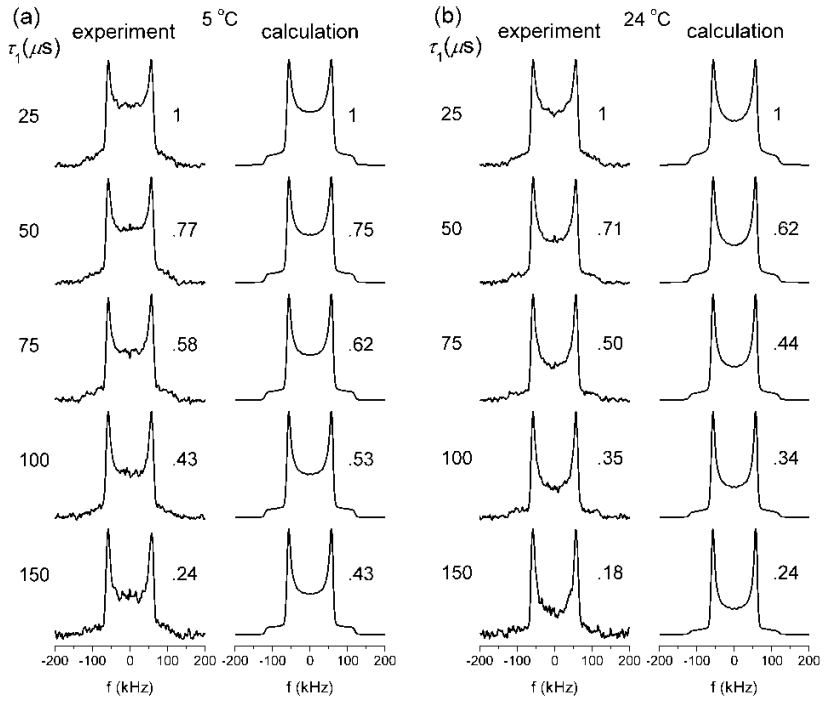

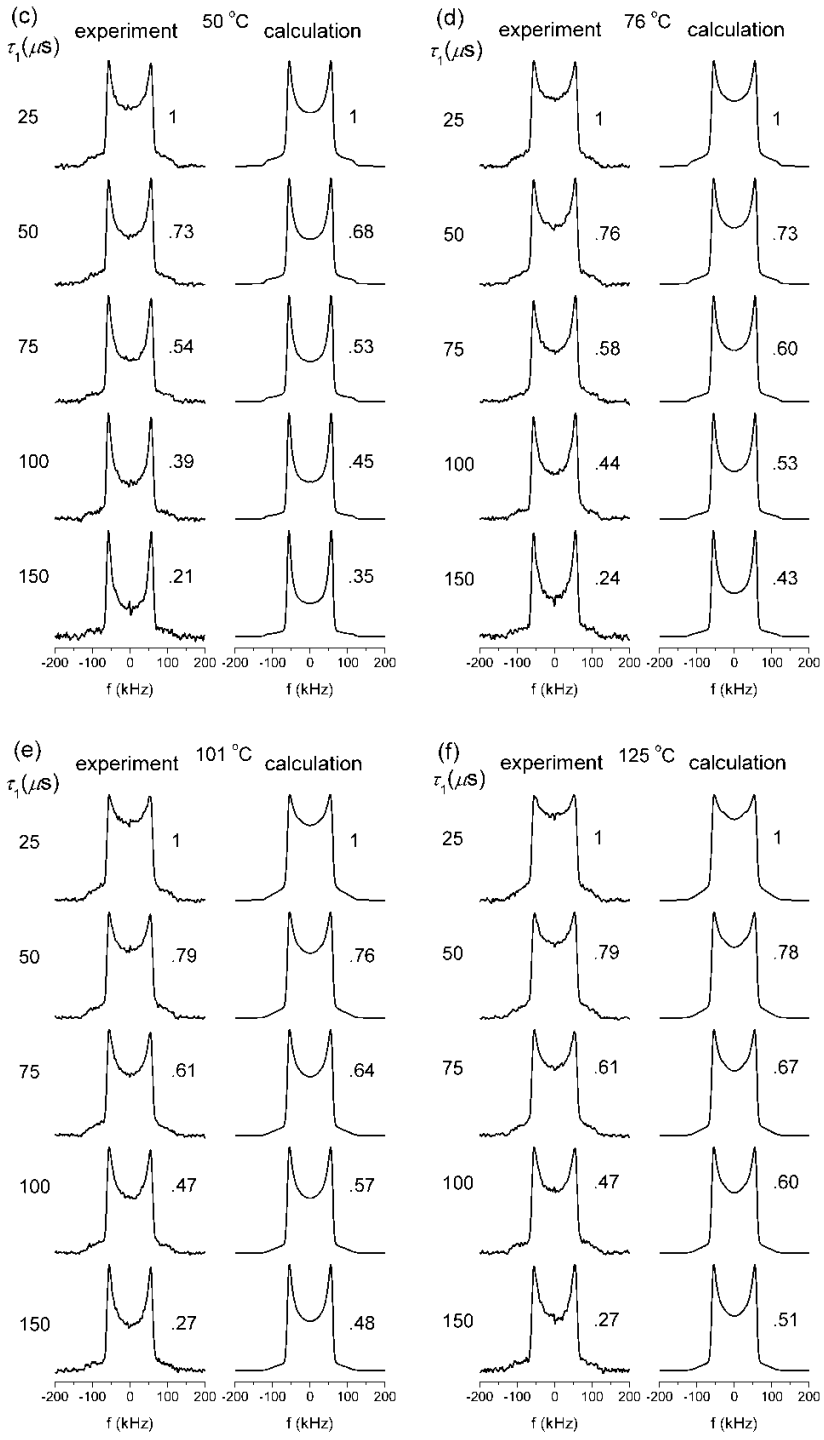
(c)
experiment
50 °C
calculation
$\tau_1(\mu s)$
25
50
75
100
150
1
.73
.54
.39
.21
1
.68
.53
.45
.35
-200 -100 0 100 200
f (kHz)
(d)
experiment
76 °C
calculation
$\tau_1(\mu s)$
25
50
75
100
150
1
.76
.58
.44
.24
1
.73
.60
.53
.43
-200 -100 0 100 200
f (kHz)
(e)
experiment
101 °C
calculation
$\tau_1(\mu s)$
25
50
75
100
150
1
.79
.61
.47
.27
1
.76
.64
.57
.48
-200 -100 0 100 200
f (kHz)
(f)
experiment
125 °C
calculation
$\tau_1(\mu s)$
25
50
75
100
150
1
.79
.61
.47
.27
1
.78
.67
.60
.51
-200 -100 0 100 200
f (kHz)

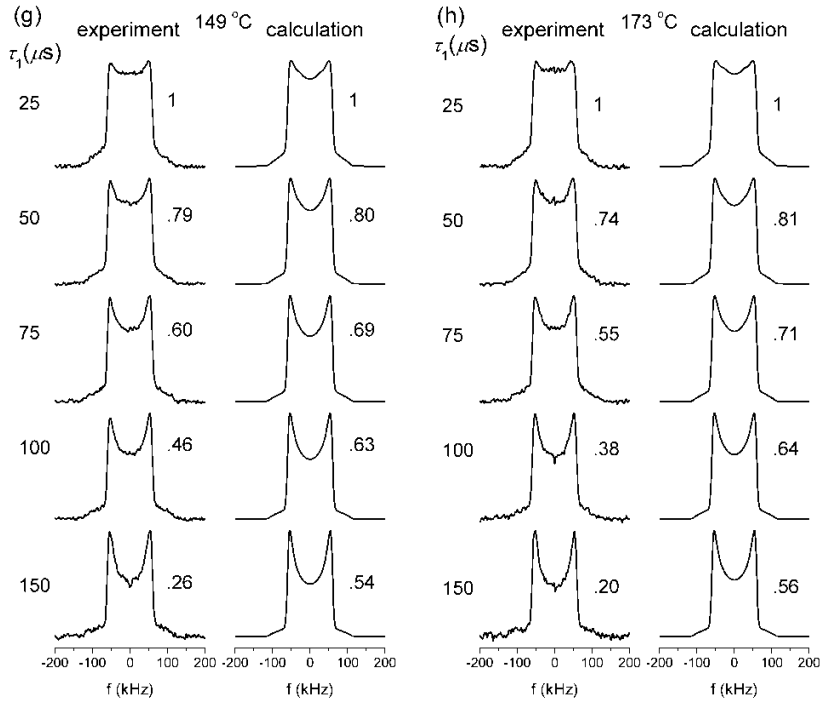

Figure 54. Experimental and calculated ^{2}H quadrupolar echo line shapes for 33A(HPE-d_{10}). The echo intensity normalized to the value at τ_1 = 25 μs is shown.

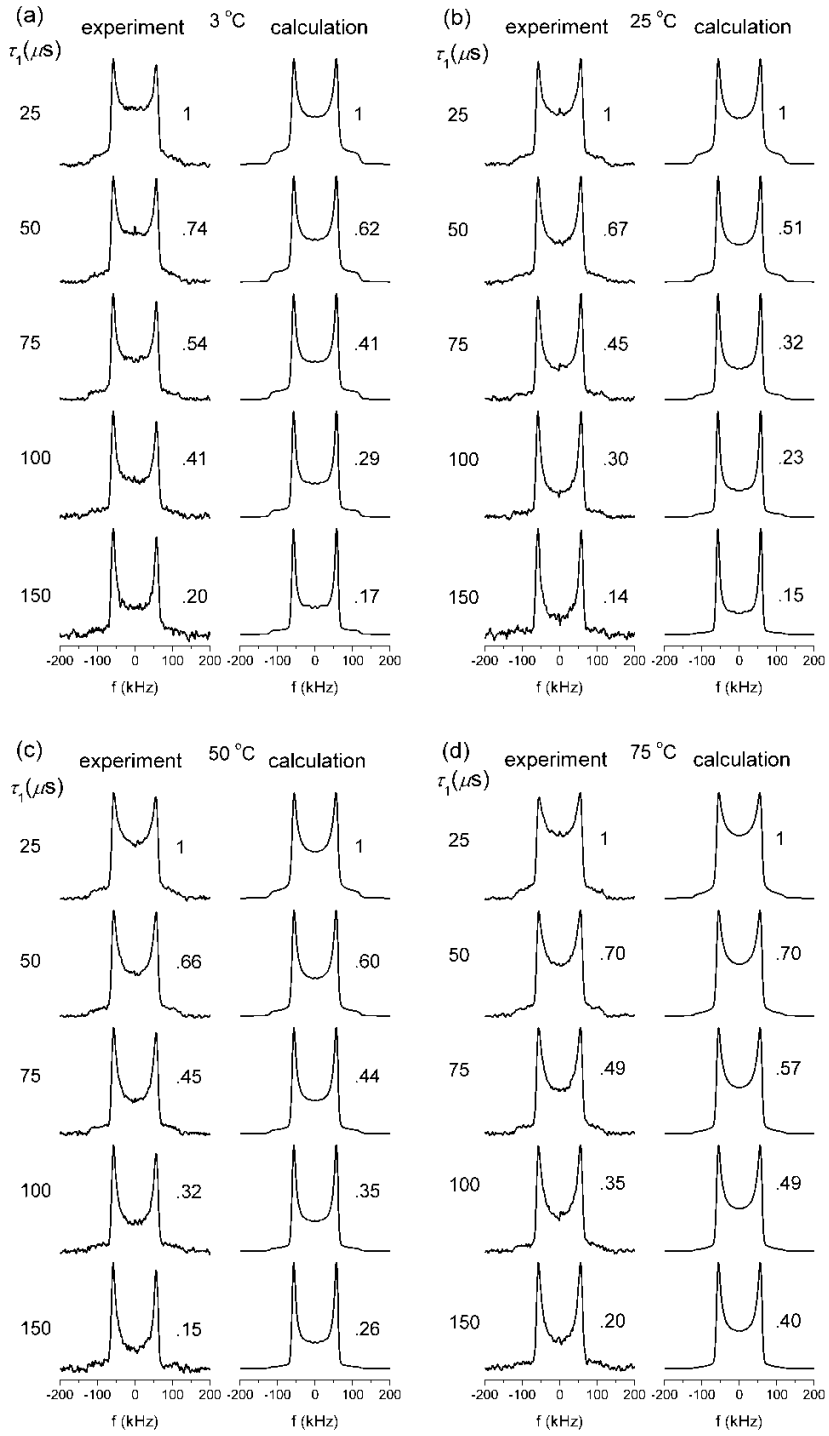
(a)
experiment
3 °C
calculation
$\tau_1(\mu s)$
25
50
75
100
150
1
.74
.54
.41
.20
1
.62
.41
.29
.17
-200 -100 0 100 200
f (kHz)
(b)
experiment
25 °C
calculation
$\tau_1(\mu s)$
25
50
75
100
150
1
.67
.45
.30
.14
1
.51
.32
.23
.15
-200 -100 0 100 200
f (kHz)
(c)
experiment
50 °C
calculation
$\tau_1(\mu s)$
25
50
75
100
150
1
.66
.45
.32
.15
1
.60
.44
.35
.26
-200 -100 0 100 200
f (kHz)
(d)
experiment
75 °C
calculation
$\tau_1(\mu s)$
25
50
75
100
150
1
.70
.49
.35
.20
1
.70
.57
.49
.40
-200 -100 0 100 200
f (kHz)

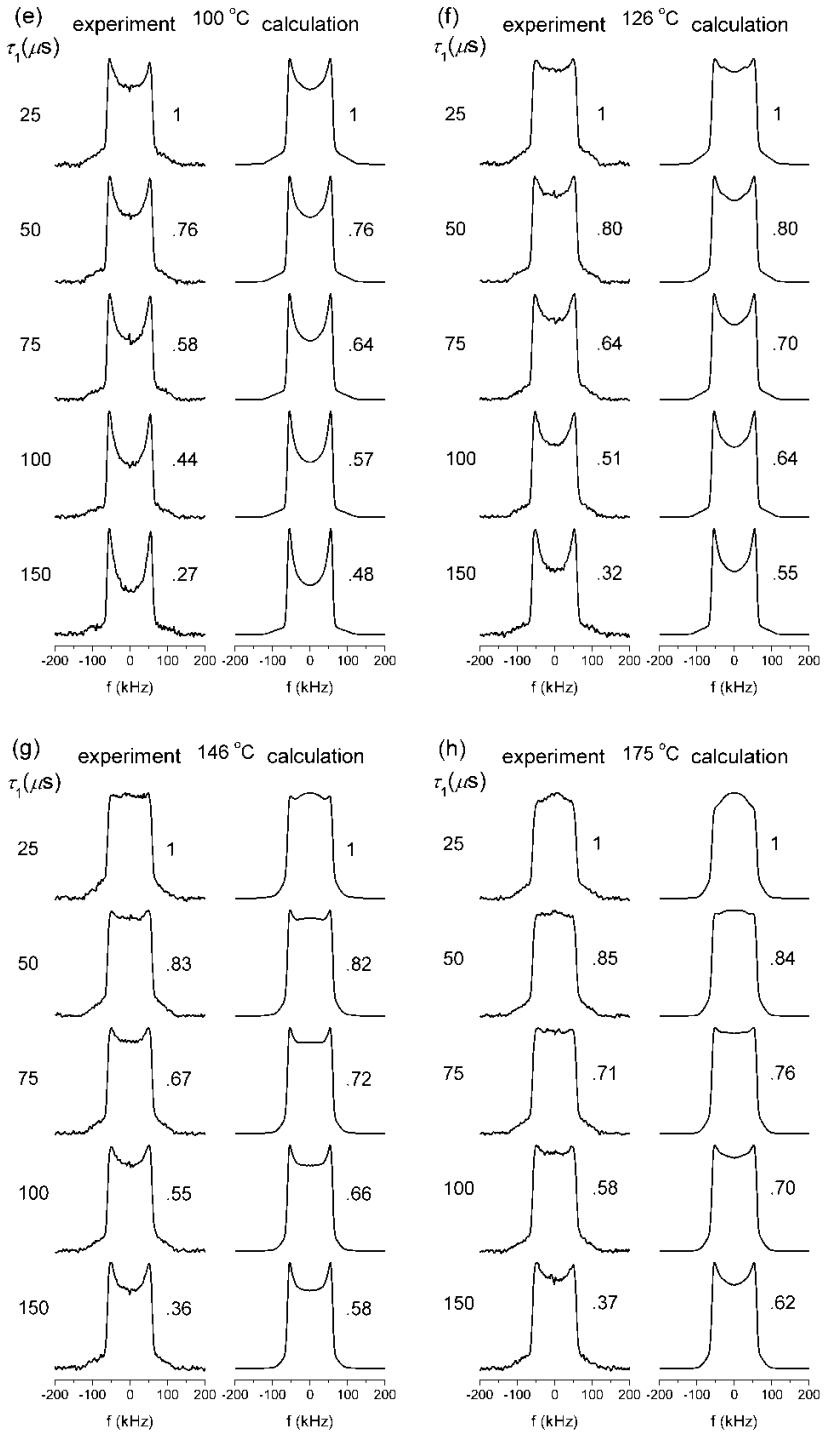
(e)
experiment 100 °C calculation
$\tau_1(\mu s)$
25
50
75
100
150
1
.76
.58
.44
.27
1
.76
.64
.57
.48
-200 -100 0 100 200
f (kHz)
(f)
experiment 126 °C calculation
$\tau_1(\mu s)$
25
50
75
100
150
1
.80
.64
.51
.32
1
.80
.70
.64
.55
-200 -100 0 100 200
f (kHz)
(g)
experiment 146 °C calculation
$\tau_1(\mu s)$
25
50
75
100
150
1
.83
.67
.55
.36
1
.82
.72
.66
.58
-200 -100 0 100 200
f (kHz)
(h)
experiment 175 °C calculation
$\tau_1(\mu s)$
25
50
75
100
150
1
.85
.71
.58
.37
1
.84
.76
.70
.62
-200 -100 0 100 200
f (kHz)

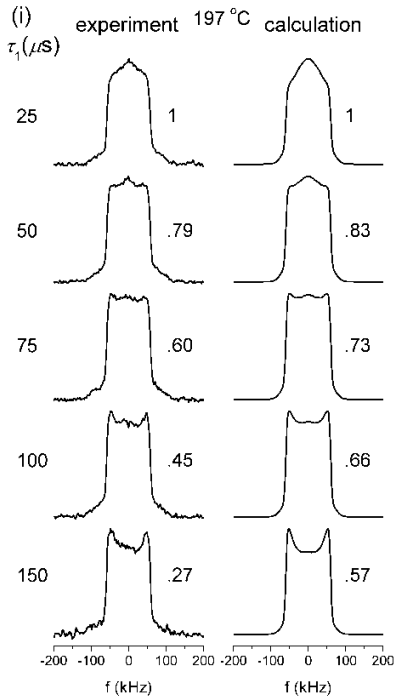

Figure 55. Experimental and calculated ^{2}H quadrupolar echo line shapes for 44A(HPE-d_{10}). The echo intensity normalized to the value at τ_1 = 25 μs is shown.

The simulation parameters are summarized in Tables 5 and 6; here, τ_c is the motional correlation time (inverse of mean jump rate *k*), and φ is the mean jump amplitude. The variances σ_k and σ_φ indicate the widths of the corresponding distributions. Note that in the calculated line shapes do not match the experimental ones very well in their echo delay dependence of signal intensities. This is partly due to that no effective T_2 parameters were incorporated into the line shapes.

Table 5

Simulation parameters for 33A(HPE-d_{10})

T (°C)	log(τ_c/s)	σ_k	φ (°)	σ_φ (°)
5	-4.1	0.5	84	20
24	-4.4	0.5	78	30
50	-4.8	0.75	72	20
76	-5.1	1	66	30
101	-5.4	1	60	30
125	-5.6	1	60	25
149	-5.9	0.75	60	30
173	-6.2	0.75	60	30

Table 6

Simulation parameters for 44A(HPE-d_{10})

T (°C)	log(τ_c/s)	σ_k	φ (°)	σ_φ (°)
3	-4.1	0.25	84	20
25	-4.4	0.25	80	25
50	-4.8	0.5	78	20
75	-5.2	0.75	72	20
100	-5.4	1	60	30
126	-5.8	1	60	30
146	-6.1	1	66	12
175	-6.5	0.75	66	12
197	-6.8	0.5	72	12

Discussion

General Observations. As was shown earlier, up to 100 °C the line shapes of the two HPE-d_{10} chains are similar, indicating similar dynamics. Line shape calculation indeed proved that the motional rates and jump amplitudes are very close in this temperature range. Other observations include: a) The rate of the motion, as described by the model (Figure 52) as the jump of one C-D bond around a C-C axis increases with increasing temperature. The temperature dependence of the rate is of major interest of

this research and will be discussed later. b) The distribution of motional rates, which reflects the dynamic heterogeneity, broadens as temperature increases but decreases when the temperature approaches T_g, indicating that glassy state dynamics are even more heterogeneous than those of glass transition. c) The two-site jump angle actually decreases as temperature increases. This is because of the growing easiness of molecular motion with increasing temperature so that molecular motions are more compensated by the rearrangement of others, but what NMR signals reflect is the absolute spatial displacements of spin orientations.

The Arrhenius Plot. The temperature dependence of the two-site jump motional rate is again examined in the Arrhenius plot (Figure 56). The temperature dependence undergoes an inflection at about 100 °C. This is in excellent agreement with the observation in the BPA rings motions, for which the inflection point was at above 67 °C. The activation energies below and above 100 °C were then calculated and denoted $E_{a,\gamma}$ and $E_{a,\beta}$, respectively. The fittings were extrapolated to a 1 Hz time scale (the frequency of dynamic mechanical testing) in order to predict the temperature at which maximum mechanical loss induced by ring flips occurs. Calculated results are shown in Table 7. When locating these temperatures in the DMA tan δ curves shown in Figure 32, it was found that HPE motions contribute to the very low temperature region of the spectra, in contrast with Jones' work, which shows that the contribution of HPE motion to the mechanical relaxation shows at a higher temperature than phenylene rings do in a DGEBA based epoxy cured with MDA.[111]

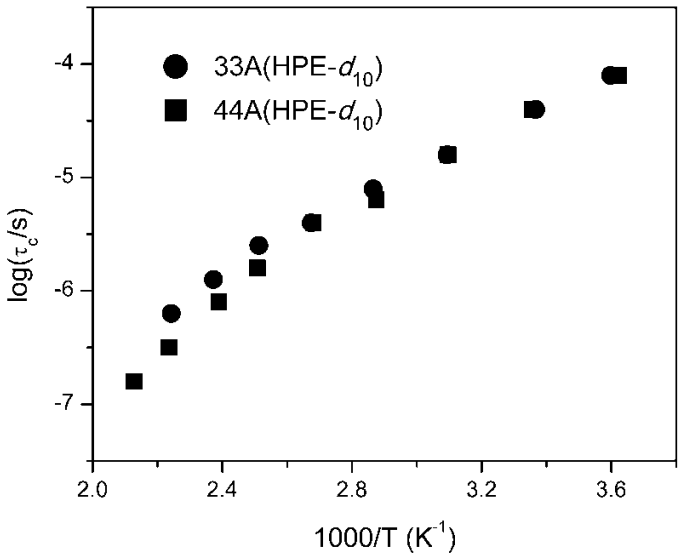

Figure 56. The Arrhenius plot shows the temperature dependence of the two-site jump rate.

Table 7

Activation energies and temperatures of 1 Hz HPE chain two-site jumps

	$E_{a,\gamma}$ (kJ/mol)	T($\tau_{c,1}$=1s) (^oC)	$E_{a,\beta}$ (kJ/mol)	T(τ_β = 1s) (^oC)
33A(HPE-d_{10})	26.9	-119	42.5	-74.3
44A(HPE-d_{10})	27.5	-118	50.2	-61.0

Chain Cooperativity. The same increase of activation energy and the inflection of the temperature dependence as observed in BPA ring motions occur at 100 °C. A similar conclusion can be drawn from this study: The observation of the inflection point suggests that the β relaxations of the epoxy networks could be due to motions of molecular chains of length scale longer than the HPE moiety. Combining previous results, the molecular origin of the β relaxations is possibly the cooperative motion of the DGEBA repeat unit.

Below 100 °C, the HPE segments do not exhibit significant difference in their dynamic behaviors. Again, this suggests that the local environment of the HPE segments

is similar for the isomers at such temperatures. The diamine crosslinkers do not significantly affect the HPE dynamics, indicating that the molecular motions of the HPE segments are localized in the deep glassy state. Differences in the HPE segment dynamics start to show up at 100 °C, which is lower than the corresponding temperature for BPA rings motions, indicating that the correlation length of the HPE chain motion grows as temperature increases, but due to the proximity of the HPE chain to the crosslink, the diamines start to influence the dynamics of HPE chain motions earlier. At above 100 °C, the HPE segments in 33A are less mobile than those in 44A because they are connected to 33DDS moieties, which have been shown to be relatively static due to the meta-substitution.

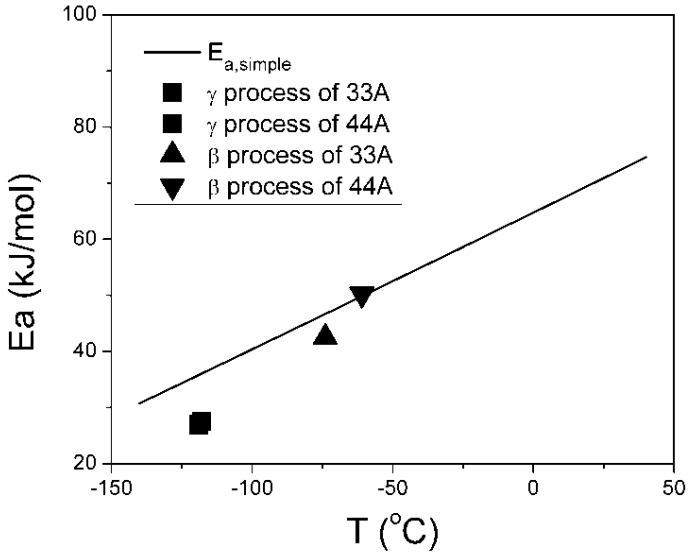

Figure 57. The Starkweather plot showing the activation energies for the γ and β processes that involve the HPE chain motions.

The Activation Energies. The activation energies of the HPE chain motions are also analyzed through the Starkweather method. The positions of the activation energies in the E_a-T map are shown in Figure 57, which found the activation energies below or

close to the zero entropy line. While for the γ processes the values are reasonable within experimental error considering they could be simple molecular motions that do not invoke much configurational entropy, the values of the activation energies for the β processes are too low. This might be due to several reasons: first of all, the model used for characterizing the HPE chain motions might not be accurate; secondly, the experimental line shapes are actually from three chemically distinct sites, which are believed to exhibit different mobilities[120,121] and make the dynamics extra heterogeneous so that no simple models can be used to precisely depict the picture.

Conclusions

The HPE chain molecular motions in 33A and 44A have been studied through ^{2}H NMR line shape analysis. The quadrupolar echo line shapes do not show any distinctive singularities, indicating ill-defined jump motions characterized by inhomogeneous distributions of motional amplitudes. On the other hand, high temperature $\eta = 1$ line shapes suggest that trans-gauche conformational transition is involved in the molecular motions. Therefore, a model that describes ill-defined two-site jumps of C-D bonds around C-C bonds at the tetrahedral angle (109.5 °C) is proposed. A bivariate normal distribution function was used to describe the heterogeneity of the molecular motion in the glassy state.

The Arrhenius plot shows that the HPE chain motions in these epoxies contribute to the very low temperature region of the mechanical relaxation spectra. The inflection in the Arrhenius plot and increase of activation energy of HPE motions, in agreement with the BPA ring motion study, suggests a possible origin of the β relaxation is the motion of the DGEBA repeat unit. The HPE segments start to exhibit different dynamics at above

100 °C, which is lower than the corresponding temperature for BPA rings, due to the proximity of HPE groups to the crosslink. Above 100 °C the HPE motions in 33A are slower because of its connection to the relatively static 33DDS moiety.

CHAPTER VI

SUMMARY

A comprehensive study of the glassy state molecular motions in isomeric epoxy networks 33A and 44A has been performed and presented in this dissertation. The isomeric epoxies are of interest because they exhibit substantial differences in thermal, mechanical, and morphological properties while they keep identical chemical composition. Especially, 33A resembles an anti-plasticized 44A. It is believed the understanding of the structure-dynamics-property relationships of thermoset polymers will enhance our capability of designing novel monomer molecules for building higher performance matrix materials for advanced carbon-fiber reinforced polymer composites.

The isomeric epoxy networks as shown in Figure 7 can be conveniently divided into three distinctive molecular groups, i.e., the bisphenol A structure (BPA), the hydroxypropyl ether segment (HPE), and the diaminodiphenylsulfone structure (DDS). The effects of structural isomerism on the glassy state molecular motions were studied using solid-state ^{2}H NMR spectroscopy, which offers unrivaled power to monitor site-specific molecular motions. Isomeric epoxy networks with deuterated phenylene rings in the BPA structure, deuterated phenylene rings in the DDS structure, and deuterated HPE group have been synthesized for the purpose of this dissertation. Quadrupolar echo experiments and line shape simulations have been employed as the main research approach to gain both qualitative and quantitative motional information of the epoxy networks in the glassy state. Quantitative information on the geometry and rate of the molecular motions allows the elucidation of the relationship between molecular motions and macro physical properties and the role of these motions in the mechanical relaxation.

In Chapter III, networks synthesized with deuterated BPA rings were used to investigate the differences in ring motions along with their role in the mechanical relaxation. The molecular motions were studied using ^{2}H quadrupolar echo line shape analysis where experimental spectra were compared to simulated line shapes calculated using a model that describes both ring π-flips and ring axis fluctuations.

The BPA ring motions which contribute to the low temperature regions of the mechanical γ relaxations in both 33A and 44A have almost identical behaviors up to a temperature 20 °C below the T_g of 33A, suggesting minimal influence of the crosslinkers on the BPA ring dynamics, which further indicates that the BPA ring motions are localized, and the correlation length of the motions is not longer than the DGEBA unit at these temperatures. The BPA ring motions of both epoxies exhibit an increase in activation energy at a temperature coinciding with the β relaxations of the two networks. This suggests the β relaxations are possibly related to the cooperative motion of the entire DGEBA unit, whereas below the β transition the ring motions have a correlation length equal to the BPA moiety. From the study of BPA ring motions, a picture of gradual development of molecular motions is seen, starting with localized motions that involve only the BPA unit, transitioning to a cooperative motion that has a correlation length scale of a DGEBA unit, and ultimately becoming long range cooperative motions characteristic of the glass transition.

In Chapter IV, networks with deuterated diamine rings were synthesized to investigate the role of these motions in the mechanical relaxation of the two networks and explain at a molecular level the anti-plasticization effect through ^{2}H NMR line shape analysis. The 44DDS ring motion is found to contribute to the high temperature part of

44A's γ relaxation. The activation energy of 44DDS ring flip motion is high, possibly due to the rigid nature of 44DDS as well as it being the crosslink. The 44DDS diamine rings undergo flip motions and the diamine backbones actively fluctuate and sweep out certain molecular space. The occurrence of 44DDS ring motions decreases the modulus of 44A and the swept-out space from the fluctuation of the 44DDS ring axis explains the higher hole-size free volume. The 40 °C difference in the T_g's of the networks is attributed to the additional energy dissipation mechanism by the 44DDS ring motions. 33DDS rings do not exhibit large amplitude motions but only undergo fast small-angle fluctuations, which results in a decrease in the magnitude of the high temperature part of the γ relaxation of 33A, a phenomenon often seen in the anti-plasticization process. Therefore the anti-plasticization effect is attributed to the meta-substitution on the diamine phenylene rings which suppresses large amplitude motions and leads to more compact packing in 33A.

In Chapter V, the HPE chain molecular motions in 33A and 44A have been studied through ^{2}H NMR line shape analysis. The quadrupolar echo line shapes do not show any distinctive singularities, indicating ill-defined jump motions characterized by inhomogeneous distributions of motional amplitudes. On the other hand, high temperature $\eta = 1$ line shapes suggest that trans-gauche conformational transition is involved in the molecular motions. Therefore, a model that describes ill-defined two-site jumps of C-D bonds around C-C bonds at the tetrahedral angle (109.5 °C) is proposed. A bivariate normal distribution function was used to describe the heterogeneity of the molecular motion in the glassy state.

The temperature dependence of two-site jump rates shows that the HPE chain motions in these epoxies contribute to the very low temperature region of the mechanical relaxation spectra. The inflection in the Arrhenius plot and increase of activation energy of HPE motions, in agreement with the BPA ring motion study, suggests a possible origin of the β relaxation is the motion of the DGEBA repeat unit. The HPE segments starts to exhibit different dynamics above 100 °C, earlier than the corresponding temperature for BPA rings, due to the proximity of HPE groups to the crosslink. Above 100 °C the HPE motions in 33A are slower because of its connection to the relatively static 33DDS moiety.

In summary, the structure-dynamics-property relationships in thermoset epoxies were studied comprehensively utilizing the power of solid-state ^{2}H NMR spectroscopy. The completed research in this dissertation has been able to connect the microscopic molecular events to macro scale thermomechanical properties of polymer materials as shown in Figure 58. Finally I hope the knowledge will enhance our capability of designing novel monomer molecules for building higher performance matrix materials for advanced carbon-fiber reinforced polymer composites.

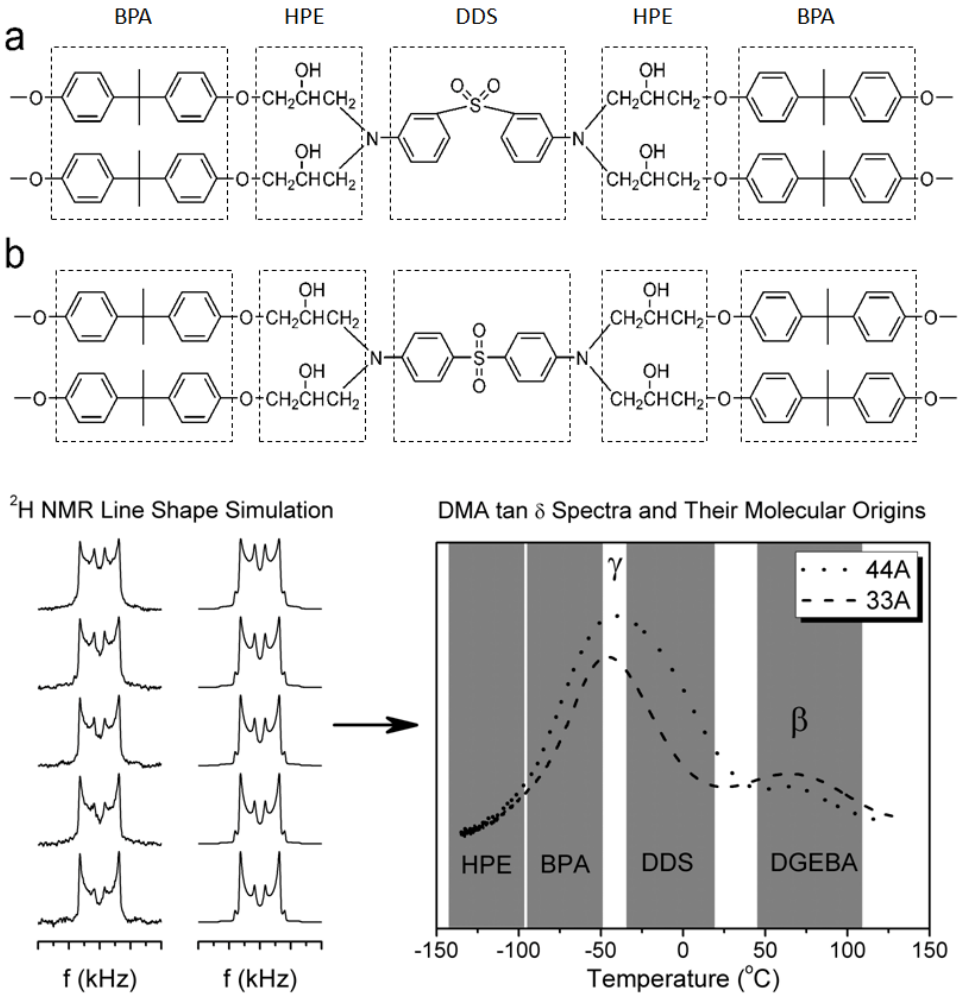

Figure 58. Summary of the dissertation research.

APPENDIX A

MATLAB SCRIPT FOR SIMULATION PARAMETER STEPPING TO OBTAIN 3D LINE SHAPE BASIS SETS FOR PHENYLENE RING MOTIONS

This MatLab® script utilizes EXPRESS program[119] to calculate a series of line shapes with varying parameters.

```
clear

%  load a parameter set saved from EXPRESS calculation of
%  phenylene ring motion based on the model illustrated in Figure X.
load fax400.mat
load 022714_FlipandFluc.fig_param.mat

%  simulation echo delay values
tau1 = [25 50 75 100 150] ;

%  define 18 k1 values, 11 k2 values, and 7 theta values for the model
fliprates = [1.2 1.6 2.2:0.4:6.6 7.2 8 8.8 9.6] ;
n1 = length(fliprates) ;

flucrates = 1.2:0.6:7.2 ;
n2 = length(flucrates) ;

coneangles =6:6:42 ;
n3 = length(coneangles) ;

%  pre-assign volume for FIDs to be calculated
sigs = cell(1,5) ;
for tt = 1:5
    sigs{1,tt} = cell(n1,n2,n3) ;

    for ii = 1:n1
        for jj = 1:n2
            for kk = 1:n3
                sigs{1,tt}{ii,jj,kk} = zeros(2048,1) ;
            end
        end
    end
end
```

```
35 -    param.n = 3000 ;
36 -    for tt = 1:5
37          %  change the echo delay value
38 -        param.pulse = tau1(tt) ;
39
40 -        for ii = 1:n1
41              %  vary the k1 value
42 -            param.frames{1,1}.rate = 10^fliprates(ii) ;
43 -            newparam = rebuild(param,'rates') ;
44 -            param = newparam ;
45
46 -            for jj = 1:n2
47                  %  vary the k2 value
48 -                param.frames{1,2}.rate = 10^flucrates(jj) ;
49 -                newparam = rebuild(param,'rates') ;
50 -                param = newparam ;
51
52 -                for kk = 1:n3
53                      %  vary the theta value
54 -                    param.frames{1,2}.cq_theta = [0 coneangles(kk)*ones(1,3)] ;
55 -                    newparam = rebuild(param,'CQangles') ;
56 -                    param = newparam ;
57
58                      %  this is the major step which calculates a FID
59                      %  using the EXPRESS script for QE line shapes.
60 -                    sig1 = staticsim(param) ;
61
62                      %  left shift the FID to echo maximum
63 -                    sig1 = [sig1(tau1(tt)+1:2048,1);zeros(tau1(tt),1)] ;
64
65                      %  assign the calculated FID to one of
66                      %  the 3D line shape basis sets
67 -                    sigs{1,tt}{ii,jj,kk} = sig1 ;
68 -                end
69 -            end
70 -        end
71 -    end
72
73 -    clear ii jj kk newparam sig1 n1 n2 n3 tt
```

APPENDIX B

MATLAB SCRIPT FOR CALCULATION OF 3D PROBABILITY DENSITY

This script defines a function for calculating the 3D (18 by 11 by 6) probability density for the superposition of a 3D line shape basis set.

```
function [pds, PDS] = mmvncdf(rt1,sigma1,rt2,sigma2,coneangle,sigma3,rho)

%  these values defines probability density
%  cubic spaces for individual line shapes
xa = [-Inf 1.2 2 2.4:0.4:6.8 7.6 8.4 9.2 Inf] ;
ya = [-Inf 1.5:0.6:6.9 Inf] ;
za = [0 9:6:45] ;

%  correlation parameters describing the correlation between
%  the three parameters of the phenylene ring motion model.
cr = [1 rho rho; rho 1 rho; rho rho 1] ;

%  normalize
x = (xa-rt1)/sigma1 ;
y = (ya-rt2)/sigma2 ;
z = (za-coneangle)/sigma3 ;

%  calculate the cumulative probability densities
[Y,X,Z] = meshgrid(y,x,z) ;

XYZ = [ Y(:) X(:) Z(:)] ;

cdfs = mvncdf(XYZ,[0 0 0],cr) ;

CDFS = reshape(cdfs, 19,12,8) ;

%  get the cubic probability densities
PDS = CDFS(2:19,2:12,2:8)...
    - CDFS(1:18,1:11,1:7)...
    - CDFS(1:18,2:12,2:8)...
    - CDFS(2:19,1:11,2:8)...
    - CDFS(2:19,2:12,1:7)...
    + CDFS(1:18,1:11,2:8)...
    + CDFS(1:18,2:12,1:7)...
    + CDFS(2:19,1:11,1:7) ;

m2c = mat2cell(PDS,18,ones(1,11),ones(1,7)) ;
pds = cat(1,m2c{:}) ;
```

APPENDIX C

PERMISSION TO USE FIGURES 2, 3, and 4

AMERICAN PHYSICAL SOCIETY
One Physics Ellipse, College Park, MD 20740 · http://www.aps.org

September 24, 2014

Jianwei Tu
Wiggins Research Group
School of Polymers and High Performance Materials
The University of Southern Mississippi

Ref # 28192

Thank you for your permission request dated Sept. 15, 2014. We are pleased to grant you a non-exclusive, non-transferable permission, English rights, limited to **print and electronic format**, provided you meet the criteria outlined below. Permission is for a one-time use and does not include permission for future editions, updates, databases, translations, or any other matters. Permission must be sought for each additional use. This permission does not include the right to modify APS material.

Please print the required copyright credit line on the first page that the material appears: "Reprinted (abstract/excerpt/figure) with permission from [FULL REFERENCE CITATION] as follows: authors names, journal title, volume number, page number and year of publication. Copyright (YEAR) by the American Physical Society.

The following language must appear somewhere on the website: "Readers may view, browse, and/or download material for temporary copying purposes only, provided these uses are for noncommercial personal purposes. Except as provided by law, this material may not be further reproduced, distributed, transmitted, modified, adapted, performed, displayed, published, or sold in whole or part, without prior written permission from the American Physical Society."

Provide a hyperlink from the reprinted APS material (the hyperlink may be embedded in the copyright credit line). APS's link manager technology makes it convenient and easy to provide links to individual articles in APS journals. For information, see: http://link.aps.org/.

You must also obtain permission from at least one of the authors for each separate work, if you haven't done so already. The author's name and address can be found on the first page of the published Article.

Use of the APS material must not imply any endorsement by the American Physical Society.

Permission is granted for use of the following APS material only:

- Figs. 4, 7, 8, Rev. Mod. Phys. 83, 587 – Published 20 June 2011

Permission is limited to the single title specified of the publication as follows:
A thesis entitled "Investigation of Glassy State Molecular Motions in Thermoset Polymers" to be published by ProQuest LLC.

If you have any questions, please refer to the Copyright FAQ at: http://publish.aps.org/copyrightFAQ.html or send an email to assocpub@aps.org.

Sincerely,

Jamie L. Casey
Circulation and Fulfillment Assistant

APPENDIX D

PERMISSION TO USE FIGURE 45

JOHN WILEY AND SONS LICENSE TERMS AND CONDITIONS

Sep 22, 2014

This is a License Agreement between Jianwei Tu ("You") and John Wiley and Sons ("John Wiley and Sons") provided by Copyright Clearance Center ("CCC"). The license consists of your order details, the terms and conditions provided by John Wiley and Sons, and the payment terms and conditions.

All payments must be made in full to CCC. For payment instructions, please see information listed at the bottom of this form.

License Number	3474300116995
License date	Sep 22, 2014
Licensed content publisher	John Wiley and Sons
Licensed content publication	Polymer Engineering & Science
Licensed content title	Reinforcement of epoxy networks with sulfur- and carbon-based molecular fortifiers
Licensed copyright line	Copyright © 2007 Society of Plastics Engineers
Licensed content author	Alan J. Lesser,Kevin Calzia,Matthais Junk
Licensed content date	Sep 12, 2007
Start page	1569
End page	1575
Type of use	Dissertation/Thesis
Requestor type	University/Academic
Format	Print and electronic
Portion	Figure/table
Number of figures/tables	1
Original Wiley figure/table number(s)	Figure 5
Will you be translating?	No
Title of your thesis / dissertation	INVESTIGATION OF GLASSY STATE MOLECULAR MOTIONS IN THERMOSET POLYMERS
Expected completion date	Dec 2014
Expected size (number of pages)	150
Total	0.00 USD

REFERENCES

[1] Ober, C. K.; Cheng, S. Z. D.; Hammond, P. T.; Muthukumar, M.; Reichmanis, E.; Wooley, K. L.; Lodge, T. P. *Macromolecules* **2009**, *42(2)*, 465-471.

[2] Sprenger, S. *J. Mater. Sci.* **2014**, *49*, 2391-2402.

[3] Bagheri, R.; Marouf, B. T.; Pearson, R. A. *J. Macromol. Sci., Part C: Polym. Rev.* **2009**, *49*, 201-225.

[4] Spiess, H. W. *Macromolecules* **2010**, *43(13)*, 5479-5491.

[5] Anderson, P. W. *Science* **1995**, *267(5204)*, 1615.

[6] Kennedy, D.; Norman, C. *Science* **2005**, *309*, 75.

[7] Angell, C. A. *Annu. Rev. Phys. Chem.* **2004**, *55*, 559-583.

[8] Tarjus, G. An Overview of the Theories of the Glass Transition. In *Dynamical Heterogeneity in Glasses, Colloids, and Granular Media*, Berthier, L., Eds.; Oxford University Press: Oxford, UK, 2011; pp 39-67.

[9] Angell, C. A. *Science* **1995**, *267*, 1924.

[10] Böhmer, R.; Ngai, K. L.; Angell, C. A.; Plazek, D. J. *J. Chem. Phys.* **1993**, *99*, 4201.

[11] Hong, L.; Novikov, V. N.; Sokolov, A. P. *J. Non-Cryst. Solids* **2011**, *257*, 351-356.

[12] Debenedetti, P. G.; Stillinger, F. H. *Nature (London)* **2001**, *410*, 259.

[13] Scopigno, T.; Ruocco, G.; Sette, F.; Monaco, G. *Science*, **2003**, *302*, 849.

[14] Sangoro, J. R.; Iacob, C.; Agapov, A. L.; Wang, Y.; Berdzinski, S.; Rexhausen, H.; Strehmel, V.; Friedrich, C.; Sokolov, A. P.; Kremer, F. *Soft Matter* **2014**, *10*, 3536.

[15] Wang, Y.; Agapov, A. L.; Fan, F.; Hong, K.; Yu, X.; Mays, J.; Sokolov, A. P. *Phys. Rev. Lett.* **2012**, *108*, 088303.

[16] Agapov, A. L.; Sokolov, A. P. *Macromolecules* **2011**, *44*, 4410-4414.

[17] Mapes, M. K.; Swallen, S. F.; Ediger, M. D. *J. Phys. Chem. B* **2006**, *110*, 507.

[18] Adam, G.; Gibbs, J. H. *J. Chem. Phys.* **1965**, *43(1)*, 139-146.

[19] Kauzmann, A. W. *Chem. Rev.* **1948**, *43*, 219.

[20] Tanaka, H. *Phys. Rev. Lett.* **2003**, *90*, 055701.

[21] Leheny, R. L.; Menon, N.; Nagel, S. R.; Price, D. L.; Suzuya, K.; Thiyagarajan, P. *J. Chem. Phys.* **1996**, *105*, 7783.

[22] Franz, S.; Parisi, G. *J. Phys.: Condens. Matter* **2000**, *12*, 6335.

[23] Berthier, L.; Biroli, G.; Bouchaud, J. -P.; Kob, W.; Miyazaki, K.; Reichman, D. R. *J. Chem. Phys.* **2007**, *125*, 184503.

[24] Berthier, L.; Biroli, G.; Bouchaud, J. -P.; Kob, W.; Miyazaki, K.; Reichman, D. R. *J. Chem. Phys.* **2007**, *125*, 184504.

[25] Toninelli, C.; Wyart, M.; Berthier, L.; Biroli, G.; Bouchaud, J.-P. *Phys. Rev. E* **2005**, *71*, 041505.

[26] Berthier, L.; Biroli, G. *Rev. Modern Phys.* **2011**, *83(2)*, 587-645.

[27] Riggleman, R. A.; Lee, H.-N.; Ediger, M. D.; de Pablo, J. J. *Soft Matter* **2010**, *6*, 287-291.

[28] Pardo, L. C.; Lunkenheimer, P.; Loidl, A. *Phys. Rev. E* **2007**, *76*, 030502(R).

[29] Andersen, H. C. *Proc. Natl. Acad. Sci. U.S.A.* **2005**, *102*, 6686.

[30] Heuer, A.; Wilhelm, M.; Zimmermann, H.; Spiess, H. W. *Phys. Rev. Lett.* **1995**, *75*, 2851.

[31] Tracht, U.; Wilhelm, M.; Heuer, A.; Feng, H.; Schmidt-Rohr, K.; Spiess, H. W. *Phys. Rev. Lett.* **1998**, *81*, 2727.

[32] Reinsberg, S. A.; Qiu, X. H.; Wilhelm, M.; Spiess, H. W.; Ediger, M. D. *J. Chem. Phys.* **2001**, *114*, 7299.

[33] Vidal Russell, E.; Israeloff, N. E. *Nature (London)* **2000**, *408*, 695.

[34] Tracht, U.; Wilhelm, M.; Heuer, A.; Spiess, H. W. *J. Magn. Reson.* **1999**, *140*, 460.

[35] Fujara, F.; Geil, B.; Sillescu, H.; Fleischer, G. *Z. Phys. B* **1992**, *88*,195.

[36] Ediger, M. D. *Annu. Rev. Phys. Chem.* **2000**, *51*, 99.

[37] Dyre, J. C.; Hechsher, T.; Niss, K. *J. Non-Cryst. Solids* **2009**, *355*, 624-627.

[38] Capaccioli, S.; Thayyil, M. S.; Ngai, K. L. *J. Phys. Chem. B.* **2008**, *112*, 16035-16049.

[39] Starkweather, H. W. *Macromolecules* **1988**, *21*, 1798-1802.

[40] Johari, G. P.; Goldstein, M. *J. Chem. Phys.* **1970**, *53*, 2372.

[41] Thayyil, M. S.; Capaccioli, S.; Prevosto, D.; Ngai, K. L. *Philosophical Mag.* **2008**, *88*, 4007-4013.

[42] Kessairi, K.; Capaccioli, S.; Prevosto, D.; Lucchesi, M.; Sharifi, S.; Rolla, P. A. *J. Phys. Chem. B* **2008**, *112*(*15*), 4470-4473.

[43] Schmidt-Rohr, K.; Kudlik, A. S.; Beckham, H. W.; Ohlemacher, A.; Pawelzik, U.; Boeffel, C.; Spiess, H. W. *Macromolecules* **1994**, *27*, 4733.

[44] Kudlik, A. S.; Beckham, H. W.; Schmidt-Rohr, K.; Radloff, D.; Pawelzik, U.; Boeffel, C.; Spiess, H. W. *Macromolecules* **1994**, *27*, 4746.

[45] Gaborieau, M.; Graf, R.; Kahle, S.; Pakula, T.; Spiess, H. W. *Macromolecules* **2007**, *40*, 6249-6256.

[46] Ngai, K. L.; Paluch, M. *J. Chem. Phys.* **2004**, *120*(*2*), 857-873.

[47] Ngai, K. L.; Casalini, R.; Capaccioli, S.; Paluch, M.; Roland, C. M. *J. Phys. Chem. B* **2005**, *109*, 17356.

[48] Mierzwa, M.; Pawlus, S.; Paluch, M.; Kaminska, E.; Ngai, K. L. *J. Chem. Phys.* **2008**, *128*, 044512.

[49] Ngai, K. L. *Solid State Phys.* **1979**, *9*, 121.

[50] (a) Tsang, K. Y.; Ngai, K. L. *Phys. Rev. E* **1996**, *54*, R3067; (b) **1997**, *56*, R17.

[51] Ngai, K. L. *J. Phys.: Condens. Matter* **2003**, *15*, S1107.

[52] Kudlik, A.; Benkhof, S.; Blochowicz, T.; Tschirwitz, C.; Rossler, E. *J. Mol. Struct.* **1999**, *479*, 201.

[53] Ngai, K. L. *J. Chem. Phys.* **1998**, *109*, 6982.

[54] Ngai, K. L.; Prevosto, D.; Capaccioli, S.; Roland, C. M. *J. Phys.: Condens. Matter* **2008**, *20*, 244125.

[55] Heuer, A. *J. Phys.: Condens. Matter* **2008**, *20*, 373101.

[56] Stillinger, F. H.; Weber, T. A. *Science* **1984**, *225*, 983.

[57] Middleton, T. F.; Wales, D. *J. Phys. Rev. B* **2001**, *64*, 024205.

[58] de Souza, V. K.; Wales, D. *J. Phys. Rev. B* **2006**, *74*, 134202.

[59] Doliwa, B.; Heuer, A. *Phys. Rev. Lett.* **2003**, *91*, 235501.

[60] Stilinger, F. H. *Science* **1995**, *267*, 1935-1939.

[61] Vogel, M.; Doliwa, B.; Heuer, A.; Glotzer, S. C. *J. Chem. Phys.* **2004**, *120*, 4404-4414.

[62] Goldstein, M. *J. Chem. Phys.* **2010**, *132*, 041104.

[63] Middleton, T. F.; Wales, D J. *J. Chem. Phys.* **2004**, *120*, 8134.

[64] de Souza, V. K.; Wales, D. J. *J. Chem. Phys.* **2009**, *130*, 194508.

[65] Berne, B. J.; Pecora, R. *Dynamic Light Scattering*; Dover: Mineola, 2000.

[66] Schaefer, J.; Stejskal, E. O.; Buchdahl, R. *Macromolecules* **1975**, *8*, 291.

[67] Schaefer, J.; Stejskal, E. O.; Buchdahl, R. *Macromolecules* **1977**, *10*, 384.

[68] Yannoni, C. S. *Acc. Chem. Res.* **1982**, *15*, 201-208.

[69] Monnerie, L.; Lauprêtre, F.; Halary, J. L. *Adv. Polym. Sci.* **2005**, *187*, 35-213.

[70] de Azevedo, E. R.; Bonagamba, T. J.; Reichert, D. *Progr. Nucl. Magn. Reson. Spec.* **2005**, *47*, 137-164.

[71] Stueber, D.; Yu, T.-Y.; Hess, B.; Kremer, K.; O'Conner, R. D.; Schaefer, J. *J. Chem. Phys.* **2010**, *132*, 104901.

[72] Heinz, S. R.; Wiggins, J. S. *Polymer Testing* **2010**, *29*, 925-932.

[73] Jackson, M. B.; Kaushik, M.; Nazarenko, S.; Ward, S.; Maskell, R.; Wiggins, J. S. *Polymer* **2011**, *52*, 4528-4535.

[74] Spiess, H. W. *Chem. Rev.* **1991**, *91*, 1321.

[75] Brown, S. P.; Spiess, H. W. *Chem. Rev.* **2001**, *101*, 4125.

[76] Schmidt-Rohr, K.; Spiess, H. W. *Multidimensional Solid-State NMR and Polymers*; Academic Press: London, 1994.

[77] Duer, M. J. *Solid State NMR Spectroscopy: Principles and Applications*; Blackwell: Oxford, 2003.

[78] Levitt, M. H. *Spin Dynamics: Basics of Nuclear Magnetic Resonance*, 2nd ed.; John Wiley & Sons Ltd.: West Sussex, England, 2008.

[79] Ward, I. M. *Structure and Properties of Oriented Polymers*; Chapman & Hall: London, 1997.

[80] *Handbook of Liquid Crystals*; Demus, D., Goodby, J., Gray, G. W., Spiess, H. W., Vill, V., Eds.; Wiley-VCH: Weinheim, 1998.

[81] Spiess, H. W. *Colloid & Polymer Science* **1983**, *261*, 193-209.

[82] Jelinski, L. W. *Ann. Rev. Mater. Sci.* **1985**, *15*, 359-377.

[83] Brown, M. F.; Lope-Piedrafita, S.; Martinez, G. V.; Petrache, H. I. In *Modern Magnetic Resonance*; Graham, A. W.; Springer: London, 2006; pp 249-260.

[84] Böhmer, B.; Diezemann, G.; Hinze, G.; Rössler, E. *Prog. NMR spect.* **2001**, *39*, 191-267.

[85] Macho, V.; Brombacher, L.; Spiess, H. W. *Appl. Magn. Reson.* **2001**, *20*. 405.

[86] Kinnun, J. J.; Leftin, A.; Brown, M. F. *J. Chem. Edu.* **2013**, *90*. 123-128.

[87] Spiess, H. W.; Sillescu, H. *J. Magn. Reson.* **1981**, *42*, 381.

[88] Macho, V.; Brombacher, L.; Spiess, H. W. *Appl. Magn. Reson.* **2001**, *20*, 405-432.

[89] Heinz, S. R. Development and Utilization of Digital Image Correlation Techniques for the Study of Structural Isomerism Effects on Strain Development in Epoxy Network Glasses. Ph.D. Dissertation, the University of Southern Mississippi, Hattiesburg, MS, December 2011.

[90] Boyer, R. F. *Polym. Eng. Sci.* **1968**, *8(3)*, 161-185.

[91] Klug, C. A.; Wu, J.; Xiao, C.; Yee, A. F.; Schaefer, J. *Macromolecules* **1997**, *30*, 6302-6306.

[92] Wu, J.; Xiao, C.; Yee, A. F.; Klug, C. A.; Schaefer, J. J. *Polym. Sci.: Part B: Polym. Phys.* **2001**, *39*, 1730-1740.

[93] Kaji, H.; Tai, K.; Horii, F. *Macromolecules* **2001**, *34*, 6318-6324.

[94] Kaji, H.; Fuke, K.; Horii, F. *Macromolecules* **2003**, *36*, 4414-4423.

[95] Arrese-Igor, S.; Arbe, A.; Alegría, A.; Colmenero, J.; Frick, B. *Physical Review E* **2007**, *75*, 051801.

[96] Dumais, J. J.; Cholli, A. L.; Jelinski, L. W.; Hedrick, J. L.; McGrath, J. E. *Macromolecules* **1986**, *19*, 1884-1889.

[97] David, L.; Girard, C.; Dolmazon, R.; Albrand, M.; Etienne, S. *Macromolecules* **1996**, *29*, 8343-8348.

[98] Arrese-Igor, S.; Arbe, A.; Colmenero, J.; Alegría, A.; Frick, B. *Physica B* **2004**, *350*, 211-213.

[99] Quintana, I.; Arbe, A.; Colmenero, J.; Frick, B. *Macromolecules* **2005**, *38*, 3999-4013.

[100] Schadt, R. J.; Cain, E. J.; Gardner, K. H.; Gabara, V.; Allen, S. R.; English, A. D. *Macromolecules* **1993**, *26*, 6503-6508.

[101] Schadt, R. J.; Gardner, K. H.; Gabara, V.; Allen, S. R.; Chase, D. B.; English, A. D. *Macromolecules* **1993**, *26*, 6509-6516.

[102] Schaefer, D. J.; Schadt, R. J.; Gardner, K. H.; Gabara, V.; Allen, S. R.; English, A. D. *Macromolecules* **1995**, *28*, 1152-1158.

[103] Wilhelm, M.; Spiess, H. W. *Macromolecules* **1996**, *29*, 1088-1090.

[104] Kawaguchi, T.; Mamada, A.; Hosokawa, Y.; Horii, F. *Polymer* **1998**, *39(13)*, 2725-2732.

[105] Simpson, J. H.; Rice, D. M.; Karasz, F. K. *Macromolecules* **1992**, *25*, 2099-2106.

[106] Simpson, J. H.; Liang, W.; Rice, D. M.; Karasz, F. K. *Macromolecules* **1992**, *25*, 3068-3074.

[107] Bang, H. S.; Oh, I. H.; Lee, K. W.; Han, J. H.; Lee, C. E.; Jin, J. -I. *Journal of Applied Physics* **2007**, *102*, 116106.

[108] Roy, A. K.; Jones, A. A.; Inglefield, P. T. *Macromolecules* **1986**, *19*, 1356-1362.

[109] Goetz, J. M.; Wu, J.; Yee, A. F.; Schaefer, J. *Macromolecules* **1998**, *31*, 3016-3020.

[110] Wehrle, M.; Hellmann, G. P.; Spiess, H. W. *Colloid & Polymer Science* **1987**, *265*, 815-822.

[111] Shi, J. –F.; Inglefield, P. T.; Jones, A. A.; Meadows, M. D. *Macromolecules* **1996**, *29*, 605-609.

[112] Hansen, M. T.; Blümich, B.; Boeffel, C.; Spiess, H. W. *Macromolecules* **1992**, *25*, 5542-5544.

[113] Hansen, M. T.; Boeffel, C.; Spiess, H. W. *Colloid & Polymer Science* **1993**, *271*, 446-453.

[114] Henrichs, P. M.; Nicely, V. A.; Fagerburg, D. R. *Macromolecules* **1991**, *24*, 4033-4037.

[115] Poliks, M. D.; Gullion, T.; Schaefer, J. *Macromolecules* **1990**, *23*, 2678-2681.

[116] Lee, P. L.; Schaefer, J. *Macromolecules* **1995**, *28*, 2577-2578.

[117] Tucker, S. J. Study of 3,3' vs. 4,4' DDS Isomer Curatives on Physical Properties and Phenyl Ring Motions of DGEBA Epoxy via Molecular Dynamics, Deuterium NMR, and Dielectric Spectroscopy. Ph.D. Dissertation, the University of Southern Mississippi, Hattiesburg, MS, December 2010.

[118] Vold, R. L.; Hoatson, G. L. *J. Magn. Reson.* **2009**, *198*, 57-72.

[119] EXPRESS DOWNLOAD | NMR. http://web.wm.edu/nmr/express_download_form.php (accessed June 2012).

[120] Hirschinger, J.; Miura, H.; Gardner, K. H.; English, A. D. *Macromolecules* **1990**, *23*, 2153-2169.

[121] Miura, H.; Hirschinger, J.; English, A. D. *Macromolecules* **1990**, *23*, 2169-2182.

[122] Schadt, R. J.; Cain, E. J.; English, A. D. *J. Phys. Chem.* **1993**, *97*, 8387-8392.

[123] Garin, N.; Hirschinger, J.; Beaume, F.; Lauprêtre, F. *Polymer* **2000**, *41*, 4281-4284.

[124] Molina-Mateo, J.; Torregrosa-Cabanilles, C.; Sabater-Serra, R.; Meseguer-Duenas, J. M.; Gomez-Ribelles, J. L. *J. Non-Crystalline Solids* **2013**, *362*, 175-179.

[125] Schmidt, C.; Kuhn, K. J.; Spiess, H. W. *Progr. Colloid & Polymer Sci.* **1985**, *71*, 71-76.

[126] Graf, R.; Ewen, B.; Spiess, H. W. *J. Chem. Phys.* **2007**, *126*, 041104.

[127] Whitney, D. R.; Yaris, R. *Macromolecules* **1997**, *30*, 1741-1751.

[128] Bloom, M.; Davis, J. H.; Valic, M. I. *Can. J. Phys.* **1980**, *58*, 1510-1517.

[129] Genz, A. *Statistics and Computing* **2004**, *14(3)*, 251-260.

[130] Koike, Y.; Shibayama, M.; Asai, M. *Macromolecules* **2011**, *44*, 6615-6624.

[131] Vogel, M.; Medick, P.; Rössler, E. A. *Annual Reports on NMR Spectroscopy* **2005**, *56*, 231-299.

[132] Hansen, M. R.; Graf, R.; Spiess, H. W. *Accounts of Chemical Research* **2013**, *46(9)*, 1996-2007.

[133] Lesser, A. J.; Calzia, K.; Junk, M. *Polym. Eng. Sci.* **2007**, *47*, 1569-1575.

[134] Zerda, A. S.; Lesser, A. J. *J. Appl. Polym. Sci.* **2002**, *84*, 302-309.

[135] Ueda, M. *Polym. Eng. Sci.* **2004**, *44*, 1877-1884.

[136] Kins, C. F.; Dudenko, D.; Sebastiani, D.; Branklaus, G. *Macromolecules* **2010**, *43*, 7200-7211.

[137] Jelinski, L. W.; Dumais, J. J.; Engel, A. K. *Macromolecules* **1983**, *16*, 492-496.

[138] Mehring, M. In *NMR: Basic Princ. Prog.* **1976**, *11*.